NUMERICAL SIMULATION OF GERMANIUM SINGLE CRYSTALS GROWN WITH A LOW MELT HEIGHT AND AN AXIAL VIBRATION

by

Pouya Yousefi Louyeh

B.S., Mechanical Engineering, Karaj Azad University, 2011

Submitted to the Institute for Graduate Studies in
Science and Engineering in partial fulfilment of
the requirements for the degree of
Master of Science

Graduate Program in Mechanical Engineering

Boğaziçi University

2016

ACKNOWLEDGEMENTS

I would like to thank my parents Yaghoub Yousefi and Zeynab Yaghoubi, and my brother Pedram Yousefi for their support, encouragement, and valuable advices in my whole life, especially my education at Boğaziçi University.

I also want to express my appreciation to my thesis supervisor, Dr. Ercan Balıkçı, for his passion, guidance, patience, and flawless support during my research in graduate level. In addition, I would be glad to thank Dr. Jeremy K. Mason for his helpful advice and suggestions in numerical part of my research. Besides, I thank the other member of my thesis committee, Dr. Necip Ünlü, for his valuable suggestions.

I sincerely appreciate all my colleagues and friends for their help and support, particularly, my friend and team mate Aidin Sheikhi for his contributions as my partner in this project. I also acknowledge my friend Mehdi Montakhab for his helpful suggestions in my research.

The work in this thesis is funded by The Scientific and Technological Research Council of Turkey (TUBITAK), under the grant number 212M030. I am appreciative for their support.

ABSTRACT

NUMERICAL SIMULATION OF GERMANIUM SINGLE CRYSTALS GROWN WITH A LOW MELT HEIGHT AND AN AXIAL VIBRATION

In this study, antimony-doped germanium (Ge-Sb) crystal growth from the melt using three directional growth methods, the vertical Bridgman (VB), the axial heat processing (AHP), and the axial vibrational control (AVC), is investigated. In the VB method, the radial heat flux from furnaces leads to a natural convective flow near the s/l interface. The convective flow results in an inhomogeneous solute distribution. In the AHP method, immersing a high thermal conductivity baffle in the melt reduces the melt height and changes the convective flow pattern near the s/l interface. Consequently, the solute segregation is reduced and the single crystal length is increased. In the AVC method, axial vibration of the immersed baffle generates a forced convective flow in growth region which affects the crystals quality. Varying amplitude and frequency of vibration results in various convective flow patterns near the s/l interface. Appropriate adjusted amplitude and frequency of vibration can improve the crystal quality.

Six Sb-doped Ge crystals are grown experimentally with the aforementioned methods to investigate the effect of the melt height, pulling velocity, and amplitude and frequency of the vibrating baffle on the solute distribution, achieved single crystal length, and morphological stability of the grown crystals. Numerical simulations for all of the three mentioned methods with different growth parameters are performed and compared with experimental results. The interface shape obtained from the experimental results is verified by simulations. Extra simulations with parameters different than experiments are performed to better understand the melt flow characteristics and its influence on crystal growth from the melt. The flow pattern and temperature distribution are investigated by simulations with varying pulling velocities, melt heights, and vibrational parameters. The influence of natural convection flow in the VB and AHP methods and of forced flow in the AVC method on the solidification rate, interface shape, and grown crystal quality is analyzed. A reduced melt height and properly adjusted axial vibration amplitude and frequency improve crystal quality and production yield.

ÖZET

DÜŞÜK SIVI YÜKSEKLİĞİYLE VE EKSENEL TİTREŞİMLE BÜYÜTÜLMÜŞ GERMANYUM TEK KRİSTALLERİN NÜMERİK SİMÜLASYONU

Bu çalışmada Vertical Bridgman (VB), Axial Heat Processing (AHP), ve Axial Vibrational Control (AVC) olmak üzere üç tek yönlü büyütme yöntemiyle eriyikten antimon katkılı germanyum (Ge-Sb) kristallerinin büyütülmesi incelenmiştir. VB yönteminde, radyal ısı girdisi doğal konvektif akışa sebep olmaktadır. Konvektif akış homojen olmayan katışkı dağılımına neden olmaktadır ve bu yüksek kalite kristallerde istenmemektedir. AHP yönteminde yüksek iletkenliğe sahip bir aparatın (baffle) eriyike daldırılmasıyla eriyik yüksekliği azaltılır ve katı/sıvı ara yüzünün yakınındaki konvektif akışı değiştirir. Sonuç olarak, katışkı segregasyonu azaltılmış ve tek kristal boyu arttırılmış olur. AVC yönteminde, eriyike daldırılmış aparatın eksenel titreşimi büyüme bölgesinde konvektif akış yaratır ve bu da kristal kalitesini etkiler. Titreşim frekansındaki ve genliğindeki değişimler katı/sıvı ara yüzünün yakınında çeşitli konvektif akış türleri oluşturur. Titreşim frekansı ve genliğinin doğru şekilde ayarlanması kristal kalitesini arttırabilir.

Eriyik yüksekliği, çekme hızı, ve titreşen aparatın genliği ve frekansının katışkı dağılımına, elde edilen tek kristal boyuna, ve morfolojik kararlılığına etkisini görmek için altı antimon katkılı germanyum kristal yukarıda bahsedilen yöntemlerle büyütülmüştür. Her üç yöntem için de farklı büyütme parametreleriyle nümerik simülasyonlar yapılmış ve sonuçları deneylerin sonuçlarıyla karşılaştırılmıştır. Deneysel sonuçlarda görülen arayüzey şekli simülasyonlarla desteklenmiştir. Eriyik akışının karakteri ve kristal büyümesine etkilerini daha iyi anlamak için deney parametrelerinden farklı parametrelerle ilave simülasyonlar yapılmıştır. Akış modeli ve sıcaklık dağılımı, çeşitli çekme hızları, eriyik yükseklikleri ve titreşimsel parametrelerle tespit edilmiştir. Doğal konvektif akışın VB ve AHP yöntemlerinde, yaratılmış konvektif akışın ise AVC yönteminde katılaşma oranı, ara yüz şekli, ve büyütülmüş kristal kalitesi üzerindeki etkisi analiz edilmiştir. Azaltılmış eriyik yüksekliği ve uygun şekilde ayarlanmış eksenel titreşim genliği ve frekansı kristal kalitesini ve üretimini arttırdığı gözlenmiştir.

TABLE OF CONTENTS

ACKNOWLEDGEMENTS iii

ABSTRACT iv

ÖZET v

LIST OF FIGURES x

LIST OF TABLES xvi

LIST OF SYMBOLS xvii

LIST OF ACRONYMS/ABBREVIATIONS xxi

1. MOTIVATION 1

2. SCIENTIFIC BACKGROUND 4

2.1. Crystal Growth Methods 4

2.1.1. Solid Phase Growth 4

2.1.2. Solution Growth 4

2.1.3. Melt Growth 5

2.1.4. Vapor Phase Growth 6

2.2. Bulk Crystal Growth from the Melt 7

2.2.1. Available Methods 7

2.2.1.1. Verneuil Method. 7

2.2.1.2. Czochralski (Cz) Method. 8

2.2.1.3. Kyropoulos Method. 8

2.2.1.4. Floating Zone (FZ) Method. 10

2.2.2. VB, AHP, and AVC Methods 10

2.2.2.1. Vertical Bridgman (VB) Method. 11

2.2.2.2. Axial Heat Processing (AHP) Method and Submerged Heater Method (SHM). 11

2.2.2.3. Axial Vibrational Control (AVC) Method. 12
2.2.3. Thermodynamics and Kinetics of Growth 13
2.2.3.1. Equilibrium. 14
2.2.3.2. Nucleation and Atomic Scale Growth. 15
2.2.3.3. The solid/Liquid Interface in Crystal Growth. 18
2.2.4. Solute Redistribution and Interface Instability 20
2.2.4.1. Solute Redistribution. 20
2.2.4.2. Interface Instability. 24
2.2.5. Boundary Layers 27
2.2.6. Convection in the Melt 28
2.2.6.1. Natural Convection. 29
2.2.6.2. Forced Convection. 30
2.3. Numerical Simulation of Crystal Growth from the Melt 31
2.3.1. Governing Equations 32
2.3.2. Boundary Conditions 34
2.3.3. Available Methods/Approaches in Phase Change Problems 35
2.3.4. The Enthalpy-Porosity Method 36
2.3.5. ANSYS Fluent Simulation 36
2.3.5.1. Navier-Stokes (NS) Equations 37
2.3.5.2. ANSYS Fluent Solvers 37
2.3.5.3. Solution Methods 38
2.3.5.4. Spatial Discretization Schemes 38
3. MATERIALS AND METHODS 40
3.1. The VB/AHP/AVC Unit 40
3.1.1. Growth Chamber 41
3.1.2. Vacuum Enclosure 41

3.1.3. Translation Mechanism....43
3.1.4. Control System....43
3.2. Experimental Procedures....45
3.2.1. The Vertical Bridgman (VB) Method....45
3.2.2. The Axial Heat Processing (AHP) Method....46
3.2.3. The Axial Vibrational Control (AVC) Method....48
3.2.4. Characterization of the Grown Crystals....48
3.2.4.1. Metallography....48
3.2.4.2. Dopant Distribution Measurement....48
3.2.4.3. Illustration of Striation Lines....49
3.3. Numerical Simulation of the Grown Crystals....50
3.3.1. Geometry and Mesh Generation....51
3.3.2. Governing Equations and Boundary Conditions....52
3.3.3. Numerical Modeling and Discretization....54
4. RESULTS....57
4.1. VB-20-58....58
4.2. AHP-20-15....60
4.3. AHP-20-10 (S)....62
4.4. AHP-20-5....62
4.5. AHP-20-2 (S)....64
4.6. AHP-10-10....64
4.7. AVC-20-10-2-0.25....66
4.8. AVC-20-15-0.25-25....68
4.9. AVC-20-10-2-0.25-g1 (S)....71
4.10. AVC-20-10-2-0.25-g2 (S)....72
4.11. AVC-20-10-2-0.25-a10 (S)....73

4.12. AVC-20-10-2-0.25-a20 (S) 74
4.13. AVC-20-10-2-0.25-a30 (S) 75
5. DISCUSSION 76
5.1. Convective Flow 77
5.1.1. Gap Flow 77
5.1.2. Radial Temperature Gradient 78
5.1.3. Flow Velocity (V) 81
5.1.4. Growth Rate 85
5.1.5. Melt Height (h) 87
5.1.6. Vibrational Amplitude (A) and Frequency (f) 89
5.2. Axial and Radial Solute Distribution 93
5.3. Interface Shape and Stability 95
6. CONCLUSIONS 98
7. FUTURE WORK 100
REFERENCES 101

LIST OF FIGURES

Figure 2.1. Simplified diagram of the Verneuil process [52]. 8

Figure 2.2. Schematic setup of the Czochralski method [63]. 9

Figure 2.3. Schematic of the Kyropoulos crystal growth [66]. 9

Figure 2.4. Schematic of the floating zone method [75]. 10

Figure 2.5. Schematic representation of the VB crystal growth method. 11

Figure 2.6. Schematic representation of the AHP crystal growth method. 12

Figure 2.7. Schematic representation of the AVC crystal growth method. 13

Figure 2.8. Variation of the Gibbs free energy versus temperature in pure metals. 15

Figure 2.9. Free energy required for homogeneous and heterogeneous nucleation. 17

Figure 2.10. Types of solid/liquid interfaces. 18

Figure 2.11. Growth velocities versus kinetic undercooling for different mechanisms. 20

Figure 2.12. Solute composition in a schematic phase diagram. 21

Figure 2.13. Equilibrium solute redistribution. 22

Figure 2.14. Solute boundary layer with convection near the interface. 23

Figure 2.15. Solute distribution during solidification for different mechanisms.....24

Figure 2.16. Comparison of thermal and compositional gradients.....25

Figure 2.17. Schematic comparison between boundary layers in metallic melts.....28

Figure 3.1. the VB/AHP/AVC growth unit (a), vacuum enclosure and growth chamber (b), baffle-crucible-pedestal assembly (c). Labels are described in the text [177].....42

Figure 3.2. The VB/AHP/AVC unit at BUSCGLAB.....47

Figure 3.3. Four-point-probe schematic grid points.....49

Figure 3.4. Electrolytical etching system for striation lines illustration. (a) the solution (b) the TDK-Lambda voltage generator.....50

Figure 3.5. Dimensions of simulated domain and its discretization.....52

Figure 4.1. The etched surface of the VB-20-58 showing the single/poly crystal regions and striations (a). The initial temperature distribution, interface shape and flow pattern simulation (left-hand-side) and after 600 seconds (right-hand-side) (b). Longitudinal solute distribution (c). Radial solute distribution (d).....59

Figure 4.2. The etched surface of the AHP-20-15 showing the single/poly crystal regions and striations (a). The initial temperature distribution, interface shape and flow pattern simulation (left-hand-side) and after 600 seconds (right-hand-side) (b). Longitudinal solute distribution (c). Radial solute distribution (d).....61

Figure 4.3. Temperature distribution, interface shape and flow pattern in AHP-20-10 simulation after steady state (left) and 600 seconds (right). 62

Figure 4.4. The etched surface of the AHP-20-5 showing the single/poly crystal regions and striations (a). The initial temperature distribution, interface shape and flow pattern simulation (left-hand-side) and after 600 seconds (right-hand-side) (b). Longitudinal solute distribution (c). Radial solute distribution (d). 63

Figure 4.5. Temperature distribution, interface shape and flow pattern in AHP-20-2 simulation after steady state (left) and 600 seconds (right). 64

Figure 4.6. The etched surface of the AHP-20-5 showing the single/poly crystal regions and striations (a). The initial temperature distribution, interface shape and flow pattern simulation (left-hand-side) and after 600 seconds (right-hand-side) (b). Longitudinal solute distribution (c). Radial solute distribution (d). 65

Figure 4.7. The striations and single crystal length of the AVC-20-10-2-0.25. 67

Figure 4.8. Longitudinal solute distribution (a) and Radial solute distribution (b) in AVC-20-10-2-0.25. 67

Figure 4.9. Temperature distribution (right), interface shape (left), and flow pattern (left) in the AVC-20-10-2-0.25 after 601s at the top, 602s at the middle-down, 603s at the bottom, and 604s at the middle-up positions. 68

Figure 4.10.The striations and single crystal length of the AVC-20-15-0.25-25. 69

Figure 4.11. Longitudinal solute distribution (a) and Radial solute distribution (b) in AVC-20-15-0.25-25. 69

Figure 4.12. Temperature distribution (right), interface shape (left), and flow pattern (left) in the AVC-20-15-0.25-25 after 120.01s at the top, 120.02s at the middle-down, 120.03s at the bottom, and 120.04s at the middle-up positions. 70

Figure 4.13. Temperature distribution (right), interface shape (left), and flow pattern (left) in the AVC-20-10-2-0.25-g1 after 601s at the top, 602s at the middle-down, 603s at the bottom, and 604s at the middle-up positions. 71

Figure 4.14. Temperature distribution (right), interface shape (left), and flow pattern (left) in the AVC-20-10-2-0.25-g2 after 601s at the top, 602s at the middle-down, 603s at the bottom, and 604s at the middle-up positions. 72

Figure 4.15. Temperature distribution (right), interface shape (left), and flow pattern (left) in the AVC-20-10-2-0.25-a10 after 601s at the top, 602s at the middle-down, 603s at the bottom, and 604s at the middle-up positions. 73

Figure 4.16. Temperature distribution (right), interface shape (left), and flow pattern (left) in the AVC-20-10-2-0.25-a20 after 601s at the top, 602s at the middle-down, 603s at the bottom, and 604s at the middle-up positions. 74

Figure 4.17. Temperature distribution (right), interface shape (left), and flow pattern (left) in the AVC-20-10-2-0.25-a30 after 601s at the top, 602s at the middle-down, 603s at the bottom, and 604s at the middle-up positions. 75

Figure 5.1. The interface shapes observed in the grown crystals (left) and obtained by the simulation (right). 76

Figure 5.2. Initial stationary temperature distribution (right), interface shape (left) and flow pattern (left) in the VB, AHP, and AVC simulations obtained in the steady state solution. Note that h58 does not use a baffle. 78

Figure 5.3. Radial temperature profile in the VB and AHP simulations after 600 seconds at 6 millimeters above the seed base (solid curves) and after the initial steady state solution at 4 millimeters above the seed base (dashed curves). 79

Figure 5.4. Radial temperature gradient in the VB and AHP simulations after 600 seconds at different axial positions from the seed base. Longer times for AHP-20-10 and VB-20-58 are also shown. Large symbols show the s/l interface position and last data point is about 1 millimeter below the baffle base. 80

Figure 5.5. Radial temperature profile in the AVC simulations of baffle shape modification after 600 seconds at 7 millimeters above the seed base. 81

Figure 5.6. Velocity magnitude in the VB and AHP simulations for initial stationary solution (dashed curves) and after 600 seconds (solid curves) 1 millimeter above the interface at the center (a). Velocity magnitude in AHP-20-10 simulation from initial stationary condition (0 seconds) to 3000 seconds at 1 millimeter above the interface at the center. The lines at 2400s and 3000s overlap (b).....83

Figure 5.7. Maximum fluid velocity magnitude in all the VB and AHP simulations. 84

Figure 5.8. The interface position during the solidification process (a). Deviation between the pulling velocity and the interface velocity (b).....86

Figure 5.9. The interface position during the solidification process. Measured at the center line relative to the seed base. 87

Figure 5.10. The melt height during the solidification process (a). Simulated rate of increase in the melt height (b). 88

Figure 5.11. The melt height during the solidification process of AVC simulated cases with modified baffle shape. 89

Figure 5.12. Velocity magnitude in the AVC-20-10-2-0.25 at 8.3 millimeter above the seed base after 597s at the top, 598s at the middle-down, 599s at the bottom, and 600s at the middle-up positions. 91

Figure 5.13. Averaged radial solute segregation along the crystals. The values in the parentheses are the single crystal lengths. 95

Figure 5.14. The interface shape at different times during the solidification process in all the simulations. The lines shown in each sample (bottom-up) represent the interface position respectively at 0, 180, 420, 600, 1200, 1800, 2400, 3000, 3600, and 4200 seconds. In the AVC-20-15-0.25-25, the shown lines (top-down) represent the interface position respectively at 0, 5, 10, 20, 30, and 120 seconds. In this sample interfaces at 30 and 120 are overlapped, thus there are four visible lines. 97

LIST OF TABLES

Table 3.1. Material properties [21,181] 51

Table 4.1. Grown/simulated crystals and their growth parameters 58

Table 5.1. The maximum flow velocity when the baffle is at the top position, and the flow velocity in the annular gap when the baffle is at the middle-up position 84

LIST OF SYMBOLS

A	Vibration amplitude
A_{mush}	Mushy constant
A_{SL}	Solid/liquid interfacial area
c_p	Specific heat capacity
C_L	Solute concentration in the liquid
C_S	Solute concentration in the solid
C_{ref}	Reference concentration
D	Solute diffusivity
D_L	Solute diffusivity in the liquid
D_S	Solute diffusivity in the solid
e_g	Unit vector in the gravitational field
E	Internal energy
f	Vibration frequency
f_l	Liquid fraction
f_n	Frequency
f_L	Mass fraction in the liquid
f_S	Mass fraction in the solid
g	Gravitational acceleration/force
G	Gibbs free energy
G_1	Free energy of the initial homogeneous liquid system
G_2	Free energy of the system after nucleation
G_L	Liquidus (solutal) temperature gradient
G_T	Thermal gradient in the liquid
ΔG	Free energy change
ΔG_A	Free energy of activation for the transfer of atoms from liquid to solid
ΔG_{cr}	Required free energy to form a nucleus with critical size
ΔG_{cr}^{het}	Required free energy to form a heterogeneous nucleus of critical radius

ΔG_{cr}^{hom}	Required free energy to form a homogeneous nucleus of critical radius
ΔG_s	Critical free energy required to form a surface nucleation
ΔG_V	Free energy change per unit volume
h_c	Dimensionless interface position
h_{ref}	Reference enthalpy
ΔH	Latent heat
ΔH_f	Latent heat of fusion per unit volume
I_{het}	Heterogeneous nucleation rate
I_{hom}	Homogeneous nucleation rate
I_r	Current
k	Thermal conductivity
K	Partition coefficient / solute segregation coefficient
K_{eff}	Effective partition coefficient
k_B	Boltzmann's constant
k_{cg}	Continuous growth constant
k_{lg}	Lateral growth constant
l_m	Length of the molten zone
L	Enthalpy of the liquid
L_c	Characteristic length
m_L	Liquidus slope
n_L	Number of atoms
P	Pressure
Pr	Prandtl number
Q_l	Thermal heat flux in the liquid
Q_s	Thermal heat flux in the solid
R	Gas constant
Ra_T	Thermal Rayleigh number
r_{cr}	Critical radius
Rs	Resistivity
s	Distance between the probe needles
S	Source term

$\overline{S}$	Entropy
ΔS_f	Entropy of fusion
Sc	Schmidt number
St	Stefan number
t	Time
T	Temperature
T_m	Melting temperature
T_{ref}	Reference temperature
ΔT	Temperature difference
ΔT_c	Constitutional (compositional) undercooling
ΔT_k	Kinetic undercooling
$\overline{V}$	Volume
$\overline{V}_S$	Volume of the formed solid
V	Flow velocity
V_r	Voltage
V_g	Solid/liquid interface growth velocity
V_{cg}	Continuous growth velocity
V_{sp}	Spiral growth rate
w	Specific thermodynamic work
θ	Wetting angle
β_T	Thermal expansion coefficient
β_S	Solutal expansion coefficient
δ	Boundary layer
δ_C	Composition/solute/diffusion boundary layer thickness
δ_T	Thermal boundary layer thickness
δ_V	Velocity boundary layer thickness
λ	Wavelength
γ_{SL}	Solid/liquid interfacial free energy
γ	Density ratio of the solid and the liquid
ρ	Density

ρ_L	Density in the liquid
ρ_S	Density in the solid
τ_L	Thermal diffusivity in the liquid
ν	Kinematic viscosity
ω	Wave number

LIST OF ACRONYMS/ABBREVIATIONS

AHP	Axial Heat Processing
AVC	Axial Vibrational Control
CMOS	Complementary Metal-Oxide Semiconductor
CS	Constitutional Supercooling
Cz	Czochralski
FZ	Floating Zone
FVM	Finite Volume Method
IC	Integrated circuits
LPE	Liquid Phase Epitaxy
MBE	Molecular Beam Epitaxy
MOCVD	Metalorganic Chemical Vapor Deposition
MODFET	Modulation-Doping Field Effect Transistor
MOVPE	Metalorganic Vapor Phase Epitaxy
MS	Mullins-Sekerka
NS	Navier-Stokes
PID	Proportional Integral Derivative
PISO	Pressure-Implicit with Splitting of Operator
SCBG	Slow Cooling Bottom Growth
SCR	Silicon-Controlled Rectifier
SHM	Submerged Heater Method
SIMPLE	Semi-Implicit Method for Pressure Linked Equation
SIMPLEC	SIMPLE-Consistent
TMF	Traveling Magnetic Field
TSSG	Top-Seeded Solution Growth
TSZG	Traveling Solvent Zone Growth
VB	Vertical Bridgman
VGF	Vertical gradient freeze
VPE	Vapor Phase Epitaxy

1. MOTIVATION

Single crystals of semiconductor materials with precisely controlled compositions are vital to modern technologies, especially for telecommunications, electronics, energy harvesting, and energy conversion. They are used in many modern electronic devices such as transistors, lasers, and solar cells. One of the well-known semiconductors is germanium (Ge) which is a key material for a wide variety of applications as a result of its unique material characteristics. Integrated circuits (IC), lenses and windows for infrared optics, substrates for III-V based optoelectronic devices, detectors for gamma radiation, temperature sensors, high-resolution γ ray spectroscopy, triple-junction solar cells, terahertz emitters, modulation-doping field effect transistors (MODFETs), and modern complementary metal-oxide semiconductor (CMOS) technology have brought special attention to Ge-based structures in recent years. Recently the quality of Ge crystals has dominated the semiconductor market, and its improvements have mostly focused on detectors and the solar cells market. For example, the semiconductor industry currently faces problems with scaling down the transistor dimensions and achieving higher performance at lower cost per function with silicon technology. Germanium with its properties can help to solve these kind of problems [1,2].

Low melting point (938.3 °C) [3], resistance against oxygen [1], negligibly low vapor pressure at the melting temperature [4], low toxicity [5], moderate reactivity of molten germanium with graphite and quartz crucible materials [6], high crystallographic perfection [7], recyclability [8], and high mechanical strength [9] make Ge a popular substance and a practical competitor for other semiconductors in the industry. On the other hand, because of the problems such as the high density, fragility of bulk wafers, and high price, the use of bulk germanium wafers in the aforementioned applications is limited [1].

Large-scale crystals of semiconductor materials are attainable via melt growth techniques. Single crystal growth from the melt is a very complicated procedure that can be analyzed and controlled by many different techniques, all of which focus on parameters like temperature distribution and convective flow in the melt, formation of defects in the growing

crystal, shape and morphological stability of the solid/liquid (s/l) interface, and thermochemical reactions in the growth chamber. Moreover, the electrical properties of semiconductors can be altered in a controllable way by doping. Dopant homogeneity in the melt grown bulks is vital to guarantee reproducibility of wafer cuts with uniform electronic properties.

Segregation and morphological instability are two phenomena causing non-homogeneities in bulk single crystals. A homogeneous dopant distribution can be obtained with a planar and stable s/l interface. Thus, solidification conditions should be carefully controlled in a directional solidification setup to keep the s/l interface as flat as possible in order to reduce the amount of such defects. Several approaches such as the Czochralski (Cz) [10], floating zone (FZ) [11], travelling magnetic field (TMF) [12], and vertical Bridgman (VB) [13], etc. have been suggested to control the s/l interface shape [14,15]. These conventional methods do not satisfactorily fulfill this goal. In all these methods, radial heat flux from the furnace results in a radial temperature gradient in the melt, convective flow near the s/l interface, a non-planar interface, and a non-homogeneous dopant distribution. It also increases the defect density and interface instability.

The new axial heat processing (AHP) method and the submerged heater (SHM) method have been developed as alternative growth methods to improve the quality of grown crystals by reducing the melt height and generating axial heat flux to the s/l interface in a modified VB configuration [16]. Axial heat is supplied to the growth interface by either manufacturing the baffle from a high thermal conductivity material or by placing a heater inside the baffle. The axial vibrational control (AVC) is another novel method which is successful in controlling the melt flow to improve the crystal perfection [17-20].

This research is focused on antimony-doped germanium (Ge-Sb) single crystal growth from the melt. The Bridgman method and its derivatives are the best choice among the conventional crystal growth methods to grow germanium crystals. Since the ratio of the melt surface tension (591 mJ/m^2) to the density (5500 kg/m^3) in germanium is too small, it cannot support a floating zone of more than 1 cm diameter. Therefore, the floating-zone method cannot be used to grow germanium crystals commercially [1]. Although mostly the Czochralski method is being used to grow germanium single crystals, high radial

temperature gradient in the melt and strong convective flow lead to high solute segregation as well as non-planar s/l interfaces [21]. In addition, complexity of the growth system is a disadvantage in Czochralski method [21].

In the current study, antimony-doped germanium crystals have been grown experimentally in the VB, AHP, and AVC configurations with similar growth parameters. The homogeneity of the solute and stability of the interface in the grown single crystals have been investigated with regard to growth parameters such as the pulling velocity and temperature gradient which are common to all the methods, the effective melt height which is relevant to the AHP and AVC methods, and the amplitude and frequency of the vibrating baffle which are relevant to the AVC method. These influence the radial temperature gradient, convective motion of the melt near the s/l interface, and growth rate to control the shape of the interface.

Optimizing the directional solidification parameters such as melt height and convection can help to increase the growth rate, and simulations offer a low-cost alternative to experimental optimization. Therefore, in addition to growing crystals experimentally, the same growth procedures have been simulated with the solidification module in ANSYS Fluent v15 to better understand the experimental outcomes. Moreover, in order to enhance single crystal length and quality, optimal combinations of the aforementioned solidification parameters are sought.

2. SCIENTIFIC BACKGROUND

Crystal growth is a process of arranging atoms, ions, or molecular assemblies into a periodic solid structure. Mainly, the presence of different types of disorder and defects make crystals imperfect. Since solids are polycrystalline in nature, numerous methods have been employed to obtain high quality and perfect single crystals of a preferred shape and size.

2.1. Crystal Growth Methods

Crystalline materials can be grown from bulk to small and even nanoscale sizes with various physical properties. They can be grown from solid, liquid, and gas. Due to a broad range of crystal growth processes, this section briefly covers most important growth techniques. The specific methods used in this research are described in more detail.

2.1.1. Solid Phase Growth

The solid phase growth is based on atomic diffusion. It is usually a slow process except in the case of fast ionic (superionic) conductors. The common solid phase growth methods are devitrification [22], annealing (sintering) [23], heat treatment [24], strain annealing [25], polymorphic phase transformations [26], precipitation hardening [27], etc. These methods are being used for adapting material properties.

2.1.2. Solution Growth

Solution growth is being used to grow a variety of crystalline products in technology and daily life e.g. foods, pesticides, medicines, etc. Growth of a crystal from solution can be divided into three types: flux (high-temperature solution) growth, hydrothermal (superheated aqueous solution) growth, and low-temperature aqueous solution growth [28]. This division is contingent on the nature of the solvent and solute, the temperature, and the pressure.

The Flux growth [29] is advantageous for growing crystals below their melting temperature and it supports an extensive range of substances. This method is useful for

growth of single crystals and liquid phase epitaxies (LPEs). In this method, the presence of flux ions in the final crystals (as impurities) is inevitable which is a disadvantage. The basic oxides, fluorides, or a mixture of them are commonly used fluxes. Flux growth can be achieved through spontaneous nucleation on a seed, and numerous types of flux growth such as slow cooling bottom growth (SCBG) to grow high-quality and large tetragonal lysozyme crystals [30], traveling solvent zone growth (TSZG) to grow GaAs [31] and $La_{2-x}SrxCuO_4$, Sr_2CuO_3, and $SrCuO_2$ [32], top-seeded solution growth (TSSG) to grow single crystals of $KHo(WO_4)_2$ [33] and $LiNbO_3$ [34], etc., are developed.

The hydrothermal growth is applicable for mixtures with low solubility and phase transitions. It is the means of many large size single crystals formed in nature like beryl crystals and created by man like quartz crystals [35]. The hydrothermal growth happens in the presence of aqueous solvents under high- temperature and pressure conditions [36]. If there are non-aqueous solvents in the system, this method is called solvothermal growth [37].

The low-temperature aqueous solution growth methods [38] are beneficial due to accurate control of supersaturation and growth conditions in ambient temperature and pressure which helps to minimize both equilibrium and non-equilibrium defects and thermal shocks [28]. These methods are applicable to materials with moderate and high solubility [28]. Small thermally generated strains in the grown crystals are due to low temperature gradient. The main disadvantage of this method is the slow growth rate (0.1 to 10 mm per day) [39].

2.1.3. Melt Growth

This method is the most popular one to grow large scale single crystals of semiconductors, metals, halides, oxides, chalcogenides, etc. with high rate of growth. In this method, the material needs to be melted without decomposition. Moreover, chemical reactions are undesired. Thus, the crystallization process has to occur in vacuum or in an atmosphere neutralized by helium, argon, or nitrogen. The temperature gradient in the melt results in convective flows which cause some defects (physical and chemical) in bulk melt growth methods. Crystals grown from small melt volumes are affected by diffusion, though. The proper melt growth method is selected depending on the physical and chemical features

of the materials to be crystallized. Typically, the Bridgman-Stockbarger method is used to grow single crystal of metals (germanium melt shows metallic characteristics) with melting points less than 1800℃ while metals with melting points greater than 1800℃ are grown by floating zone method [28]. For growing semiconductors, Czochralski and floating zone are the popular methods. To produce single crystals of dielectrics the Bridgman-Stockbarger or Czochralski methods (for melting points less than 1800℃) and Verneuil method (for higher melting points) are more useful. The Kyropoulos method is another melt growth method, very similar to Czochralski method, which was very popular for growing large scale crystals. The aforementioned methods are useful to grow a wide range of materials, such as SiGe [40], CdTe [41], Pb3MgNb2O9 [42], SrTiO3 [43]. The melt growth methods are explained more specifically in sections 2.2.1 and 2.2.2.

2.1.4. Vapor Phase Growth

Vapor phase growth is known as a low cost method to produce crystals for electronic devices (especially semiconductors) and epitaxial structures [44]. Growing crystals with this method results in few of point defects and low dislocation densities in comparison to melt grown crystals. This is because growth occurs at temperatures much lower than the melting temperature. Vapor phase growth is commonly used to grow substrates, thin films, and epitaxial layers in the semiconductor industry. Vaporization, transportation, and deposition are three steps of crystal growth with this method [44]. A solid or liquid is vaporized by heating. The kinetic energy of vaporization drives the vapor through a vacuum. Then, condensation or chemical reaction deposits the vapor to the growing crystal surface.

Vapor phase growth methods are distinguished according to their source material and the mechanisms of deposition. The most popular method is the vapor phase epitaxy (VPE) for growing III-V compounds of semiconductors such as GaAs [45], AlGaAs [46], GaInP [47], InGaAs [48], and GaSe [49], which are hard to attain by other methods. Metalorganic vapor phase epitaxy (MOVPE), plasma assisted molecular beam epitaxy (MBE), metalorganic chemical vapor deposition (MOCVD), etc. are suitable to grow these compounds as well [50].

2.2. Bulk Crystal Growth from the Melt

Bulk crystal growth of metals, especially semiconductors, with controlled microstructure is possible with melt growth methods. Different methods for growing crystals from the melt have been proposed. In these methods, an imposed temperature gradient forms the s/l interface at the position of the melting temperature isotherm. Then, by moving the crystal container or the temperature gradient, the crystal starts to grow. To achieve the desired compositional properties and high quality crystals, the thermodynamics and kinetics that govern solidification phenomena should be considered.

2.2.1. Available Methods

This section introduces some conventional methods to grow high quality crystals from the melt which are not utilized in this research. The next section describes the crystalized methods in detail.

2.2.1.1. Verneuil Method. The Verneuil (flame fusion) method is a conventional method to grow large amounts of high quality single crystals such as rutile, corundum, spinel, and strontium titanate in the laser industry and as substrates in thin film technologies. However, it was primarily developed by Auguste Verneuil [51] (a French chemist) in 1902 for producing synthetic gemstones. As it is shown in Figure 2.1, in a Verneuil setup, there is a furnace in which a seed crystal on a support rod is being fed from a highly fine powder material charge from the top. The system is supplied with oxygen and hydrogen. The oxygen from the top continuously release the source material through a tube into a hydrogen/oxygen flame (about 2200℃) above the growth region. The fine powder melts as it passes through the flame and falls on the growing crystal. As droplets are feeding the seed, the support rod will be pulled down slowly while rotating letting a cylindrical single crystal grow. Normally, the grown crystal is about 100 mm long and 15 to 20 mm wide. The cross section of the grown crystal is not essentially circular.

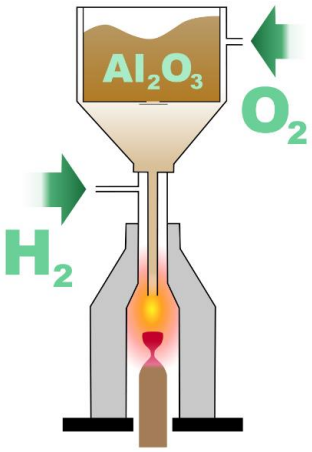

Figure 2.1. Simplified diagram of the Verneuil process [52].

2.2.1.2. Czochralski (Cz) Method. Jan Czochralski in 1917 [10] invented a method for crystal growth from a melt which was one of the first methods to grow large size single crystals which could not be grown by other melt growth methods in large quantities. This method is the most popular method for silicon single crystal production in the electronics industry [53-55]. The Czochralski method is schematically illustrated in Figure 2.2. The chamber, which is surrounded by a constant temperature furnace, contains the charge melt. A rotating rod, called the pull rod, holds a single crystal seed which is dipped in the feed melt. By pulling the rod up, crystallization at the s/l interface starts with a virtually constant growth rate. In this method, since the crystal has no contact with the crucible's wall, the thermal expansion coefficient difference cannot cause stress-induced defects in the crystal. This is the main advantage of the Czochralski method. The absence of crucible in this method results in problems such as difficulty in shape control and reproducibility, although adjusting the pull rate, rotation rate, and heating power can help to control the growing crystal's diameter. This method is being used for growing several semiconductor alloys like Ge-Si [56-58], $Bi_2ZnOB_2O_6$ [59], YAG [60], and $Zn_2Te_3O_8$ [61]. However, high radial temperature gradient in the melt and strong convective flow cause a high solute segregation other than a non-planar s/l interface [21]. Moreover, the growth system is complicated in this method.

2.2.1.3. Kyropoulos Method. The Kyropoulos method invented by Spiro Kyropoulos [62] in 1926 was one of the most popular methods to grow large single crystals.

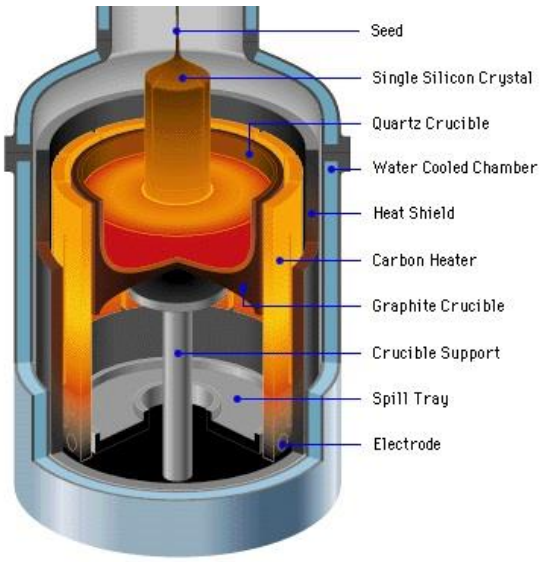

Figure 2.2. Schematic setup of the Czochralski method [63].

In this method, similar to the Czochralski method, the source material should be melted inside a crucible. However, in this method instead of pulling the seed out of the melt inside a constant temperature heater, the crystal grows towards the melt while the melt smoothly cools down. As a result, crystal's diameter increases and the melt level decreases. The s/l interface and the final crystal shape are the main difference between these two methods. The final crystal has a diameter at most equal to the diameter of the crucible and an ellipsoid shape. Thus, crystals grown by Kyropoulos method can obtain larger diameters than the crystals grown by Czochralski method. The most important use of this method is growing alkali halides to produce optical components [64,65]. Figure 2.3 shows a schematic of crystal growth by this method.

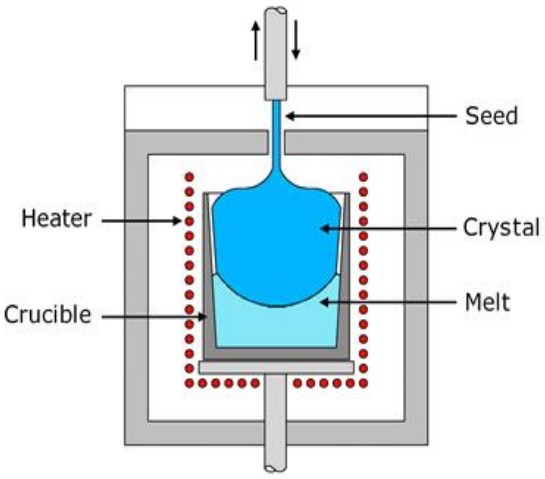

Figure 2.3. Schematic of the Kyropoulos crystal growth [66].

2.2.1.4. Floating Zone (FZ) Method. William Gardner Pfann [67] invented this method in Bell Laboratories for the purification of semiconductor alloys. In this method, as it is shown in Figure 2.4, initially a single crystal seed is in contact with a polycrystalline ingot charge. A heating coil, which is positioned around the seed-ingot contact interface melts a thin layer of the seed and the charge. Thus, two s/l interfaces will be formed. By pulling the seed downward, the melt above the seed starts to solidify through the lower s/l interface, and the polycrystalline ingot feeds the melt zone between the two s/l interfaces. Keeping the melt zone stability is the main difficulty of this method. However, this method is very advantageous for growing pure semiconductors and alloys with high segregation coefficients [68-74]. Nevertheless, germanium with a very small ratio of the melt surface tension (591 mJ/m^2) to the density (5500 kg/m^3) cannot support a floating zone of more than 1 cm diameter [1].

2.2.2. VB, AHP, and AVC Methods

Since this study is about antimony-doped germanium semiconductor crystal growth using the VB, AHP, and AVC methods, this section is focused on the growth methods suitable to grow Ge single crystals.

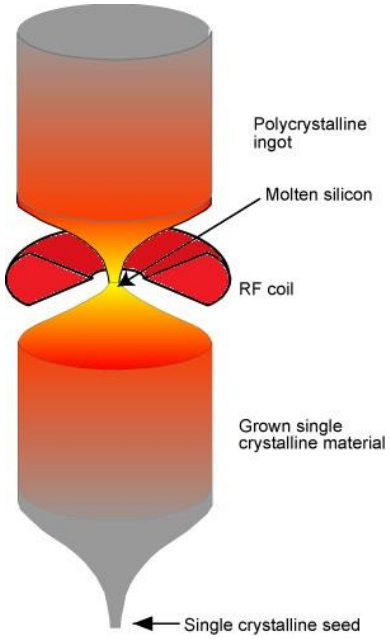

Figure 2.4. Schematic of the floating zone method [75].

2.2.2.1. Vertical Bridgman (VB) Method. The VB method was invented by Percy Williams Bridgman [76] in 1928 with a single heating zone. Donald C. Stockbarger [77] developed the method in 1936 further by adding a lower temperature heater below the first (each controlled independently) and creating a positive axial temperature gradient in the melt chamber. This method with the final configuration, shown in Figure 2.5, is still one of the popular single crystal growth methods. In this method, the polycrystalline charge is placed on a single crystal seed positioned on the bottom of the crucible. A tubular furnace, surrounding the crucible, applies heat in such a way that the charge and a portion of the seed melt. By pulling the crucible down inside the furnace, the crystallization process begins. This method, due to the simplicity of the apparatus and its control, is very common in growing compound semiconductor crystals [78-82]. Germanium is usually grown with the vertical Bridgman method. This method supplies heat radially to the melt, leading to a radial temperature gradient, a non-planar interface, and a non-homogeneous dopant distribution. Still, this method is the best choice among the other conventional crystal growth methods for growing Ge crystals.

2.2.2.2. Axial Heat Processing (AHP) Method and Submerged Heater Method (SHM). The AHP method was designed and patented by Vladimir D. Golyshev and Michael A. Gonik [83].

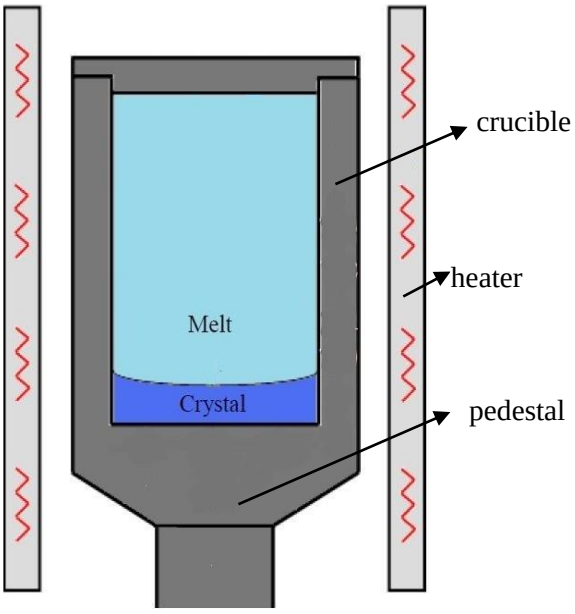

Figure 2.5. Schematic representation of the VB crystal growth method.

This method is a modification of the VB method by immersing a baffle in the melt. Thus, the melt height is decreased. Axial heat is supplied to the growth interface by manufacturing the baffle from a high thermal conductivity material and/or by placing a heater inside the baffle. Concurrently, the SHM method was developed and patented by Aleksandar G. Ostrogorsky [84,85] which is essentially the same as the AHP method. Reducing the melt height and axial heating over the entire s/l interface decrease the radial temperature gradient and the buoyancy driven convection in the melt near the interface [86-88] and consequently promotes a planar interface. The submerged baffle separates the melt into two regions. A small annular gap between the baffle and the crucible, which allows the bulk liquid to flow from the feeding region to the growth region, minimizes any back diffusion of the solute into the bulk liquid above the baffle, and improves the uniformity of the dopant distribution. The AHP and SHM methods are schematically demonstrated in Figure 2.6. These methods have been successfully used to grow many semiconductor alloys such as GeSb [21,87-92], Ga-doped $Ge_{0.98}Si_{0.02}$ [93], $Li_2B_4O_7$ [94], $Bi_4Ge_3O_{12}$ [95], GaSb [96], and GeSi [40,97,98].

2.2.2.3. Axial Vibrational Control (AVC) Method. The AVC method has the same equipment configuration as the AHP and SHM methods. As it can be seen in Figure 2.7, the only difference in this method is the axial vibrational motion of the baffle. In the VB, AHP,

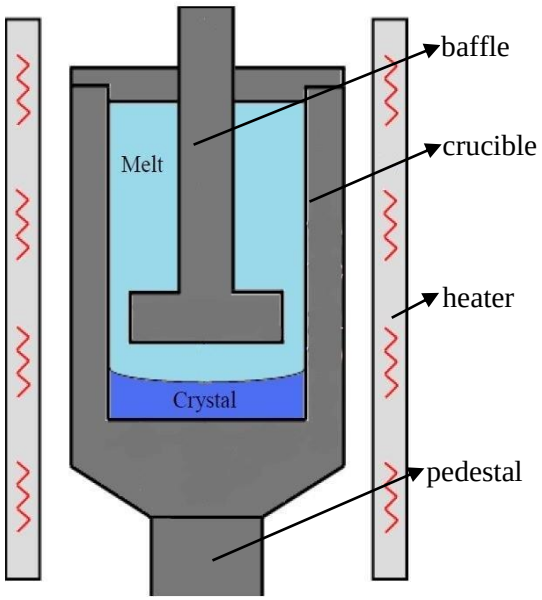

Figure 2.6. Schematic representation of the AHP crystal growth method.

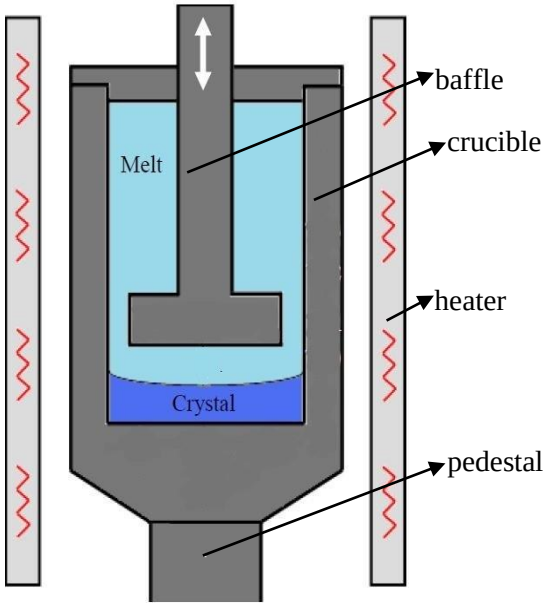

Figure 2.7. Schematic representation of the AVC crystal growth method.

and SHM methods, the fluid flow close to the s/l interface leads to solute accumulation in the middle of the growing crystal. Since the solute concentration changes the melting temperature, the center of the interface deflects into the solid and increases the instability of the interface. The axial oscillation of the submerged baffle during crystallization, by stirring the melt in the growth region, can suppress or modify these convective flows [17] providing more homogeneous solute distribution and promoting stable planar interface during growth. This method has been used to grow PbTe [99], CdTe [100], and NaNO3 [101] crystals in the VB configuration and is also applicable in the Czochralski [102-104] and floating zone [105-107] configurations. In this study, the term "AVC" has been used for the AVC in the VB configuration for simplicity. Several numerical simulations have been also performed to analyze the growth parameters and flow pattern in this method with different configurations [18,19,102,103,108,109].

2.2.3. Thermodynamics and Kinetics of Growth

The phase transformation process from liquid to solid is called solidification, and involves many physical effects. This process can be analyzed mathematically by using thermodynamics and kinetics. Many studies have been conducted to understand this complex phenomenon, especially at the solid/liquid (s/l) interface where the transformation occurs.

Thermodynamics is very powerful at predicting whether a solidifying system is in equilibrium. Estimating the solidification path, and the slopes of liquidus and solidus phase boundaries. However, it cannot determine the rate at which equilibrium is reached. The following subsection briefly explains the thermodynamics and kinetics of the solidification process at equilibrium. This content is comprehensively covered in [110,111].

2.2.3.1. Equilibrium. A phase transformation occurs because of the relative stability of a system in its final state, which can be determined by thermodynamics at constant temperature and pressure. This relative stability is determined by the Gibbs free energy (G) of the system.

$$G = E + P\overline{V} - T\overline{S} \tag{2.1}$$

where E is the internal energy, P is the pressure, $\overline{V}$ is the volume, T is the absolute temperature, and $\overline{S}$ is the entropy of the system. The most stable state of the system occurs when it has the lowest value of the Gibbs free energy, that is called the equilibrium state.

In metallic alloys, the solid and liquid compositions can be determined with an assumption of local thermodynamic equilibrium. The result of this assumption is equilibrium phase diagrams which describe a system as a function of composition and temperature, assuming the transformation rate is extremely slow or species diffusion rate is very fast. The free energy of a pure metal varies with temperature at a constant pressure as shown in Figure 2.8. In this figure, the line with greater slope is the liquid free energy line, the other one is the solid free energy line, and the intersection point shows the melting temperature. For temperatures higher than the melting temperature, the free energy of the solid is more than the free energy of the liquid, while for temperatures lower than that, this relation is reversed. This indicates that at temperatures higher than the melting temperature, the liquid phase is the stable phase and vice versa. For the solidification process to start, a finite undercooling ΔT from the equilibrium temperature is required. In appropriate conditions, the liquid can stay undercooled with no phase transformation. Thermodynamics relates the undercooling to the driving force for solidification, but fails to give information about the rate of the phase transformation. In fact, kinetics determines this rate.

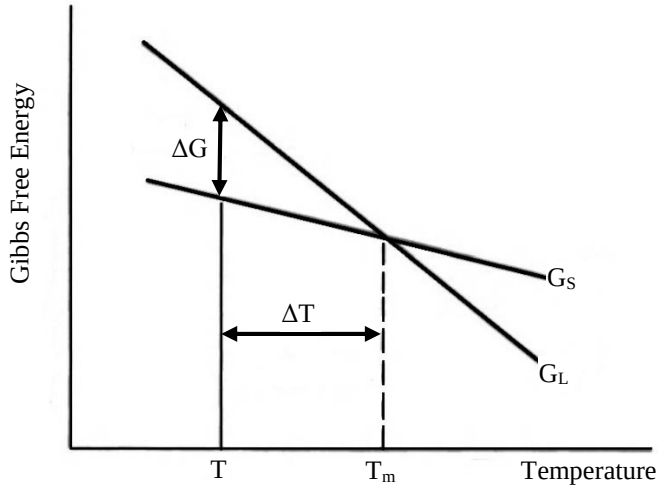

Figure 2.8. Variation of the Gibbs free energy versus temperature in pure metals.

2.2.3.2. Nucleation and Atomic Scale Growth. The nucleation phenomenon is the creation of stable clusters of solid in the liquid at the atomic scale, and is the basis of the solidification process. When the solid is nucleated, the s/l interface dynamics and the grain growth rate affect the solidification undercooling, diffusive/convective energy transfer, and interface shape.

Homogeneous nucleation in a liquid occurs when atoms of the liquid randomly fluctuate and cluster together to form a spherical solid [112]. In this nucleation, the free energy associated with the transformed volume and created s/l interfacial area of the atomic spherical cluster (ΔG) changes the free energy of the initial homogeneous liquid system (G_1). Thus, the free energy of the system after nucleation (G_2) is:

$$G_2 = G_1 + \Delta G \tag{2.2}$$

$$G_2 = G_1 - \overline{V}_S \cdot \Delta G_V + A_{SL} \cdot \gamma_{SL} \tag{2.3}$$

$$\Delta G_V = \Delta H_f \, \Delta T / T_m \tag{2.4}$$

where $\overline{V}_S$ is the volume of the formed solid, A_{SL} is the s/l interfacial area of formed solid, γ_{SL} is the s/l interfacial free energy, ΔG_V is the free energy change per unit volume of formed solid, ΔH_f is the latent heat of fusion per unit volume, and T_m is melting temperature. According to the Equation 2.3, the transformed volume has a negative contribution in free

energy change, while the interfacial free energy increases the total free energy. By assuming a spherical cluster and equating the first derivative of Equation 2.3 with respect to r, to zero, a critical radius r_{cr} can be derived as:

$$r_{cr} = 2\gamma_{SL}/\Delta G_V \tag{2.5}$$

The free energy of the system decreases as atoms add to the spherical cluster and increase the radius. Thus, a solid particle with $r > r_{cr}$ is stable. This particle is called a *nucleus*. In addition, the required free energy to form a nucleus with critical size ΔG_{cr} can be derived from Equations (2.3) and (2.5):

$$\Delta G_{cr} = \frac{16\pi {\gamma_{SL}}^3 {T_m}^2}{3{\Delta H_f}^2}\frac{1}{\Delta T^2} \tag{2.6}$$

For n_L atoms per unit volume of the liquid which attach to the solid nucleus, the homogeneous nucleation rate I_{hom} is:

$$I_{hom} = f_n n_L \exp\left(-\frac{\Delta G_{cr}+\Delta G_A}{k_B T}\right) \tag{2.7}$$

where f_n is the frequency with which atoms from liquid attach to the solid nucleus, ΔG_A is the free energy of activation for the transfer of atoms from liquid to solid, and k_B is Boltzmann's constant. The nucleation typically takes place when ΔG_A is greater than ΔG_{cr} and is defined by the probability of adequate energy fluctuation to overcome the activation boundary. Kinetics dictates that the system has to overcome a critical undercooling to form a nucleus while thermodynamics suppose that solidification occurs at any undercooling.

In real solidification, because of the relatively large required activation energy to form a nucleus (ΔG_{cr}^{hom}), homogeneous nucleation is a hard way to form crystals. Homogeneous nucleation occurs within the bulk, while *heterogeneous nucleation* occurs at interfaces like the walls of the container or solid impurity particles in the liquid. The free energy required to form a heterogeneous nucleus of critical radius (ΔG_{cr}^{het}) on a nucleant can

be expressed as a product of the nucleus shape factor (f) and the critical free energy of homogeneous nucleation (ΔG_{cr}^{hom}):

$$f(\theta) = 0.25(2 + cos\theta)(1 - cos\theta)^2 \tag{2.8}$$

$$\Delta G_{cr}^{het} = f(\theta)\Delta G_{cr}^{hom} \tag{2.9}$$

where θ is the wetting angle which is defined as the angle between the growing nucleus surface and the substrate nucleant wall. $f(\theta)$ is always less than one, which means that heterogeneous nucleation starts at a lower undercooling. This fact is shown in Figure 2.9 by comparing ΔG^{hom} and ΔG^{het}.

Similar to homogeneous nucleation, the heterogeneous nucleation rate is defined as:

$$I_{het} = f_n n_S \exp\left(-\frac{\Delta G_{cr}^{het} + \Delta G_A}{k_B T}\right) \tag{2.10}$$

where n_S is the number of atoms in contact with heterogeneous sites per unit volume, and I_{het} is the homogeneous nucleation rate.

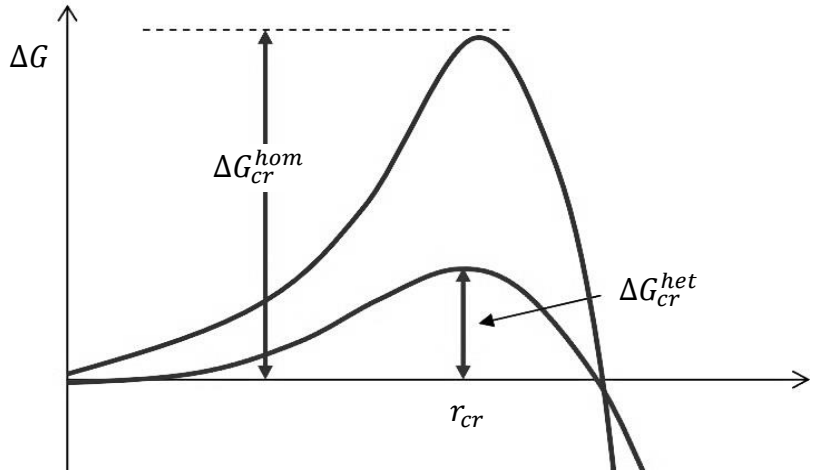

Figure 2.9. Free energy required for homogeneous and heterogeneous nucleation.

2.2.3.3. The solid/Liquid Interface in Crystal Growth. The next step after nucleation is growth, where the s/l interface grows toward the melt. For this process, two types of interfaces can be considered; atomically rough (diffuse) interfaces and atomically smooth (flat) interfaces. Diffuse interfaces migrate by *continuous growth*, whereas flat interfaces typically advance by the *lateral growth* of ledges resulting from surface nucleation or dislocations intersecting the interface. Continuous growth leads to a *non-faceted* s/l interface while lateral growth results in a *faceted* s/l interface. Figure 2.10 illustrates a schematic of these two types of interfaces.

Whether an interface is faceted or non-faceted depends on the non-dimensional ratio (α) of the entropy of fusion (ΔS_f) and the ideal gas constant (R). This value is less than 2 for regular metals and some organics, which have non-faceted interfaces. For semi-metals and semiconductors such as Bi, Sb, Ga, Ge, and Si, with faceted s/l interfaces, this value is between 2.2 and 3.2. For most inorganics including carbides and nitrides, α is more than 3.5 and they grow with faceted interfaces [113]. The rate of continuous growth is typically controlled by heat transfer to the interfacial region for pure materials and by solute diffusion for alloys.

In diffuse interfaces, atoms can be received anywhere on the solid interface and the equilibrium configuration of the interface will not be disrupted. The kinetics of *continuous growth* was described by David Turnbull in 1949 [114]. He defined the continuous growth velocity as:

$$V_{cg} = k_{cg}\Delta T_k \tag{2.11}$$

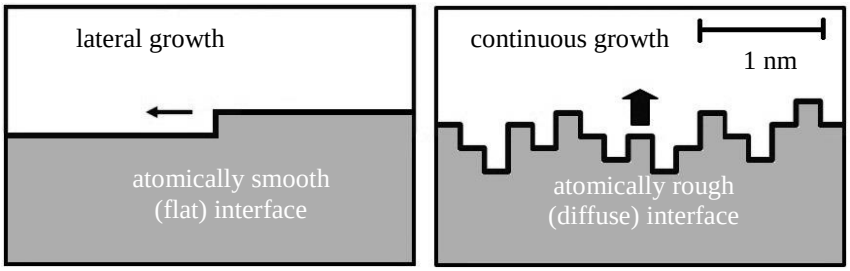

Figure 2.10. Types of solid/liquid interfaces.

where k_{cg} is the continuous growth constant, and ΔT_k is the required kinetic undercooling very low kinetic interfacial undercooling (ΔT_k) results in normal rates of solidification. Therefore, the s/l interface can be assumed to be at the equilibrium melting temperature and ΔT_k can be ignored. Pure metals grow at a rate controlled by heat diffusion while alloys solidify controlled by solute diffusion [115].

Smooth s/l interfaces are expected to advance by the *lateral growth* of ledges and jogs. Since these sites are non-equilibrium features of the interface, atoms arriving to them minimize the number of broken solid bonds and the free energy. Different equations can describe the kinetics of lateral growth according to the growth mechanism. Here, growth by screw dislocations and growth by surface nucleation are discussed. Screw dislocations create a step or ledge on the surface of the crystal. The ledge rotates about the point where the dislocation intersects the interface as atoms attach to it, and never leaves the interface. Subsequently, as growth continues, the ledge develops into a growth spiral with a constant angular velocity until it reaches equilibrium with the surrounding liquid and stops growing. The normal spiral growth rate (V_{sp}) has a parabolic relation with the kinetics undercooling (ΔT_k).

$$V_{sp} = k_{lg} {\Delta T_k}^2 \tag{2.12}$$

where k_{lg} is the lateral growth constant.

Surface nucleation occurs when adequate amount of atoms reaches the s/l interface, bundle and form an island. The critical free energy required for surface nucleation is:

$$\Delta G_s = \frac{\pi a {\gamma_{SL}}^2 T_m}{\Delta H_f \, \Delta T} \tag{2.13}$$

and the relation between the growth velocity and kinetic undercooling for surface nucleation is given by David Turnbull [116] as:

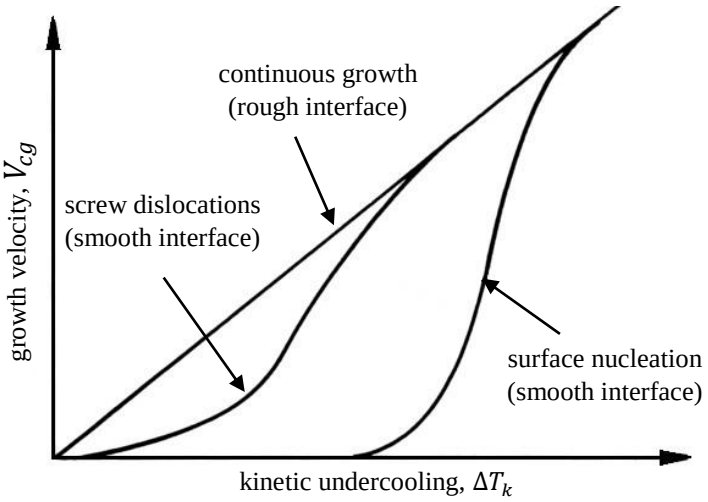

Figure 2.11. Growth velocities versus kinetic undercooling for different mechanisms.

$$V_{su} \propto exp\left(\frac{1}{3\Delta T_k}\right) \tag{2.14}$$

The variations of growth velocity according to the kinetic undercooling for continuous growth, spiral growth, and surface nucleation are given in Figure 2.11. Note that for a given solid growth velocity, the required undercooling at the interface for the continuous growth of rough interfaces is the least. For a given undercooling, the growth with screw dislocations mechanism normally is more significant than surface nucleation.

2.2.4. Solute Redistribution and Interface Instability

Since large scale semiconductor materials with homogeneous dopant distribution in microelectronic industry are widely demanded, prediction and control of solute distribution in the crystal growth process is essential. During growth, solute redistribution, heat transfer, and fluid flow significantly affect the interface morphology and result in perturbation at the s/l interface.

2.2.4.1. Solute Redistribution. Several theoretical models have been developed to predict the solute distribution in the crystal growth process. Some of the most important ones are reviewed in this section. The *equilibrium partition coefficient* (K) is the ratio of the solute concentration in the solid (C^*_S) and the solute concentration in the liquid (C^*_L) at the s/l

interface in local equilibrium conditions at constant pressure and temperature. The superscript "$*$" represents the values at local equilibrium near the s/l interface.

$$K = \left(\frac{C^*_S}{C^*_L}\right)_{T,P} \tag{2.15}$$

According to the Ge-Sb phase diagram, for this system K is less than 1. Therefore, the equations in this section are considered for $K < 1$. In this condition, solute concentration of the solidifying liquid in the *diffusion (solutal) boundary layer* ahead of the interface decreases from C^*_L to the concentration in the bulk liquid. The thickness of the diffusion boundary layer (δ_C), by assuming no convection in the liquid, is the distance from the interface determined by the growth velocity (V_g) and the solute diffusivity in the liquid (D_L) as follows.

$$\delta_C = D_L/V_g \tag{2.16}$$

(i) When either there is enough time for the solute to become homogeneously distributed in the solid and the liquid, the solidification is in *equilibrium* conditions and the solute completely diffuses in the liquid ($D_L = \infty$) and in the solid ($D_S = \infty$). As it is shown in Figure 2.12, during the solidification process, C_S and C_L vary as temperature changes.

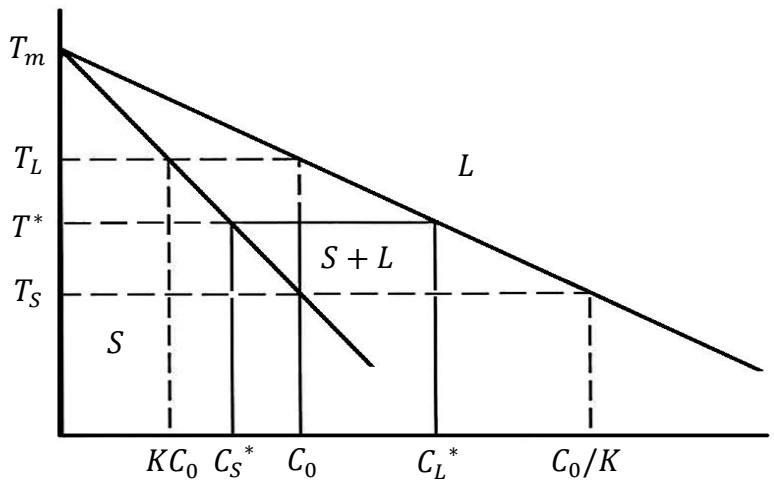

Figure 2.12. Solute composition in a schematic phase diagram.

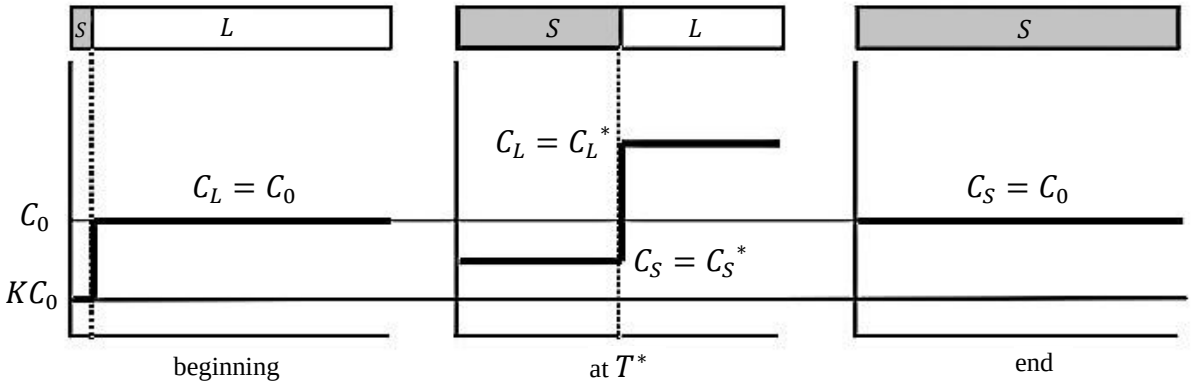

Figure 2.13. Equilibrium solute redistribution.

Figure 2.13 shows the solute distribution at the beginning, in the middle, and at the end of solidification process. The composition in the liquid, at the beginning of solidification, is equal to the total amount of the solute ($C_L = C_0$) and in the solid it is KC_0. When the interface temperature is T^*, C_S is still less than C_0 and C_L is more than C_0 (C_S=KC_L). Conservation of solute at T^* results in *the equilibrium lever rule* equation [117]:

$$C_S f_S + C_L f_L = C_0 \tag{2.17}$$

$$f_S + f_L = 1 \tag{2.18}$$

$$C_S = \frac{KC_0}{1-(1-K)f_S} \tag{2.19}$$

where f_S and f_L are mass fractions in the solid and the liquid respectively. At the end of solidification process, due to the fast solid diffusion, the solute is uniformly distributed along the solid ($C_S = C_0$). Equation (2.19) is valid when the densities in the solid and the liquid are equal ($\rho_S = \rho_L$). When $\rho_S \neq \rho_L$, by using volume fractions, g_S and g_L, instead of mass fractions, a similar equation can be derived [117]:

$$C_S = KC_0 \frac{1-(1-\rho_S/\rho_L)g_S}{1-(1-\rho_S/\rho_L)g_S} \tag{2.20}$$

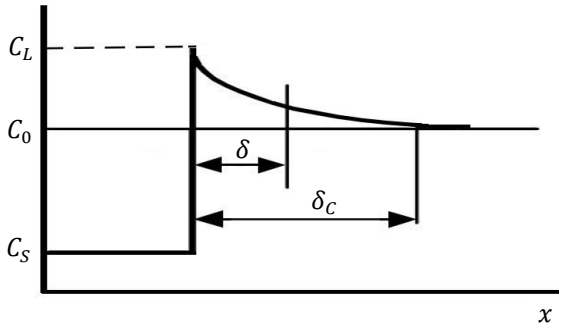

Figure 2.14. Solute boundary layer with convection near the interface.

Diffusion in the solid can be assumed to be negligible. Even then, the mixing in the liquid can be diffusional or convectional. A temperature gradient in the liquid, due to the density difference between the hot and cold material, results in thermal convection. Thus, mass transfer in most cases is due to both diffusion and fluid flow (convection). In fact, solute transport in the diffusion layer of thickness δ is only diffusional (the convection is ineffective) and beyond that, convection homogenizes the solute in the liquid. The boundary layer thickness (δ) at this condition is schematically shown in Figure 2.14. In this case, the solute distribution in the solid is given by the following:

$$C_S = K_{eff} C_0 (1 - f_S)^{K_{eff}-1} \tag{2.21}$$

The concept of effective partition coefficient (K_{eff}), is introduced by Jonathan A. Burton *et al.* from boundary layer theory [118] as follows to account for the convective solute transport.

$$K_{eff} = \frac{K}{K+(1-K)\exp(-V_g \delta / D_L)} \qquad K \leq K_{eff} \leq 1 \tag{2.22}$$

When the solute transfer in the liquid is only via convective flow and the melt above the interface is completely mixed (D_L is infinity), K_{eff} is equal to K and the following equation results:

$$C_S = K C_0 (1 - f_S)^{K-1} \tag{2.23}$$

This equation is known as the non-equilibrium lever rule or the Scheil equation [117]. This case is seen in most of the directional solidification experiments under the earth's gravitational field. When the convective mixing in the melt is prevented, such as in microgravity, a diffusional-mixing model is more accurate. In this case, the solute distribution in the solid is given by the following expression [117]:

$$C_S = C_0\left[1 - (1 - K)exp\left(-KxV_g/D_L\right)\right] \tag{2.24a}$$

The solute redistribution in the AHP method, however, resembles that in the floating zone (FZ) method. In this case, an active melt region solidifies at one boundary and melts at the opposing boundary. In this configuration, the solute content in the solid during initial transient is given as follows [117]:

$$C_S = C_0[1 - (1 - K)exp(-Kx/l_m)] \tag{2.24b}$$

where l_m is the length of the molten zone. Figure 2.15 plots the solute distribution during the solidification in all aforementioned models together.

2.2.4.2. Interface Instability. The compositional and thermal fields ahead of s/l interface affect its morphological stability. If any interface perturbation is controlled and damped during growth, the interface will be stable, otherwise it is unstable and results in crystal defects.

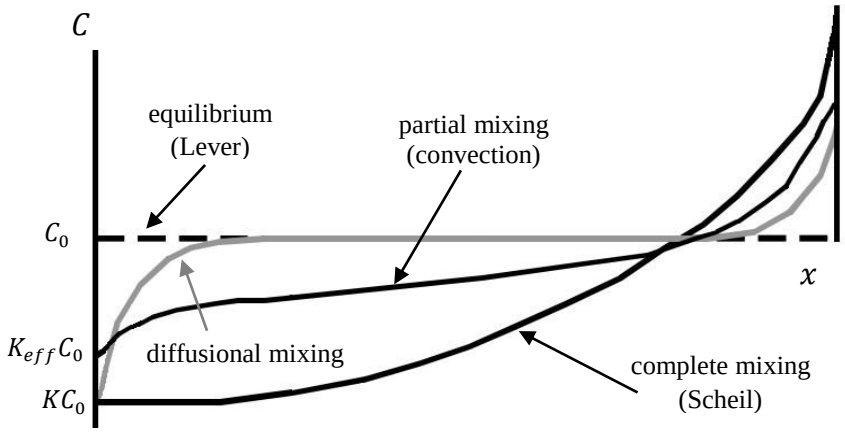

Figure 2.15. Solute distribution during solidification for different mechanisms.

(i) In pure materials, there is no constitutional undercooling. Therefore, instabilities result from the *thermal* field. In a positive thermal gradient in which the temperature increases continuously from the solid to the liquid, a local perturbation at the s/l interface will be located in a temperature higher than its melting temperature and it cannot grow. Accordingly, the interface remains stable and morphologically planar.

Sudden and high undercooling makes nuclei form in the bulk liquid away from the crucible wall and the s/l interface. Thus, due to isotropic growth conditions *equiaxed crystals* (spherical nuclei) grow in the bulk liquid. The latent heat of fusion at the grain surface cause a negative temperature gradient at which the s/l interface temperature is higher than the bulk liquid. Therefore, the equiaxed crystal surface will grow and form a dendritic interface which is *unstable*.

In alloy crystal growth, *constitutional (compositional)* undercooling (ΔT_c) is defined based on the difference between the solid and liquid solubility. The composition of the solid (KC_0) at the s/l interface at temperature T_S and the composition of the bulk liquid far away from the interface (C_0) are less than the composition of the liquid at the interface (C_0/K) as shown in Figure 2.12. According to Figure 2.16, the composition of the liquid (C_L) decreases from the interface toward the liquid. The composition profile given by C_L can be converted to temperature profile (T_L) ahead of the interface as seen in Figure 2.16. The line tangent to the temperature profile at the interface is the liquid (solutal) temperature gradient (G_L). If this gradient becomes greater than the externally generated thermal gradient in the liquid (G_T), the liquid will be at a lower temperature than its liquidus.

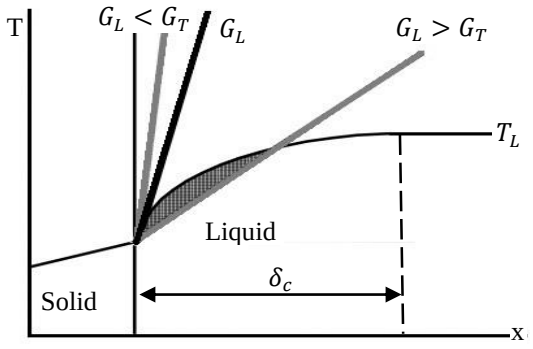

Figure 2.16. Comparison of thermal and compositional gradients.

This case is called constitutional undercooling, and can promote interface instability. When the applied thermal gradient in the liquid (G_T) at the s/l interface is greater than the solutal temperature gradient (G_L), the interface is compositionally stable and remains planar. By assuming the liquidus as a straight line, the liquidus slope (m_L) will be constant and the result is:

$$(G_L)_{int} = (dT_L/dx)_{int} = m_L(dC_L/dx)_{int} \tag{2.25}$$

The composition in the solute boundary layer is [117]:

$$C_L = C_0 + \Delta C_0\, exp\big(-V_g/D_L\big)C_0[1 + (1 - k/k)exp(-Vx/D_L)] \tag{2.26}$$

This formula with the boundary conditions in (2.25) results in the composition gradient at the s/l interface [119]:

$$(dC_L/dx)_{int} = -C_0(1 - K)V_g/KD_L \qquad \text{for steady state} \tag{2.27a}$$

$$(dC_L/dx)_{int} = -C_L(1 - K)V_g/D_L \qquad \text{for non-steady state} \tag{2.27b}$$

Then, the criterion for constitutional undercooling is defined as [120]:

$$\frac{G_T}{V_g} < -\frac{m_L C_0(1-K)}{KD_L} \qquad \text{for steady state} \tag{2.28a}$$

$$\frac{G_T}{V_g} < -\frac{m_L C_L(1-K)}{KD_L} \qquad \text{for non-steady state} \tag{2.28b}$$

At the steady state condition when the imposed temperature gradient from the furnace into the s/l interface is less than the equilibrium liquidus temperature gradient, there will be a supercooled region in front of the interface which changes a planar interface to a cellular one. Equations 2.26 and 2.27 imply that high temperature gradient (G_T) and low pulling velocity (V_p) lead to a planar and stable s/l interface.

2.2.5. Boundary Layers

Interaction of flows with interfaces can stimulate morphological instabilities. Near the s/l interface, the temperature, velocity, and solute concentration have boundary layer thicknesses of δ_T, δ_V, and δ_C, respectively. When the melt flow is unsteady, temperature and concentration fluctuations near the s/l interface result in the variation of boundary layer thicknesses and change in the growth rate and striations. Indeed, fluctuation in melt motion causes crystalline inhomogeneity. Davis and Schulze [121] have studied the effects of flow on morphological stability during directional solidification. According to this study δ_T, δ_V, and δ_C are related.

The temperature evolution from the bulk liquid (T_∞) to the solid interface (T_0) defines the thermal boundary layer thickness (δ_T) which relates the convection to the thermal diffusion by the thermal conductivity. The thermal boundary layer thickness (δ_T) is related to the ratio of the thermal diffusivity in the liquid (τ_L) to the pulling velocity (V_p).

$$\delta_T \propto \frac{\tau_L}{V_p} \tag{2.29}$$

Whether the segregation coefficient (K) is less than one (the interface rejects components) or greater than one (the interface accumulates components), the developing concentration gradient causes diffusive flow into the diffusion (concentration) boundary layer whose thickness (δ_C) is related to the ratio of the solute diffusivity (D_L) to the pulling velocity (V_p).

$$\delta_C \propto \frac{D_L}{V_p} \tag{2.30}$$

Coriell et al. [122] by imposing plane Couette flow upon the s/l interface defined the velocity boundary layer thickness (δ_V) from the *continuous* transition of the flow velocity parallel to the interface from stagnation (u_0) to the bulk liquid (u_∞). The velocity boundary layer thickness (δ_V), which is related to the ratio of the kinematic viscosity (ν) to the pulling velocity (V_p), is related to the other two boundary layer thicknesses [123]:

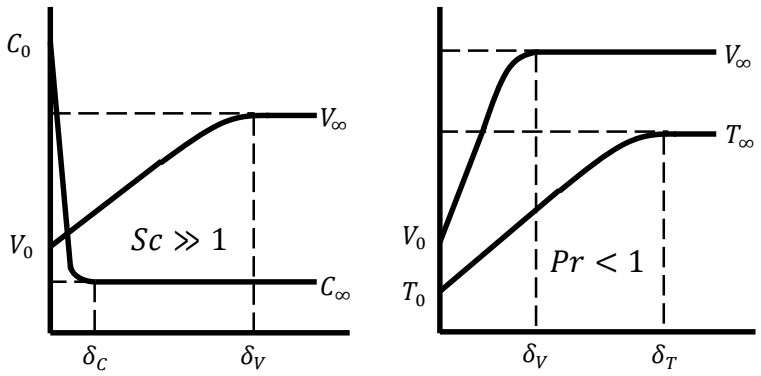

Figure 2.17. Schematic comparison between boundary layers in metallic melts.

$$\delta_V \propto \frac{\nu}{V_p} \tag{2.31}$$

$$\delta_C \approx \delta_V (D_L/\nu)^{0.33} = \delta_V \, Sc^{-0.33} \tag{2.32}$$

$$\delta_T \approx \delta_V (\tau_L/\nu)^{0.33} = \delta_V \, Pr^{-0.33} \tag{2.33}$$

where the Schmidt number (Sc) is the ratio of the kinematic viscosity (ν) to the solute diffusivity (D_L) and the Prandtl number (Pr) is defined as the ratio of the kinematic viscosity (ν) to the thermal diffusivity (τ_L). The boundary layer thicknesses vary amongst systems. For metal alloys, which have low viscosity and high thermal conductivity (like germanium alloys), the Prandtl number is small ($Pr < 1$). Accordingly, metallic melts have conductive heat transport rather than convective. These materials have wider thermal boundary layer than velocity boundary layer ($\delta_T \gg \delta_V$). In addition, in metallic melts convection does not affect the temperature gradient near the s/l interface. Multicomponent melts have a large Schmidt number [123] ($Sc \gg 1$), i.e. the velocity boundary layer is much broader than the solute boundary layer ($\delta_V \gg \delta_C$). Figure 2.17 briefly demonstrates the boundary layers in metallic melts.

2.2.6. Convection in the Melt

According to the previous sections, melt convection is significantly important in semiconductor crystal growth processes to obtain the desired dopant segregation and s/l interface shape. The melt flow affects the crystal growth conditions. It can lead to

inhomogeneous radial/axial dopant distribution and undesired temperature oscillations near the s/l interface which cause defects. It can also improve the crystal quality if it is present in a controlled way. In crystal growth from the melt, the rate of diffusion is typically slower than the convective mass transport velocity. Consequently, the convection in the melt has an important role in the growth and segregation. Crystallization will be mostly controlled by mass transport in forms of Marangoni convection, buoyancy-driven (natural) convection, or artificially evoked forced convection.

2.2.6.1. Natural Convection. Temperature variations in a melt volume under gravitational acceleration result in natural convection in the system by augmenting heat and mass transfer. The thermal Rayleigh number (Ra_T) determines the strength of this convective motion.

$$Ra_T = \frac{g\beta_T \Delta T {L_c}^3}{\nu k} = \frac{convective\ heat\ transfer}{diffusive\ heat\ transfer} = \frac{buoyancy\ force}{viscous\ force} \qquad (2.34)$$

where g is gravitational acceleration, L_c is the characteristic length, β_T is thermal expansion coefficient, and ΔT is the temperature difference. It should be noted that two systems with the same thermal Rayleigh number can have different convection patterns. Actually, heat and mass transfer depends on temperature distribution and system configuration. The natural convective flow depending on the growth conditions can be categorized as *Buoyancy-driven* convection or *Thermo-solutal-capillary (Marangoni)* convection. The buoyancy-driven convection results from radial/axial temperature gradient caused by the interface deformation or heat flux and density difference in binary liquids. It can be suppressed in the microgravity. For the buoyancy-driven convection, the orientation of the body force with respect to the thermal gradients characterizes the growth configurations. The Marangoni convection is driven by surface tension which depends on both temperature and compositional gradient at the free surface.

In the Czochralski method, the heated crucible wall results in radial Buoyancy-driven convection which joins the Marangoni flow at the melt free surface. Moreover, the rotating crystal takes the melt up at the center of the s/l interface. These three flows together make a complicated flow structure [124]. The crucible rotation makes this flow more complicated [125]. In the VB method, the radial heat flux from the furnace and the s/l interface

deformation result in a small buoyancy-driven convection in comparison to the CZ method. In the horizontal configuration of Bridgman and FZ methods, the buoyancy-driven convection as well as Marangoni convection, due to perpendicularity of gravitational force and the applied temperature gradient from the furnace, is much stronger than that in the vertical configuration [126]. Thus, the dopant can be well mixed. The s/l interface shape is intensely affected, though. In the VB configuration, the convection flow is typically stable and weak, and it does not have a strong effect on the interface shape compared to the heat transfer. In addition, the dopant diffusivity is insignificant and is affected by the convective flow. Therefore, the melt convection should be carefully controlled to achieve a desired dopant distribution in this method.

2.2.6.2. Forced Convection. Forced convective flow in the melt to control the crystal growth conditions can be obtained from external fields such as static magnetic fields [127,128], dynamic magnetic fields [129,130], electromagnetic fields [131,132], rotation [133,134], centrifugation [135-137], reduced gravity [138,139], and vibrational effects [140-143]. Static magnetic fields apply Lorentz force to electrical conductive materials and have a damping effect on melt flow to suppress temperature fluctuations and reduce growth velocity oscillations. Dynamic magnetic fields mix the melt more effectively and consume less power in comparison to static fields. Electromagnetic fields stir the melt azimuthally in a fixed crucible by an electromagnetic force to control the convective motion. Mechanical vibration stimulates convection in the melt grown methods. In these systems, the material should not necessarily couple to the electrical conductivity (unlike magnetic field applications) and can be selected more easily. The only limitation is that the vibrating device should be connected to the crystal or melt, and the vibrational parameters (amplitude and frequency) should be selected properly. Mixing the melt during crystallization can be critical in homogenizing the solute distribution in the solid and liquid, and decreasing the diffusional boundary layer thickness to avoid constitutional supercooling, morphological instability, and other undesirable defects.

There are several types of mechanical vibration. Gershuni and Lubimov [144] differentiated them as translational, rotational, swinging, submerged body vibrations, harmonic and nonharmonic, and low-frequency and high-frequency vibration. Crystal growth methods utilizing different types of vibration generate a variety of forced convective

flows. In this study only translational vertical vibration, which has been used in the axial vibrational control (AVC) method (introduced in section 2.2.2.3), is considered. This type of vibrational motion, which was used by Evgeny Zharikov [17] with low frequency (tens of Hz) and small amplitude (tens to hundreds of microns), forms a vortex near the sharp edges of vibrating device perpendicular to the direction of vibration. Periodic movement of the vibrating device results in a stationary flow. The applied vibrations are assumed to have a small amplitude and a harmonic sinusoidal velocity as:

$$V_{vib} = Af\sin(\omega t) \tag{2.35}$$

where f is the vibration frequency and A is the vibration amplitude.

2.3. Numerical Simulation of Crystal Growth from the Melt

Bulk crystal growth including a diverse range of physical phenomena is amongst the most complicated processes to numerically model. In melt growth systems, a continuum model can determine the interface shape, flow pattern, chemical composition, and temperature distribution. In order to reasonably model these phenomena, understanding the fundamentals as well as numerical methods is required. Consequently, many studies cover transport phenomena, heat transfer, and convective flow in crystal growth modelling.

Brown [145] has reviewed the analytical models of transport process in single crystal growth from the melt until the 1980s. Later, many authors, such as Müller and Ostrogorsky [146], Derby [147,148], Polezhaev [149], Kakimoto [150], and others discussed this issue in more details. Lately, Lan [151] has provided an update on recent crystal growth modellings.

Since this study is about crystal growth with VB, AHP, and AVC methods and in these configurations the melt free surface is far from the s/l interface (in contrast to the Czochralski method), the Marangoni convection has insignificant effects on growth parameters. Therefore, this effect is ignored and only buoyancy-driven convection and conductive heat transfer are considered for modelling. In addition, in these methods, the centrifugal, angular, rotational, and magnetic fields are not used.

Radiative heat transfer has a very important role in melt growth systems due to high temperatures [152]. It involves heat fluxes from surfaces (surface radiation) and through the medium itself (internal radiation). Since the melt free surface in the methods practiced in this study is far away from the s/l interface and molten germanium is an opaque material and its emissivity at melting temperature is 0.17 [153], the radiation effect is not considered for simplicity.

2.3.1. Governing Equations

The heat transfer, mass flow, and composition distribution in crystal growth from the melt are governed by the conservation of mass, momentum, and energy. Here, the commonly used form of the governing equations for modelling crystal growth are summarized. Behind these equations, the fluid is assumed to be incompressible (Newtonian flow), and energy and species transport is dominated by convection effects, rather than diffusion-induced flow. For easy interpretation, dimensionless forms of these governing equations are also provided. In this form, the mass conservation continuity equation is [154]:

$$\nabla.\vec{V} = 0 \tag{2.36}$$

The momentum conservation equation is based on the Boussinesq approximation, in which the density is assumed to be constant everywhere except in the body force term, and Newtonian flow, in which the density is independent of pressure and temperature in the dimensional and dimensionless forms. This gives [136,154]:

$$\partial\vec{V}/\partial t + \left(\vec{V}.\nabla\right)\vec{V} - (\mu/\rho_0)\nabla^2\vec{V} = -\nabla\vec{w} + \vec{g} \qquad \text{dimensional} \tag{2.37a}$$

$$\partial\vec{V}/\partial t + \vec{V}.\nabla\vec{V} = -\nabla P + Pr\nabla^2\vec{V} + \vec{F} \qquad \text{dimensionless} \tag{2.37b}$$

respectively. The Boussinesq approximation is necessary in order to include the effect of density variations arising from the temperature and concentration gradients across the liquid phase. The density variations as a function of temperature and concentration can be shown

by expanding the density into a Taylor series about the reference concentration C_{ref} and temperature T_{ref} [129,147]:

$$\rho = \rho_0[1 - \beta_T(T - T_{ref}) + \beta_S(C - C_{ref})] \tag{2.38}$$

The dimensionless body force per unit volume in Equation 2.36 is given as [154]:

$$\vec{F} = -\mathrm{Pr}[Ra_T(T - T_{ref}) + Ra_S(C - C_{ref})]\vec{e}_g \tag{2.39}$$

The dimensional and dimensionless forms of the conservation equation of energy and composition are presented as [148,154]:

$$\rho_0 C_p(\partial T/\partial t + \vec{V}.\nabla T) = \nabla.(k\,\nabla T) \quad \text{dimensional} \tag{2.40a}$$

$$\partial T/\partial t + \vec{V}.\nabla T = \nabla^2 T + S \quad \text{dimensionless} \tag{2.40b}$$

$$\partial C/\partial t + \vec{V}.\nabla \mathrm{C} = \nabla.(D\,\nabla C) \quad \text{dimensional} \tag{2.41a}$$

$$\partial C/\partial t + \vec{V}.\nabla \mathrm{C} = (Pr/Sc)\nabla^2 C \quad \text{dimensionless} \tag{2.41b}$$

respectively. In these equations, w is the specific thermodynamic work, g is the gravitational force, V is the flow velocity, t is the time, P is pressure, T is temperature, k is thermal conductivity, C is concentration, D is diffusion coefficient, T_{ref} is the dimensionless reference temperature, C_{ref} is the dimensionless dopant concentration, S is the source term, and e_g is the unit vector in the gravitational field. The thermal Rayleigh number (Ra_T) is mentioned in Equation 2.32. The solutal Rayleigh number (Ra_C) is similar to the thermal one but the driving force is based on $\beta_S \Delta C$, where β_S is the solutal expansion coefficient, and ΔC is the concentration difference. As mentioned in section 2.2.5, the Prandtl number (Pr) is the ratio of the kinematic viscosity to the thermal diffusivity and the Schmidt number (Sc) is the ratio of the kinematic viscosity to the solute diffusivity. Since in semiconductors and metals the Prandtl number is less than one, 0.0075 [155] for germanium, the flow does

not affect the heat transfer and the interface shape too much and conductive heat transfer dominates convective heat transfer. Instead, because of large ratio of the kinematic viscosity to the solute diffusivity in these materials ($Sc \gg 1$), 7.6743 [155] for germanium, the dopant segregation is mostly affected by convective flow rather than atomic diffusion. Therefore, conductive and convective heat transfer both have an important role in semiconductors crystal growth.

In case of existence of the centrifugal, angular, rotational, and magnetic fields, in addition to the gravitational field, the related terms should be added to the dimensionless body force (F) in the momentum conservation equation (Equation 2.36) [151]. Since these fields are not used in this study, the related terms are not mentioned here. Moreover, if the material is not transparent and has a low emissivity (like germanium), the source term S in Equation 2.40 can be ignored for simplicity.

2.3.2. Boundary Conditions

To solve the governing equations numerically for a specific growth system, boundary conditions should be defined appropriately. The energy and solute equilibrium at the interface are very important to consider. For the VB configuration in which the crucible moves down with a speed of V_p, the energy and dopant balances at the s/l interface, by ignoring internal radiation and solid state diffusion, are [135,151]:

$$Q_s - Q_l + \gamma St\left[\left(V_p - dh_c/dt\right)(\vec{n}.\vec{e}_z)\right] = 0 \tag{2.42}$$

$$\vec{n}.\nabla C_l + \frac{Sc}{Pr}(1-K)C\left[\left(V_p - dh_c/dt\right)(\vec{n}.\vec{e}_z)\right] = 0 \tag{2.43}$$

respectively, where Q_s is the thermal heat flux in the solid, Q_l is the thermal heat flux in the liquid, γ is the density ratio of the solid and the liquid, St is the Stefan number or the ratio of sensible heat to latent heat, h_c is the dimensionless interface position, $\vec{e}_z$ is the unit vector in axial direction, and K is the dopant segregation coefficient. The no-slip boundary condition is considered at the walls where the liquid is in contact with the crucible. The walls

are also impermeable to the solute in the liquid. Therefore, in a two dimensional cylinderical system, boundary conditions at the wall are [155]:

$$V_r = 0, \qquad V_z = 0, \qquad \partial C/\partial r = 0 \tag{2.44}$$

At the centerline the symmetry boundary condition is applied. Thus,

$$V_r = 0, \qquad \partial C/\partial r = 0, \qquad \partial T/\partial r = 0, \qquad \partial V_z/\partial r = 0 \tag{2.45}$$

More details about specific boundary conditions applied to the simulated system in this research will be provided at section 3.3, and since pure germanium is the only material in all simulations, the solute equilibrium equations and boundary conditions are not discussed.

2.3.3. Available Methods/Approaches in Phase Change Problems

There are several numerical methods with different merits and disadvantages to discretize and solve the governing equations of phase change problems. These problems deal with time-dependent boundaries where the position of the boundary needs be determined as a function of time and space. Accordingly, they are known as moving boundary problems or Stefan problems.

Many numerical methods are proposed for solving the moving boundary problems; for instance, fixed grid methods, variable grid methods, methods of latent-heat evolution, apparent heat capacity methods, effective capacity method, heat integration method, source based method, and enthalpy method are comprehensively explained by Henry Hu and Stavros Argyropoulos [156]. In fixed grid method, the heat flow equation is approximated by finite difference substitutes for the derivatives to calculate temperature and time on a fixed grid. The major problem with this method is the zero velocity condition at phase change area. Since the fixed grid methods sometimes fail as the boundary excels a space increment in a time step, variable grid methods where the exact location of the moving boundary is evaluated on a grid at each step will be more useful. Methods of latent-heat evolution focus on applying finite difference methods to the formulation of the process, locating moving

boundaries, and finding temperature outlines at each time step. They are applicable to the problems involving one or two phases in one space dimension. In effective capacity method, rather than determining an apparent capacity in terms of the temperature of nodes, an effective capacity is calculated based on the integration over the control volume. In the heat integration method, the temperatures of all control volumes are monitored. The source based method allows any additional heat from either a heat sink or a heat source to be introduced into the general form of the energy equation as an extra term (the source term). In the enthalpy method, the latent heat evolves by the enthalpy in addition to the relationship between the enthalpy and temperature. In the enthalpy formulation, there is no explicit conditions on the heat flow at the s/l interface which simplifies the numerical modelling requirements.

2.3.4. The Enthalpy-Porosity Method

The enthalpy method is a numerical formulation for solving moving boundary problems under conduction and convection. This method employs a temperature formulation for problems with deforming grids treating the moving s/l interface, and uses an enthalpy formulation for a fixed grid in which the s/l interface is not tracked explicitly. There are some examples of fixed grid solutions of convection-diffusion phase change in the literature [157-160]. The main problem with fixed grids is the zero velocity when the liquid turns to solid. Voller *et al.* [158,159] suggested the *enthalpy-porosity method* dealing with this problem in fixed grids. In this method, the grids are modelled as pseudo porous media with a quantity defined as liquid fraction increasing from 0 to 1 as the enthalpy (ΔH) increases from zero to the latent heat of the phase change (L). The porosity decreases to zero for the solid region and therefore the velocity of the cell drops to zero. The cells with a liquid fraction between 0 and 1 form a region known as the *mushy zone* in which the latent heat of fusion is a function of temperature, $\Delta H = f(T)$.

2.3.5. ANSYS Fluent Simulation

Several codes and software packages have been developed to model phase change problems due to their importance in industry and technology. CGSim [161], CrysVUn [162],

CrysMAS [163], STHAMAS [164], ORCAN [165], and FEMAG [166] are some specialized codes developed by companies for crystal growth simulations. ANSYS Fluent (a computational fluid dynamics software developed by ANSYS Inc. in Pennsylvania, United States) is an alternative with its strong solvers for simulating solidification/melting processes in crystal growth. It can simulate phase change problems for pure materials as well as alloys with complicated geometries and is capable of including radiation. This software has been successfully used to simulate different melt grown crystal methods such as Czochralski [167-169], floating-zone [170], RVT [171], Bridgman [172], and AVC-VGF [173], AVC-CZ [104]. ANSYS Fluent uses the well-known enthalpy-porosity method for modeling such problems. All of the mentioned codes and packages use the finite volume method (FVM) for representing and evaluating partial differential equations at discrete places on a meshed geometry.

In the following subsections, a general approach for solving the fluid dynamics problems is provided. This approach is used by most of the aforementioned software packages including ANSYS Fluent. All of the provided information is obtained from the theory guide of the ANSYS Fluent software [174]. The simulation of the current study is specifically explained in section 3.3.3.

2.3.5.1. Navier-Stokes (NS) Equations. In order to obtain the temperature profile and the velocity field in a fluid flow problem, the Navier-Stokes equations have to be solved. The Navier-Stokes equations include the conservation equations of mass, momentum, and energy. These equations should be solved to find the pressure, density, velocity, and temperature. Thus, there is one unknown more than equations.

2.3.5.2. ANSYS Fluent Solvers. There are two solvers in ANSYS Fluent to solve the required equations; the density-based solver and the pressure-based solver. The density-based solver solves the governing equations simultaneously and coupled together, whereas the pressure-based solver uses an algorithm based on the projection method [175]. In this method, the continuity of the velocity field is attained by solving an equation for the pressure correction. This equation results from the continuity and the momentum equations in such a way that continuity is satisfied by the velocity field and corrected by the pressure. The governing equations are nonlinear and coupled. Therefore, the solution implies an iterative

procedure in which all of governing equations are solved together repetitively until the solution converges to the set residuals.

2.3.5.3. Solution Methods. The continuity equation should be reformatted by an additional condition for pressure via pressure-velocity coupling. The pressure-based solver solves the problem using a segregated or coupled algorithm. In ANSYS Fluent, there are four pressure-velocity coupling algorithms: SIMPLE (Semi-Implicit Method for Pressure Linked Equations), SIMPLEC (SIMPLE-Consistent), PISO (Pressure-Implicit with Splitting of Operators), and Coupled. All of these algorithms use the prediction-correction approach, except the "coupled" algorithm. These schemes are referred to as the pressure-based segregated algorithm. Steady-state calculations normally use the segregated algorithms (SIMPLE, SIMPLEC, and PISO). PISO is also useful for transient scheming on highly skewed meshes. The Coupled algorithm supports complete pressure-velocity coupling.

2.3.5.4. Spatial Discretization Schemes. Gradients are used to construct values of a scalar at the cells and to compute velocity derivatives. There are three available gradients in ANSYS Fluent; Green-Gauss cell based, Green-Gauss node based, and least-squares cell based. The correctness of the least-squares gradient method on skewed and distorted meshes is similar to that of the other two gradients. However, calculating the least-squares gradient is computationally less expensive than the other two.

Among the available pressure interpolation schemes in ANSYS Fluent, when the pressure-based solver is employed, mostly the second-order scheme is a suitable choice. However, the body-force-weighted scheme is suggested for the problems including significant body forces.

The scheme for the convection terms of the flow equations of single-phase problems is the second-order upwind discretization, while, the first-order upwind discretization is used by default for multiphase flows. Although, the first-order upwind discretization enhances the numerical diffusion/error, it is still acceptable when the flow is allied with the mesh, as for a laminar flow in a geometry with a quadrilateral/hexahedral mesh. For triangular/tetrahedral meshes, the flow does not align with the mesh. Thus, generally the second-order discretization provides more accurate results for this kind of mesh. Obviously, the second-

order discretization also gives better results for quad/hex meshes, particularly for complex flows. Briefly, while the first-order scheme produces better convergence than the second-order discretization, it usually yields less precise results.

3. MATERIALS AND METHODS

High quality single crystal production requires accurate monitoring and control of growth parameters to obtain interface morphological stability via homogeneous solute distribution. This study has utilized the VB, AHP, and AVC methods to experimentally grow antimony-doped germanium (Ge-Sb) semiconductor single crystals. The resultant buoyancy driven convection and concave s/l interface in the VB method can benefit from the submerged baffle in the bulk liquid in the AHP method and the vibrational motion of the baffle in the AVC method. In fact, the materials used for manufacturing the growth unit and the growth parameters are carefully determined. In addition, simulations helped to better investigate the flow pattern in the melt in all methods to choose the dimensional parameters more efficiently.

This chapter introduces the VB/AHP/AVC experimental equipment and describes the experimental procedures, characterization of the grown crystals, and the numerical simulations.

3.1. The VB/AHP/AVC Unit

In the present study, a specific unit designed by Dr. Ercan Balikci and constructed by Thermo (a liquidated company located in Moscow, Russia) is used. The control system is designed by Dr. Ercan Balikci and implemented by a former M.Sc. student, Mr. Aidin Dario for the VB and AHP methods and developed by current M.Sc. student, Mr. Pouya Yousefi and Ph.D. student, Mr. Aidin Sheikhi for the AVC method.

The experimental unit is illustrated in Figure 3.1. It is comprised of four main parts; growth cell, translation mechanism, control system, and vacuum enclosure.

3.1.1. Growth Chamber

The growth chamber contains a four-zone tubular furnace with 80 millimeter diameter and around 450 millimeters total height. The furnace is made by winding molybdenum wires covered by high purity alumina ceramic. Compact rounded wires make each cylindrical heating zone of the furnace. The furnace is placed inside a cylindrical steel chamber. Between the furnace and the steel chamber, first there are two molybdenum sheets and then a thick three-layer cylindrical insulator of graphite felts to protect the steel chamber from radiation and minimize the heat loss of the furnace (Figure 3.1b). Since the top heaters are hotter than the bottom heaters (to provide a positive temperature gradient), the thickness of the graphite felt insulator is more at the top. Inside the furnace, a crucible-pedestal assembly made of a high density graphite [176] is positioned. The inner diameter of the crucible is 40 mm and its length is 180 mm. The pedestal at the bottom and a graphite cap at the top are mounted to the crucible. In the AHP and AVC methods, a baffle shaft goes through a hole at the center of the cap to be positioned inside the crucible. The hole makes the baffle centered in the crucible. The baffle of 39 mm diameter and 20 mm height has six small tabs at the bottom touching the inner wall of the crucible to keep a constant 0.5 mm annular gap between the crucible and the baffle. The external wall of the crucible has some annular and vertical grooves for thermocouple placement.

3.1.2. Vacuum Enclosure

The vacuum enclosure contains the aforementioned steel cylindrical chamber and two plates at the top and bottom of the chamber. They are manufactured of double-walled stainless steel and cooled by circulating water between the walls. The water is cooled and circulated via a Julabo made chiller. The bottom plate is attached onto a stainless steel platform. Silicon O-rings are used to enclose the gaps between the chamber and the two plates. Then, the chamber is assembled to the plates with bolts and nuts. The bottom plate has four inlet/outlet ports. These ports are used for the pressure gauge, furnace thermocouple wires, incoming inert gas, and evacuation. At the beginning of each experiment while the furnace is heating up, the enclosure is pumped down to 10^{-3} *mbar* via an Ilmvac mechanical vacuum pump to prevent oxidization. After vacuuming the enclosure, it is fed of 99.999% purity argon gas.

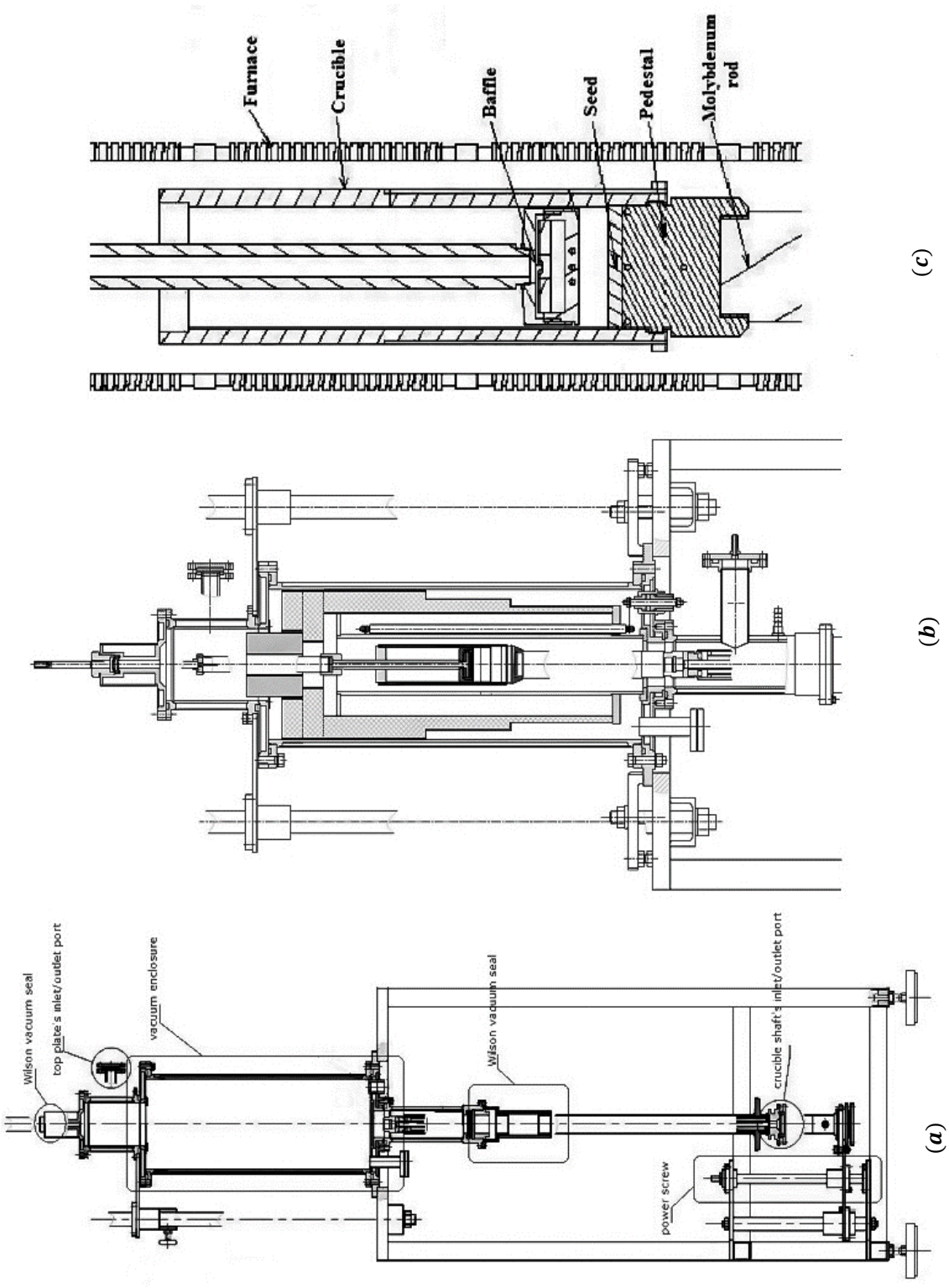

Figure 3.1. the VB/AHP/AVC growth unit (a), vacuum enclosure and growth chamber (b), baffle-crucible-pedestal assembly (c). Labels are described in the text [177].

During the experiments, the enclosure is continuously purged with fresh argon gas and the used gas escapes at a constant rate through a pneumatic hose from the valve of the gas outlet flange on top of the vacuum enclosure into a beaker filled with water to let the operator see the outgoing gas. The flange of the vacuum port is connected to a vacuum ball valve and the flange of the inert gas is connected to pneumatic ball valve. The flanges are also sealed with O-rings. The crucible shaft passes through a hole at the middle of the bottom plate, and a brass rod connected to the baffle shaft passes through a hole at the middle of the top plate. These shafts move through Wilson seals without disturbing the vacuum or inert gas environment inside the vacuum enclosure (Figure 3.1a).

3.1.3. Translation Mechanism

In order to move the crucible upward and downward, a translation mechanism is positioned underneath the platform. This mechanism transfers the crucible shaft from the bottom of the system through the enclosure. The crucible shaft is a stainless steel double-walled water-cooled shaft which is connected to the pedestal via a molybdenum rod. The molybdenum rod cools the pedestal in order to facilitate an axial heat escape from the bottom of the crystal. The bottom of the shaft is enclosed with a flange. The crucible thermocouple wires go inside the system from the bottom flange which is sealed with silicon O-ring. A power screw converts the rotational motion provided by a KEB servo motor and servo drive to vertical movement in order to move the crucible shaft vertically. To minimize the transmission of the motor's vibration to the crucible shaft, a gearbox coupled with a rubber connector to the power screw is used to reduce the frequency of rotation of the motor.

3.1.4. Control System

The growth system has been controlled with an in-house program written in LabVIEW (provided by National Instruments Corporation, Texas, USA) used for data acquisition. Setting up the thermocouples temperature, heating up the heaters in the furnace, and translation and speed of the servomotor are controlled by this system. Of the thermocouples used in the system, two K-type sheated thermocouples are purchased and the rest were C-type thermocouples made by hand. For the C-type thermocouples Tungsten-5%Rhenium and Tungsten-26%Rhenium wires, both with 0.5 mm diameter, are used. The tips of the wires

are welded to each other by a TIG welder to make the thermocouples. Each wire was thermally and electrically insulated with proper insulators. Double hole ceramic sleeves made by OMEGA (a company supplying highly engineered products) are used to cover the thermocouple wires inside the furnace, and the remainder outside the furnace is covered with OMEGA-made fiber glass insulators. These C-type thermocouples are collected in two screw terminal boxes, as cold junction points, outside of the system. These boxes and the data acquisition system are connected to the system via copper wires. The two purchased K-type thermocouples measured the cold junction temperature in these boxes to be used in the software for cold junction compensation.

A Keithley 7700 differential multiplexer module collect the data coming from the thermocouples. This module is plugged into a Kiethley 2700 data acquisition and switching system. An IEEE-488 (GPIB) interface read the data coming from the data acquisition system. The visual program developed in the LabVIEW interface monitors all these data to ease the control process. The user interface in this platform has three pages; the setup page, the monitoring page, and the error page. The *setup page* is used to set the temperature for each thermocouple, the conforming PID (proportional integral derivative) values of each furnace zone, and the velocity and the displacement of the servomotor. Software can control the furnace heaters in three modes; manual heating, PID heating, and cooling. According to the desired set temperatures the software calculates the required output voltage to heat up the heaters and keep them at that temperature. The PID control can keep the heaters at their temperature set values with 0.3℃ offset. Software sends a voltage ranged from 0 to 10 Volts using a Kiethley PCI3130 analog output card to four Eurotherm single phase power thyristor SCR (Silicon-Controlled Rectifier) units. These thyristors send a current to the heating furnace zones up to 60A, proportional to the incoming control voltage. The software also sends a constant voltage to the motor inverter to keep the translation motor rotating at a constant rate. The *monitoring page* display the furnace temperatures versus time on a graphical screen. It also contains a table showing the cold junction temperatures, the thermocouple temperatures, heaters set temperatures, relative position of the crucible shaft, and time. These data are recorded in an excel workbook file. The *error page* shows any problems that the software encounters.

3.2. Experimental Procedures

All crystals are grown in a $40mm$ inner diameter cylindrical graphite crucible. Initially, a cylindrical germanium seed with (111) orientation and $10\ mm$ height is placed at the base of the crucible. The seed, which is an optical grade high purity single crystal germanium ingot of 40mm diameter, is purchased from Novotech Inc., Boston, USA. The determined single crystal seed is cut from the ingot by an ATM GmbH (Mammelzen, Germany) precision slicing device and both sides of it are ground with silicon-carbide grinding papers. Since the melting temperature of the antimony (630°C) is much lower than that of the germanium (938.3 °C), a master charge of a Ge-Sb alloy is prepared in vacuum and placed between the seed and germanium chunks to avoid vaporization of antimony during melting of the germanium chunks. The master charge was placed on top of the seed and below the Ge chunks. The germanium chunks are also evaporation grade high purity polycrystalline. The amount of antimony in each grown crystal is $10^{20}\ atom/cc$ ($0.24\ at\%$).

3.2.1. The Vertical Bridgman (VB) Method

In the VB method, since there is no baffle used inside the crucible, after putting the master charge and the Ge chunks on the seed, the crucible is closed with a graphite cap and then the top cap of the chamber is mounted up on the system. The crucible is surrounded by the furnace with four heaters, each adjusted individually to establish a $20\ °C/cm$ positive axial temperature gradient (G_F) along the crucible. The bolts for fixing the bottom plate, the chamber, and the top cap are placed into their holes in order to align these three parts, but are not tightened. The vacuuming process is started before tightening bolts of the chamber to let the silicon O-rings be squeezed (about 3 mm) during this process. All the valves and flanges are closed except the vacuum valve. Then the vacuum pump is turned on. When the vacuum gauge reached 10^{-3} mbar, the bolts and nuts of the chamber are tightened. At this time, the heaters were turned on to reach their set points in the software. The heaters are heated up in manual mode until about 500℃ under vacuum to remove degassing impurities, and then the argon gas of 99.999 % purity is purged into the system. By closing the vacuum valve and opening the argon gas valve, the chamber is filled with argon gas with a maximum

pressure of 0.5 atm. The system is vacuumed and filled with argon twice more to purge the system of impure gases. Subsequently, the heaters are heated up to their set temperatures with the PID control. The argon gas pressure inside the chamber is kept almost 1 atm above the ambient pressure during the experiment.

The crucible is positioned inside the furnace to melt all of the Ge chunks, Sb-Ge charge, and half of the seed. The temperature profile inside the growth chamber is measured beforehand in some sample tests and the position of the initial s/l interface is estimated. When the furnace thermocouples reached the set temperatures, the crucible is remained at that position for 20 minutes to let the melting process become stable and the solute distribute throughout the melt. Then, the motor starts to rotate and the solidification process begins. The solidification process is continued by pulling the crucible down with a constant velocity. After the solidification is completed and the motor is stopped, the control system is switched to PID cooling while continuing to feed argon gas to the system until the heater temperatures fell below 250℃ to protect components from oxidation.

The described procedure so far is common to the initial setup preparation of all the VB, AHP, and AVC methods. The following subsections are about the specific procedures of each method.

3.2.2. The Axial Heat Processing (AHP) Method

The difference between the VB and AHP method is the baffle used in the AHP method inside the crucible to adjust the effective melt height. The baffle in the AHP method has a wide cylindrical lower part facing the bottom of the crucible with 39 mm diameter and 20 mm height. This part is attached to a 15 mm long rod from the top passing through a hole in the middle of the graphite enclosure cap of the crucible. This rod is connected to a brass rod in the center line of the top cap of the vacuum enclosure going through a Wilson vacuum seal out of the system. At the beginning of each experiment due to existence of germanium chunks, the baffle should be placed at its maximum position inside the crucible.

In all AHP experiments, after closing the system, the vacuum and gas purging processes are carried out the same as for the VB method. After heating the heaters up, the crucible is

gradually moved upward to the calculated initial position where the s/l interface would form. Next, the baffle is immersed to the melt until it touched the top of the seed. Then, it is pulled up to make the desired initial melt height above the s/l interface. Similar to the VB method, at this situation the crucible is kept steady to have a stabilized system before moving it down. The same procedure is performed for the solidification process as in the VB method.

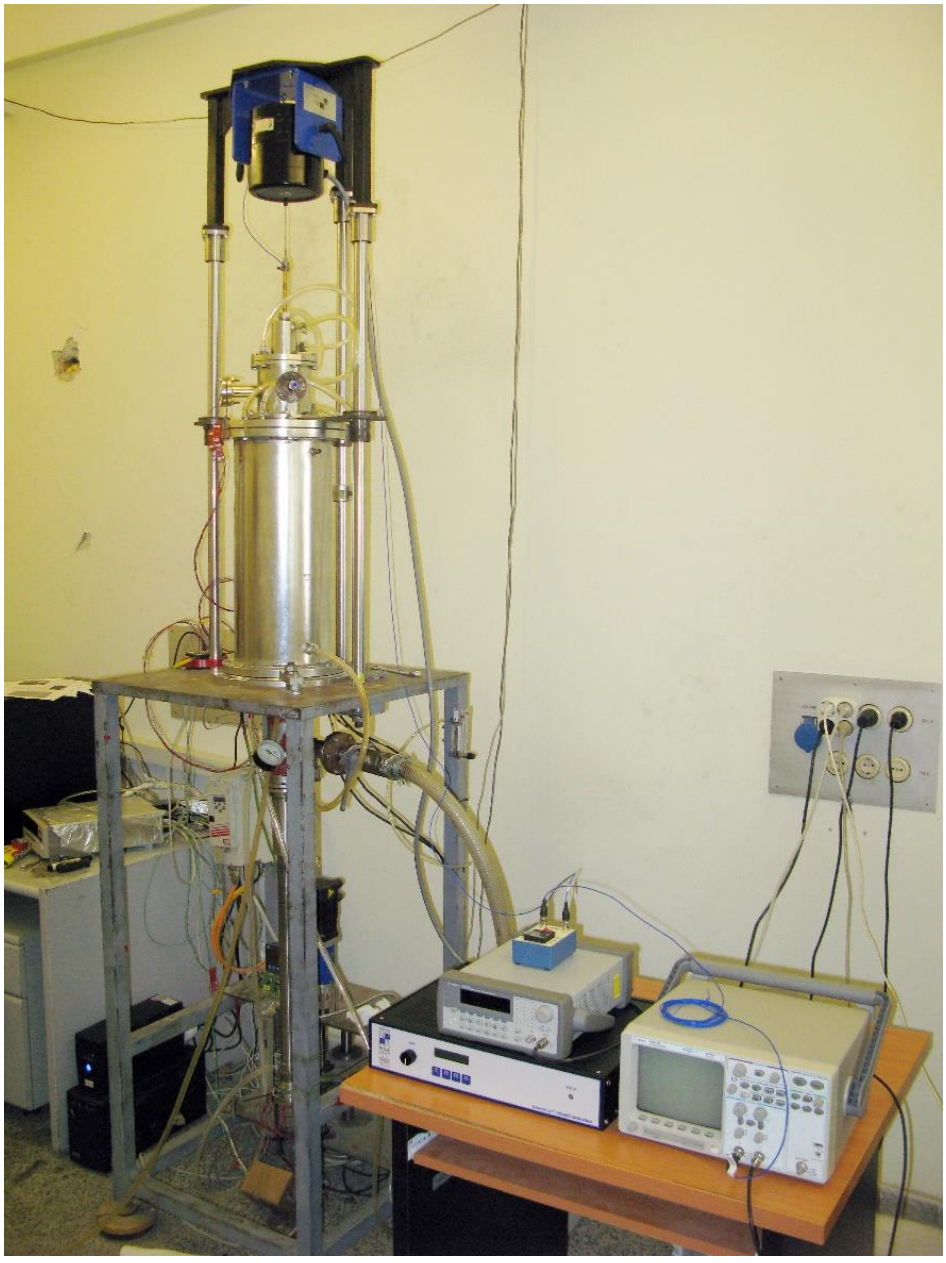

Figure 3.2. The VB/AHP/AVC unit at BUSCGLAB.

3.2.3. The Axial Vibrational Control (AVC) Method

Preparing the setup for the AVC experiments is very similar to the AHP experiments. The only difference is the vibrating baffle. In fact, a MODAL SHOP shaker model 2060E is assembled on top of the growth unit connected to the brass rod to shake the baffle inside the melt. This shaker gets its power from a SmartAmp power amplifier. The desired amplitude and frequency of the vibration are generated by an Agilent model 33220A signal generator is minitored by an Agilent oscilloscope model 54621A during crystal growth. In this method, the baffle vibrates with a sinusoidal pattern. The vibration amplitude is measured by a laser doppler velocimeter. Figure 3.2 shows the VB/AHP/AVC growth unit in Solidification and Crystal Growth Laboratory at Bogazici University (BUSCGLAB).

3.2.4. Characterization of the Grown Crystals

After growth, each crystal is analyzed to obtain its characterizations including and axial and radial dopant distribution, single crystal length, and the interface shape during growth through striation lines.

3.2.4.1. Metallography. To do this, each crystal is axially cut into two halves using a diamond blade cutter. The surface of one of the halves is prepared for characterization by the standard metallography processes, which are grinding, polishing, and etching. For grinding the surface Beuhler SiC grinding papers (from P-120 grit to P-2000 grit) are used. Then the ground surface is polished on Beuhler polishing cloths and a suspension of Beuhler alumina powders. All samples are polished with 5μm powder and continued with 1 and 0.3μm powders. After each step, the surface is washed with water to prevent scratches on the finer polishing step. The grinding and polishing time is approximately 2 hours for each surface.

3.2.4.2. Dopant Distribution Measurement. The final polished surface of the longitudinal half of each crystal is used to measure its electrical resistivity employing the four-point probe technique. The resistivity is measured on different points on the surface. The first row of the selected points is 5 mm above the seed base and the other points are selected above the first row with 4 mm intervals. In the radial direction, the points are selected with 4 mm intervals from the center line up to 16 mm to the right and left sides.

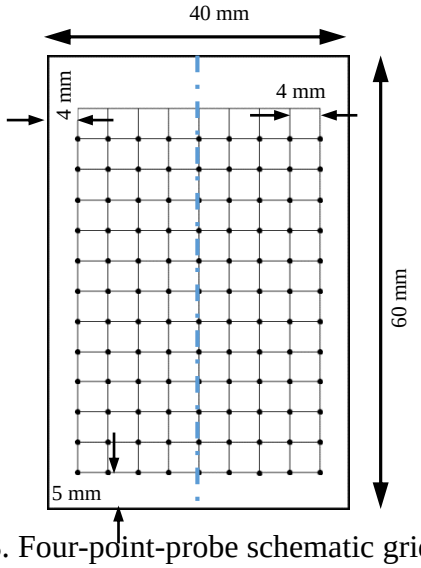

Figure 3.3. Four-point-probe schematic grid points.

The probe tip is kept 4 mm away from the sides to prevent edge effect. Figure 3.3 is a schematic illustration of these grid points. Measurements are taken by lowering the head of a JANDEL micro-position probe (provided by Jandel Engineering Ltd., UK) onto each grid point on the surface and applying 30 mA. For measuring the resistivity, the forward and reverse polarity voltages are taken from a JANDEL RM3 nanovoltmeter. These measurements are converted to resistivity via the following relationship [178,179]:

$$Rs = 2\pi s V_r / I_r \tag{3.1}$$

where Rs is the resistivity, s is the distance between the probe needles (0.72 mm in this case), I_r is the applied current, and V_r is the measured voltage. This resistivity is converted to dopant concentration [180] in order to obtain the axial and radial dopant distribution in each crystal.

3.2.4.3. Illustration of Striation Lines. After the four-point probe measurements, the polished surface is electrolytically etched in a dilute solution of 150 mL of H_2O and 1.9 g of Na_2SO_3 using a graphite cathode with 2 A current [181] to reveal the single/polycrystalline regions as well as the striations that show the interface position and shape during the solidification. In this process, the entire polished surface of the specimen is longitudinally immersed into the solution facing the graphite cathode as shown in Figure 3.4. The specimen as an anode (positive electrode) and the graphite cathode (negative electrode) are connected to a TDK-Lambda (Tokyo, Japan) voltage generator.

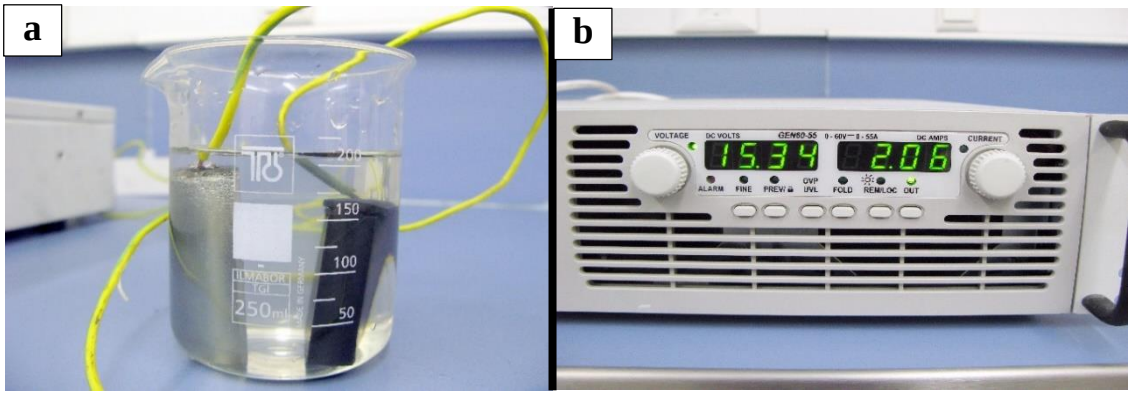

Figure 3.4. Electrolytical etching system for striation lines illustration. (a) the solution (b) the TDK-Lambda voltage generator.

The current is kept constant (2 amps). To illustrate striation lines, the voltage generator is turned on for about 2 minutes to corrode the surface. Then the surface is cleaned and examined. This 2-minute process continued until the surface features appears persistently.

3.3. Numerical Simulation of the Grown Crystals

In order to better understand and analyze the experimental observations, the crystal growth process is simulated to provide a reasonable prediction of the melt flow behavior, temperature distribution, and the interface shape and position in the grown crystals. The simulations are performed in ANSYS Fluent v15.

The material properties listed in Table 3.1 are used in all of the simulations. Since the dopant concentration in the grown crystals is 10^{20} $atom/cc$ ($0.24\,at\%$), there is a correspondingly small difference between the solidus and liquidus temperatures at this composition [3]. Therefore, the solutal effect [182] on melting temperature and natural convection is neglected, and simulations in the VB/AHP/AVC configuration are performed with pure germanium. Simulations were conducted corresponding to each experiment, and two extra simulations in the AHP configuration were performed to analyze the effect of the melt height on crystal growth. Furthermore, a modified baffle shape was used in the AVC configuration in five simulations to see its effect on melt flow characteristics.

Table 3.1. Material properties [21,181]

Substance	Property	Value	Unit
Germanium (melt)	Density	5500	kg/m3
	Specific Heat	380	J/kg-K
	Thermal Conductivity	39	W/m-K
	Viscosity	7.3255e-4	kg/m-s
	Thermal Expansion Coef.	1.1e-4	1/K
	Latent Heat of Fusion	465000	J/kg
	Melting Temperature	1211	K
Germanium (crystal)	Thermal Conductivity	17	W/m-K
Graphite	Density	1840	kg/m3
	Specific Heat	770	J/kg-K
	Thermal Conductivity	65 at 1000℃	W/m-K

3.3.1. Geometry and Mesh Generation

As seen in Figure 3.5, a solid (seed) is placed at the bottom of the simulated cylindrical domain (crucible). Molten Ge is present above the solid, and the solid and liquid are separated by the s/l interface. The baffle is not present in the VB simulation. For the AHP method, the baffle together with the temperature gradient moves upward with a predefined velocity relative to the stationary crucible. Note that in the experiments, the baffle and the temperature gradient are stationary and the crucible is pulled down due to practical necessities. For the AVC method, the baffle vibrates axially while moving upward with the temperature gradient. The vibrational motion of the baffle follows a sinusoidal form. Two imaginary interior surfaces are defined within which the baffle's axial movement and vibration take place. A dynamic mesh is used between the imaginary surfaces, while a static mesh is used in all other regions.

The simulations are performed in a 2D axially symmetric geometry meshed with non-uniform quadrilateral elements as shown in Figure 3.5 except for the VB which uses uniform elements. All the geometries are meshed in ANSYS Gambit 2.4.6 software. In the VB case, the size of the uniform elements is 0.04 mm^2. In the AHP cases, the maximum cell size is 0.04 mm^2 in the liquid and less than 1 mm^2 in the baffle. In the AVC cases, because of high frequency and accordingly high fluid motion, the maximum cell size is 0.02 mm^2 in the liquid and less than 0.5 mm^2 in the baffle to get more accurate results.

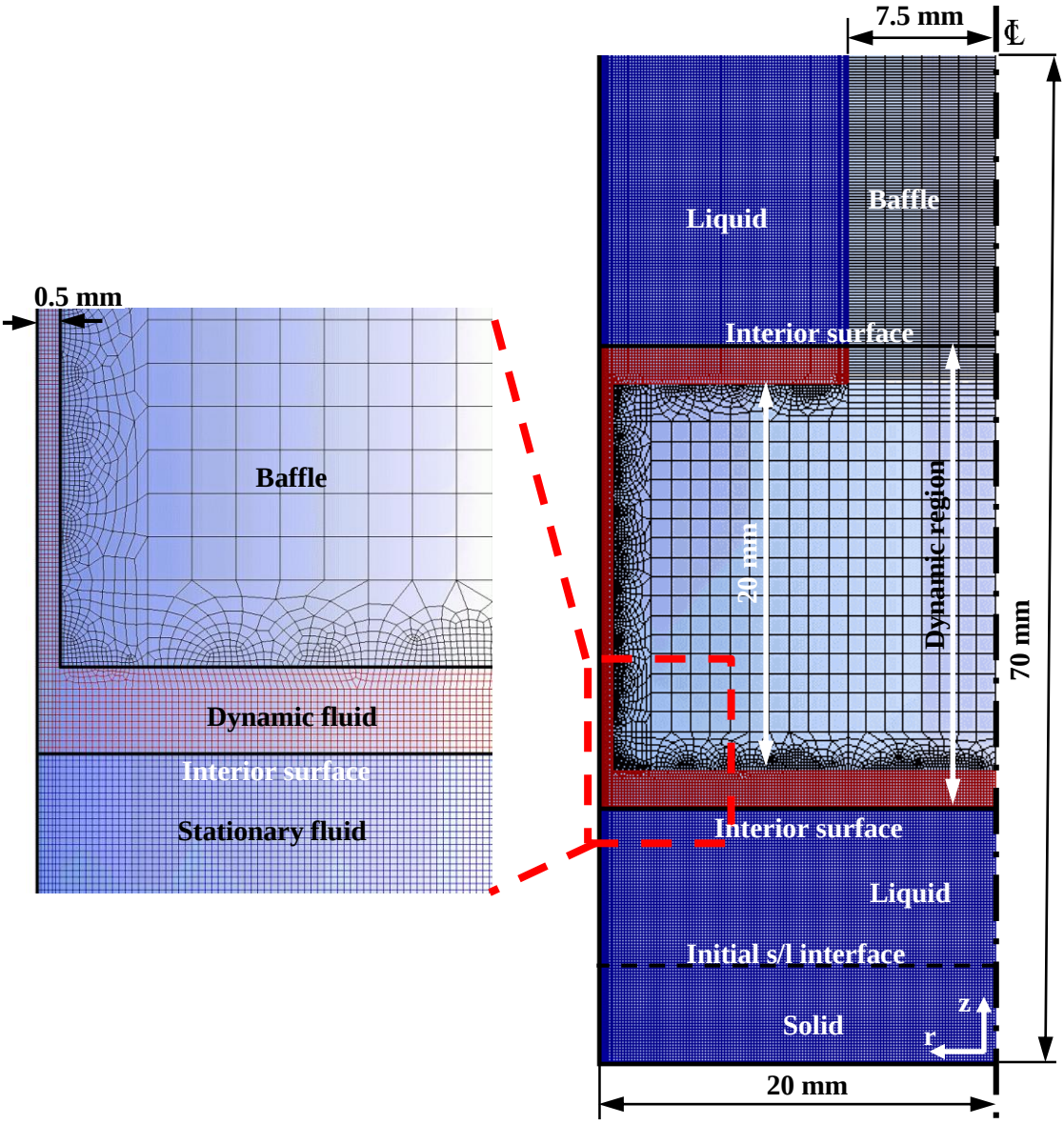

Figure 3.5. Dimensions of simulated domain and its discretization.

In both AHP and AVC cases, the cell size near the walls is consistently less than the other regions, and all edges of the baffle are sharp as it is demonstrated in Figure 3.5.

3.3.2. Governing Equations and Boundary Conditions

The simulated domain is under a positive temperature gradient of 20 K/cm from the bottom up. The gradient is applied at the vertical interior wall of the crucible (left vertical boundary in Figure 3.5). A symmetry boundary condition is applied at the radial center (right

vertical boundary). A no-slip condition is satisfied at all the walls. All fluids are assumed to be incompressible and the flow is laminar.

The solidification/melting module in Fluent which uses enthalpy-porosity method [183] has been used for the solidification process. In this method, the enthalpy (H) results from the sensible enthalpy (h), and the latent heat, ΔH:

$$H = h + \Delta H \tag{3.1}$$

$$h = h_{ref} + \int_{T_{ref}}^{T} c_p d\,T \tag{3.2}$$

where h_{ref} is the reference enthalpy, T_{ref} is the reference temperature, and c_p is the specific heat capacity. The latent heat, ΔH, can be written in terms of the enthalpy of the liquid L and the liquid fraction f_l:

$$\Delta H = f_l L \tag{3.3}$$

f takes the following values at the given temperatures:

$$\begin{aligned} f_l &= 0 && T < T_{liquidus} \\ f_l &= 1 && T > T_{liquidus} \\ f_l &= \frac{T - T_{solidus}}{T_{liquidus} - T_{solidus}} && T_{solidus} < T < T_{liquidus} \end{aligned} \tag{3.4}$$

The velocity components of the melt flow in the r and z directions (V_r and V_z) are obtained from the continuity (Equation 3.5) and momentum equations (Equations 3.6 and 3.7) [184].

$$\frac{\partial \rho}{\partial t} + \frac{\partial (\rho V_z)}{\partial z} + \frac{\partial (\rho V_r)}{\partial r} + \frac{\rho V_r}{r} = 0 \tag{3.5}$$

$$\frac{\partial(\rho V_z)}{\partial t}+\frac{1}{r}\frac{\partial(r\rho V_z V_z)}{\partial z}+\frac{1}{r}\frac{\partial(r\rho V_r V_z)}{\partial r}=-\frac{\partial P}{\partial z}+\frac{1}{r}\frac{\partial\left[r\mu\left[2\partial V_z/\partial z-2\left(\nabla.\vec{V}\right)/3\right]\right]}{\partial z}+\frac{1}{r}\frac{\partial\left[r\mu[\partial V_z/\partial r+\partial V_r/\partial z]\right]}{\partial r}+F_z \quad (3.6)$$

$$\frac{\partial(\rho V_r)}{\partial t}+\frac{1}{r}\frac{\partial(r\rho V_z V_r)}{\partial z}+\frac{1}{r}\frac{\partial(r\rho V_r V_r)}{\partial r}=-\frac{\partial P}{\partial r}+\frac{1}{r}\frac{\partial\left[r\mu\left[2\partial V_r/\partial r-2\left(\nabla.\vec{V}\right)/3\right]\right]}{\partial r}+\frac{1}{r}\frac{\partial\left[r\mu[\partial V_z/\partial r+\partial V_r/\partial z]\right]}{\partial z}-2\mu V_r/r^2+2\mu\left(\nabla.\vec{V}\right)/3r+\rho {V_z}^2/r+F_r \quad (3.7)$$

The body forces (F_z and F_r) in the momentum equations depend on the liquid fraction as [183]:

$$F_z=g\beta_T\left(T-T_{ref}\right)+A_{mush}(V_z)(1-f)^2/(f^3+\varepsilon) \quad (3.8)$$

$$F_r=A_{mush}(V_r)(1-f)^2/(f^3+\varepsilon) \quad (3.9)$$

The first term in F_z is the gravitational force using Boussinesq approximation where β_T is the thermal expansion coefficient of Ge ($0.00011\ [1/\mathrm{K}]$). The second term is the momentum descend due to the reduced porosity in the mushy zone. A_{mush} is a constant (10^6) that forces velocities in solid to zero and ε is a small number (0.001) to keep the term finite. The energy equation for solidification/melting process in a cylindrical coordinate system is written as [183]:

$$\frac{\partial(\rho H)}{\partial t}+\frac{1}{r}\frac{\partial(r\rho V_r H)}{\partial r}+\frac{\partial(\rho V_Z H)}{\partial z}=\frac{1}{r}\frac{\partial(rk(\partial T/\partial r))}{\partial r}+k\partial^2 T/\partial z^2 \quad (3.10)$$

where r and z are radial and vertical coordinates and ρ is the density.

3.3.3. Numerical Modeling and Discretization

In all simulations the pressure-based approach is used to obtain the velocity field. According to this solver, the pressure equation is derived from the continuity and the

momentum equations in such a way that the velocity field, corrected by the pressure, satisfies the continuity. The pressure-based solver uses a solution algorithm where the governing equations are solved sequentially (i.e., segregated from one another). Since the governing equations are non-linear and coupled, the solution loop must be carried out iteratively in order to obtain a converged numerical solution. Two pressure-based solver algorithms are available in ANSYS Fluent, a segregated algorithm and a coupled algorithm. In the segregated algorithm, the individual governing equations for the solution variables are solved one after another. Each governing equation, while being solved, is decoupled or segregated from other equations, as its name. The segregated algorithm is memory-efficient, since the discretized equations need only be stored in the memory one at a time. Among the algorithms that ANSYS Fluent provides for segregated pressure-based solvers, the SIMPLE (Semi Implicit Method for Pressure Linked Equations) is used. This algorithm is adopted because in calculations the pressure and velocity fields are coupled with each other, while neither field is given. The pressure field which is the driving force for flow is initially set. The velocity field is calculated by using the set pressure field such that the continuity equation is satisfied. The SIMPLE algorithm iteratively corrects the calculated pressure and velocity fields. Therefore, as the pressure field converges to an accurate pressure field according to the set residuals, the velocity field approaches an accurate velocity field as well. through the addition of a pressure and velocity correction factors [185].

For the VB, AHP, high amplitude/low frequency AVC simulations, the scaled absolute residual of the continuity and momentum equations is set to 10^{-5} while this value for energy equation is set to 10^{-7} and the solution control under-relaxation factors are 0.3, 1, 1, 0.7, 0.9, and 1 for pressure, density, body forces, momentum, liquid fraction update, and energy respectively. For the low amplitude/high frequency AVC simulations, the residuals are set to 10^{-3} for the continuity equation, 10^{-4} for the momentum equation, and 10^{-6} for the energy equation. The solution control under-relaxation factors in AVC simulations are 0.3, 1, 1, 0.6, 0.9, and 0.8 for pressure, density, body forces, momentum, liquid fraction update, and energy respectively.

The second order upwind discretization scheme for the momentum and energy equations, and the body force weighted discretization for the pressure have been used. In the

AVC cases, the layering dynamic mesh method has been employed to simulate the vibration. For calculations, an adaptive time step is used for the VB, AHP, and high amplitude/low frequency AVC simulations whereas a fixed step of 0.00125 seconds is used for the low amplitude/high frequency AVC case.

It should be noted that in all simulations, the steady solution of the governing equations provides the shape and the position of the initial s/l interface. Then, the solver is switched to transient mode when the baffle and the temperature gradient move upward to initiate the solidification. After getting the simulated results from ANSYS Fluent, they are post processed using ANSYS CFD-Post module to generate useful data and plots to better illustrate and analyze the effective parameters.

4. RESULTS

This section provides experimental results for crystals grown with the VB, AHP, and AVC methods with varying growth parameters, and the simulation results performed with the same growth parameters for validation and with different parameters for prediction and control of crystal quality. Experimentally, one crystal with the VB, three with the AHP, and two with the AVC methods are grown with varying growth parameters. The total length of every grown crystal is about 60 cm. Two extra simulations with different melt heights are also performed to analyze the effect of the melt height on crystal growth in the AHP method. In addition, five more simulations with various baffle size and shape were performed for the AVC method to analyze the effect of baffle shape modification on melt flow and interface stability. This gives a total of thirteen simulations. In each subsection the experimental results (striations and dopant distribution) and simulation results (temperature profile and convective flow) for each sample are provided separately. They are analyzed and compared in the discussion section.

For simplicity, the samples are named as “mmm-ww-xx-yy-zz”, where “mmm” stands for the growth method (VB: vertical Bridgman; AHP: axial heat processing; AVC: axial vibrational control), “ww” the pulling velocity in millimeters per hour, “xx” the initial melt height in millimeters, “yy” the vibrational amplitude in millimeters in AVC cases, and “zz” the vibration frequency in Hertz in AVC cases. In most of the simulations, the annular gap between the baffle and the crucible wall is 0.5 mm. In two simulations where the baffle shape was modified and the gap size is other than 0.5 mm, a “g” term is used in the name of the sample following a number which represents the gap size in millimeters. Moreover, in three simulations of the AVC method a chamfered baffle base was used. In the name of these simulations an “a” term is used following a number indicating the angle of the chamfer. The heights of all chamfers are 5 mm from the baffle base. Table 4.1 presents a complete list of grown samples with their corresponding parameters. The single crystal length in all the crystals is measured from the initial s/l interface to the end of the single crystal region at the center of the crystal.

Table 4.1. Grown/simulated crystals and their growth parameters.

Name	**Parameters**								
	V_p	**h**	**A**	**f**	**g**	**a**	**G_F**	**H**	$I \times 10^{-4}$
AHP-20-2	20	2			0.5		20		
AHP-20-5	20	5			0.5		20	35	
AHP-20-10	20	10			0.5		20		
AHP-20-15	20	15			0.5		20	33.4	
VB-20-58	20	58			0.5		20	14	
AHP-10-10	10	10			0.5		20	41.5	
AVC-20-10-2-0.25	20	10	2	0.25	0.5		20	39	1.25
AVC-20-15-0.25-25	20	15	0.25	25	0.5		20	21.5	1562.50
AVC-20-10-2-0.25-g1	20	10	2	0.25	1		20		1.25
AVC-20-10-2-0.25-g2	20	10	2	0.25	2		20		1.25
AVC-20-10-2-0.25-a10	20	10	2	0.25	0.5	10	20		1.25
AVC-20-10-2-0.25-a20	20	10	2	0.25	0.5	20	20		1.25
AVC-20-10-2-0.25-a30	20	10	2	0.25	0.5	30	20		1.25

V_p: pulling velocity (mm/h), **h**: initial melt height in simulations (mm), **A**: amlitude of vibration (mm), **f**: frequency of vibration (Hz), **g**: annular gap between the baffle and the crucible (mm), **a**: angle of the chamfer of the baffle base (degree), **G_F**: furnace temperature gradient in simulations(°C/cm), **H**: single crystal length measured from initial interface to the last portion of the single crystal region at the center of the crystal (mm), **I**: vibration intensity parameter (m/s^2).

The etched half of each grown crystal indicates the single and poly crystalline regions and the position and shape of the striations during the growth. The initial s/l interface shape was expected to be flat, however, the crystals grown with the AHP method have slanted initial interfaces. After their growth, it is realized that the initial s/l interface of these crystals is positioned at the top boundary of a furnace zone being affected by an asymmetric heat flux. After identifying this issue, the initial s/l interface position is altered to solve this problem for the subsequent VB and AVC samples. Consequently, the VB and AVC crystals have relatively flat initial interfaces, except for the AVC crystals with concavity at the sides due to vibration effects. The concavity of the interface in the AVC crystals is discussed later.

4.1. VB-20-58

The VB method is just used to grow one crystal with 20 mm/h puling velocity to compare with crystals grown with the other two methods. Figure 4.1a shows the longitudinal etched surface illustrating the striations and single length of the crystal. The single crystal

length in this crystal is 14 mm, which is the lowest among all the grown crystals. According to the striations, the concavity of the s/l interface during growth increases and due to instabilities, develops a polycrystalline structure at the center, while the single crystalline structure continues at the sides.

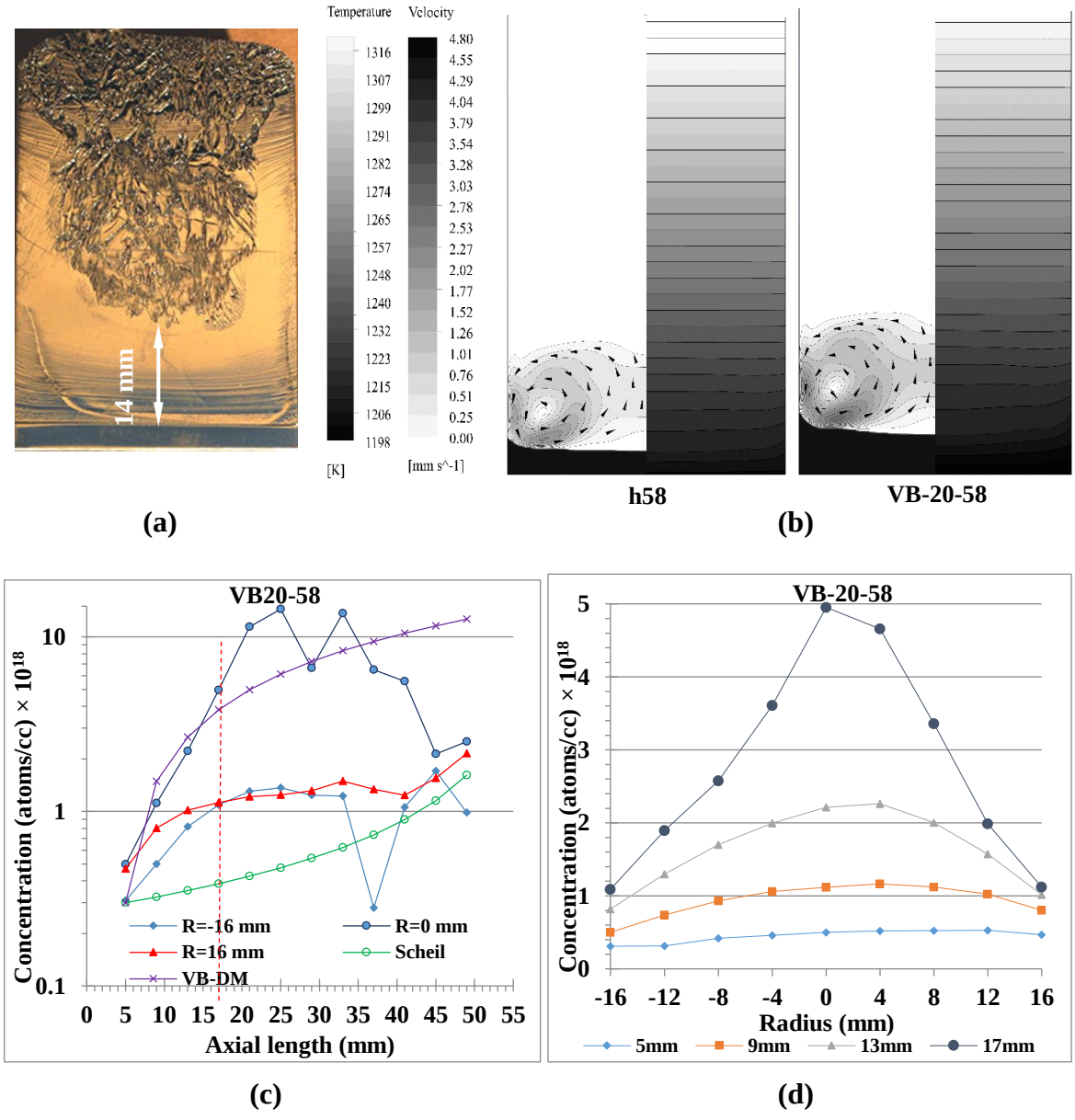

Figure 4.1. The etched surface of the VB-20-58 showing the single/poly crystal regions and striations (a). The initial temperature distribution, interface shape and flow pattern simulation (left-hand-side) and after 600 seconds (right-hand-side) (b). Longitudinal solute distribution (c). Radial solute distribution (d).

Figure 4.1b represents the simulated results for the s/l interface shape, the flow pattern, and the temperature distribution along VB-20-58 crystal after steady state (h58) and 600 seconds of solidification. It shows stronger flow after pulling the crucible down. The convective flow at the beginning is concentrated more towards the crucible wall, while it is radially wider after the onset of pulling. The s/l interface is at the left-hand-side.

Figure 4.1c shows the axial dopant concentration along VB-20-58 crystal at the center and 16 mm away from the center at both sides. The vertical dashed line indicates the single/poly boundary at the longitudinal center line. This concentration is measured in atoms/cc. The concentration at the center is more than at the sides since the convective flow in the melt concentrates the solute in the center of the crystal. This figure shows that from 5 mm until 13 mm above the seed base, the concentration at right side (+16 mm) is more than the left side (-16 mm), which is consequence of weaker convective flow on the right side. In the poly crystalline region, the concentration at the center is still more than at the sides. However, the difference between concentration at the sides is less than the difference with the axial levels in this region.

In addition, the dopant concentration along the whole crystal is shown in Figure 4.1d. Different symbols show radial concentrations at different axial levels. This figure also shows that the center of the crystal has a higher dopant concentration than the sides at all axial positions.

4.2. AHP-20-15

The etched surface of AHP-20-15 in Figure 4.2a show an increasing concavity of the s/l interface during growth. The striations indicate that the concavity of the interface in this crystal is more than that in other AHP crystals. The single crystal length in this crystal is the least among the AHP cases, but it is still about 2 times longer than that in VB-20-58. Figure 4.2b shows a very little difference in flow velocity between the initial condition and after 600 seconds after pulling the crucible.

The axial dopant concentration along AHP-20-15 in Figure 4.2c at the center as before is more than sides. A sharp jump in the concentration at left side of the crystal is

related to an early onset of poly-crystallinity on this side, and is visible in Figure 4.2a as well. The radial dopant concentration along this crystal shown in Figure 4.2d is disordered on the left side, which is a consequence of the poly crystal structure in this region. Less dopant at lower axial levels in comparison to the other AHP cases shows that the larger melt height mixes the melt above the s/l interface more effectively, and reduces the solute build-up at the s/l interface and hence the solute in the solid.

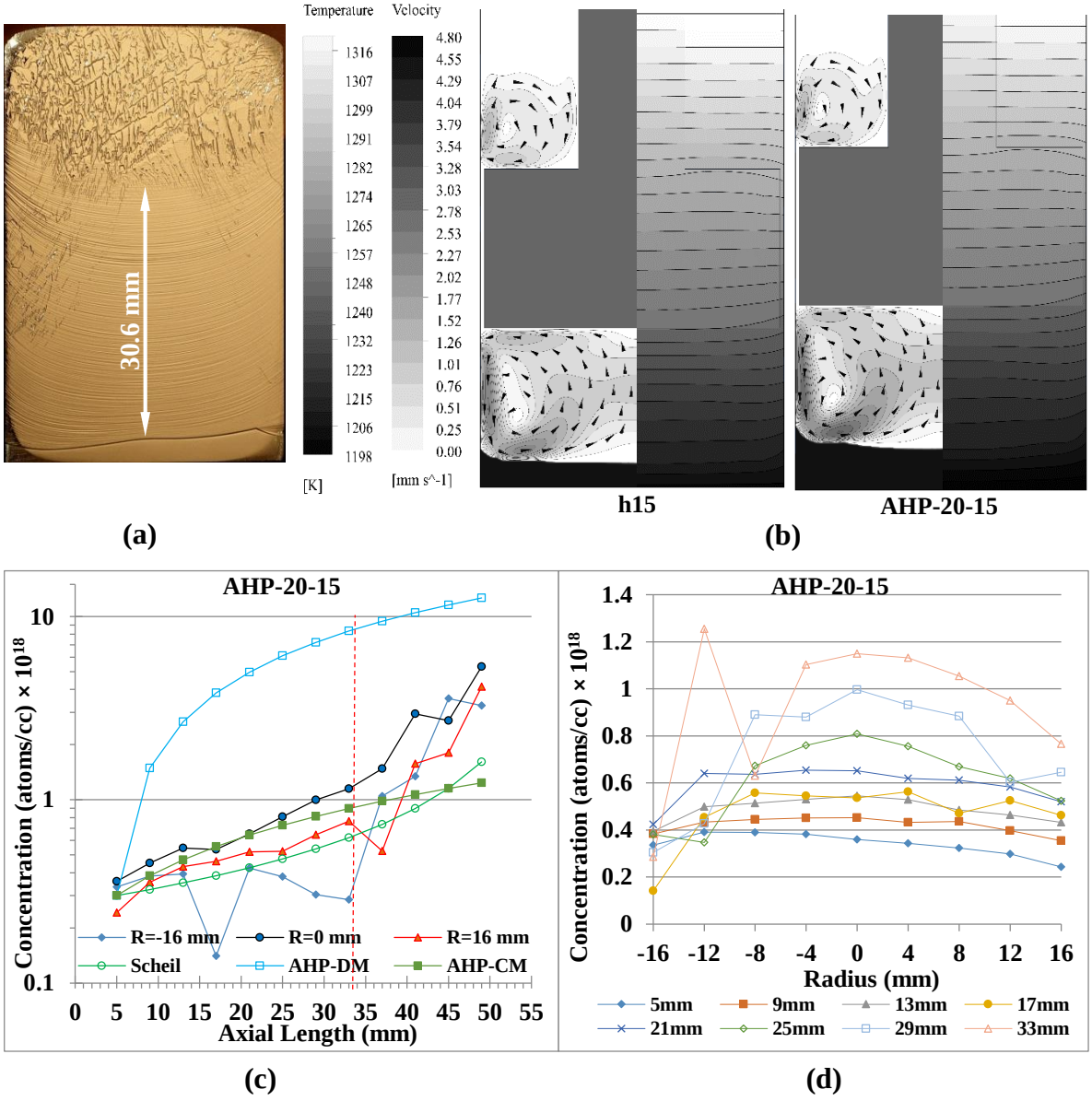

Figure 4.2. The etched surface of the AHP-20-15 showing the single/poly crystal regions and striations (a). The initial temperature distribution, interface shape and flow pattern simulation (left-hand-side) and after 600 seconds (right-hand-side) (b). Longitudinal solute distribution (c). Radial solute distribution (d).

4.3. AHP-20-10 (S)

This sample is just simulated (not grown) to better understand the melt height effect on the s/l interface shape and the flow motion above it. Thus, only the flow pattern and the temperature distribution at the initial condition and after 600 seconds growth are shown in Figure 4.3. In this sample, as well as the other mentioned VB and AHP samples, the convective flow above the interface is stronger after pulling the crucible down. The convective flow is more concentrated toward the crucible wall compared to AHP-20-15.

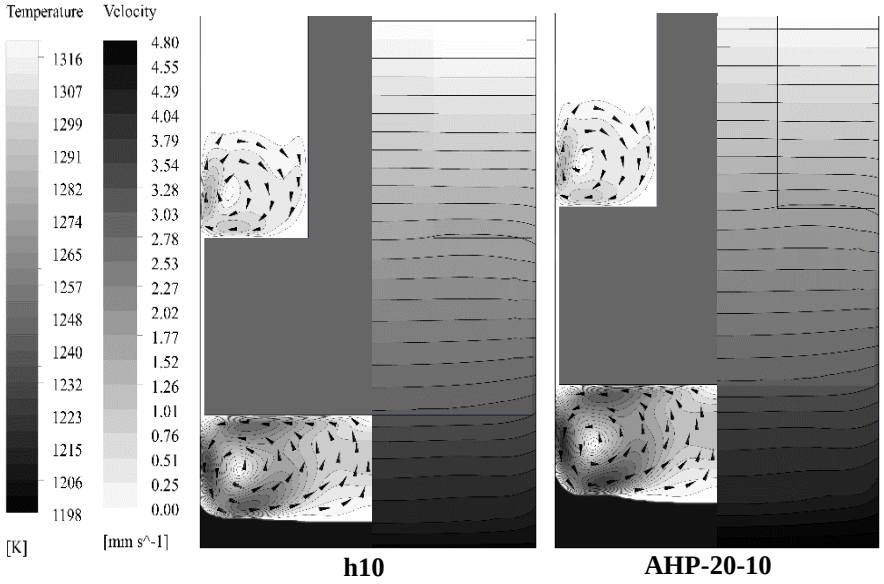

Figure 4.3. Temperature distribution, interface shape and flow pattern in AHP-20-10 simulation after steady state (left) and 600 seconds (right).

4.4. AHP-20-5

The striations and single crystal length of AHP-20-5 with 20 mm/h puling velocity and 5 mm melt height are shown in Figure 4.4a. The single crystal length in this crystal is about 2.5 times that of VB-20-58 with higher melt height. A relatively strong convective cell near the crucible wall below the baffle in this sample is shown in Figure 4.4b, and could justify the linages that develop in the vicinity of the crucible wall in Figure 4.4a. The convective cell is stronger after pulling the crucible. The longitudinal dopant concentration along AHP-20-5 is shown in Figure 4.4c and illustrates a relatively significant difference in dopant concentration between the center and the two sides at the initial s/l interface (5 mm

axial position). At this axial level, the concentration at the center is lower than the sides and the left side has more dopant than the right one. Above the first axial level (5 mm), the dopant concentration becomes more uniform, although the concentration at the right side is consistently slightly lower. The compact lines in Figure 4.4d show more dopant at the same axial levels than in AHP-10-10.

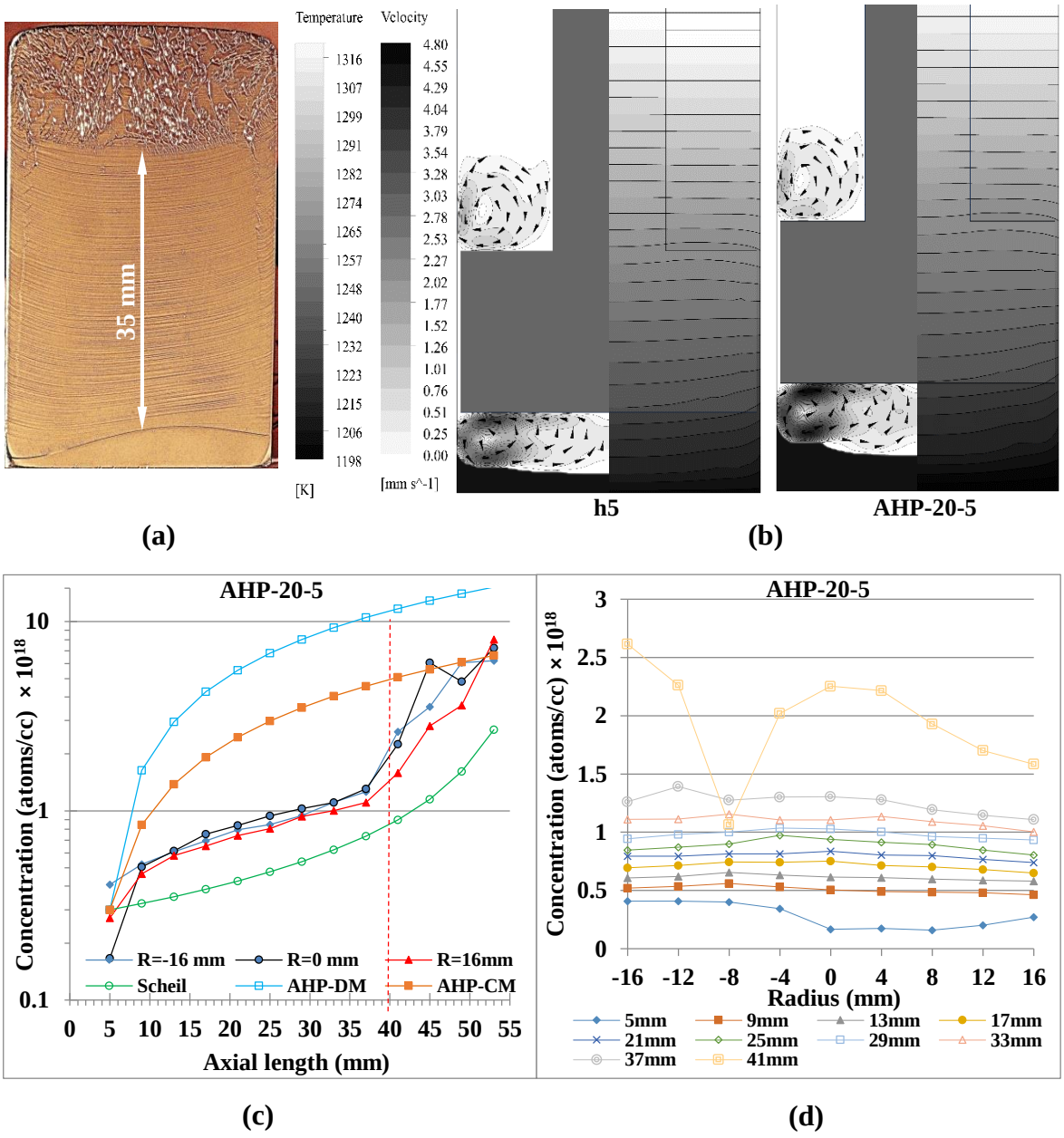

Figure 4.4. The etched surface of the AHP-20-5 showing the single/poly crystal regions and striations (a). The initial temperature distribution, interface shape and flow pattern simulation (left-hand-side) and after 600 seconds (right-hand-side) (b). Longitudinal solute distribution (c). Radial solute distribution (d).

4.5. AHP-20-2 (S)

This sample is just simulated (not grown) to better understand the influence of the melt height on the s/l interface shape and the flow pattern above it. Therefore, for AHP-20-2 only the flow pattern and the temperature distribution are obtained and shown in Figure 4.5. In this figure, the increase in flow velocity and radial temperature gradient is visible. After pulling the crucible down for 600 seconds, the flow covers the melt region above the s/l interface more in radial direction and also the melt height increases significantly.

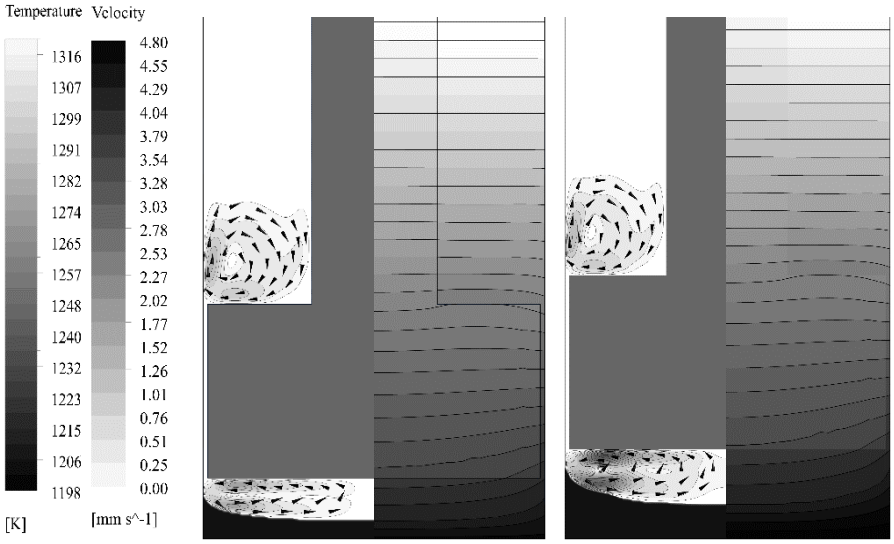

Figure 4.5. Temperature distribution, interface shape and flow pattern in AHP-20-2 simulation after steady state (left) and 600 seconds (right).

4.6. AHP-10-10

AHP-10-10 with 10 mm/h puling velocity is grown to examine the effect of pulling velocity on the quality of the crystal in comparison to the higher velocity of 20 mm/h. Figure 4.6a shows the striations and single crystal length of this crystal. This crystal has the highest single crystal length of all grown crystals, about 3 times longer than the VB-20-58. The striations in this crystal show that the initial slanted interface changes to become symmetric during growth. The simulation results for this crystal are given in Figure 4.6b. The s/l interface shape after 600 seconds shows a relatively strong convective flow that affects the interface.

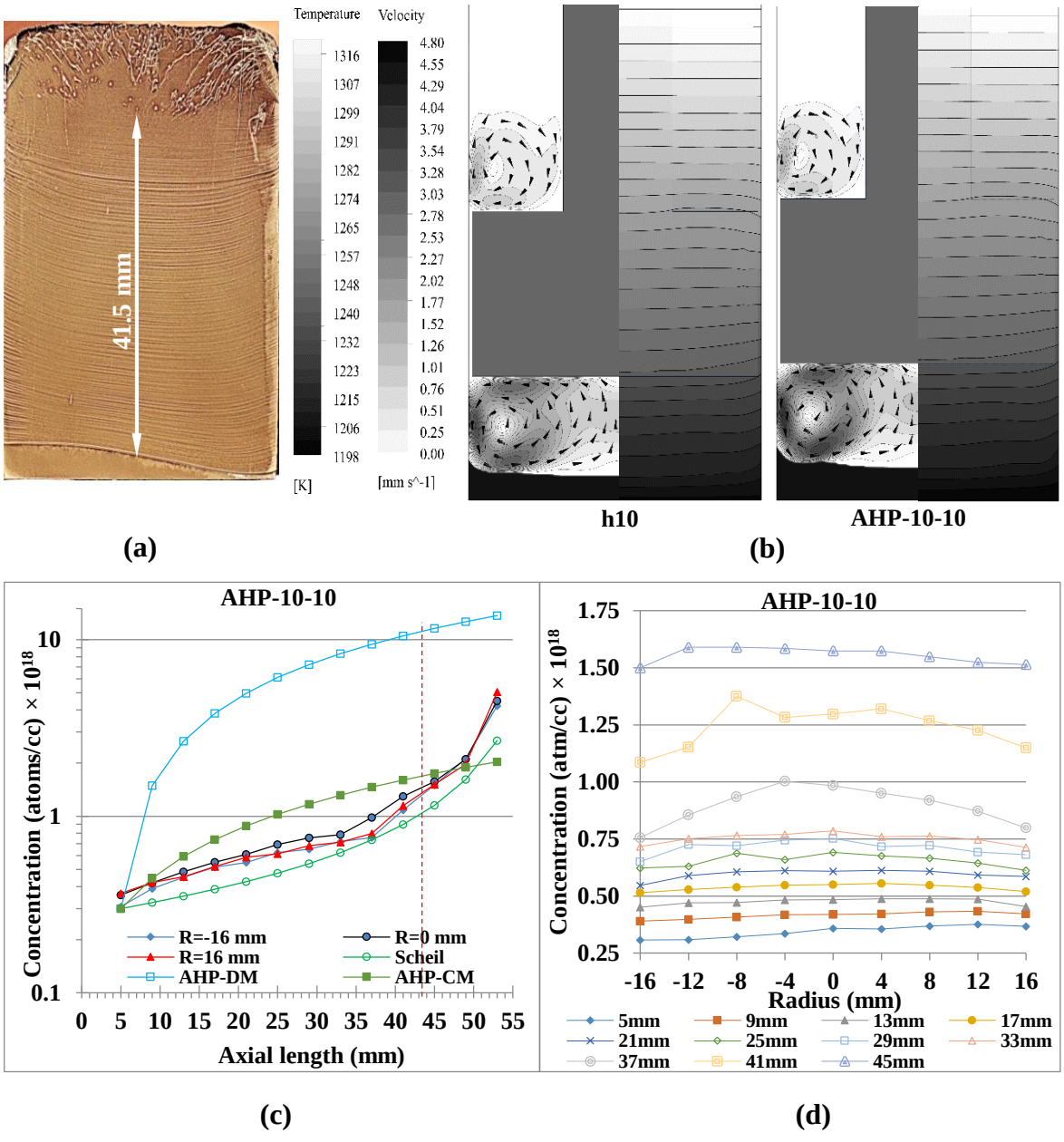

Figure 4.6. The etched surface of the AHP-20-5 showing the single/poly crystal regions and striations (a). The initial temperature distribution, interface shape and flow pattern simulation (left-hand-side) and after 600 seconds (right-hand-side) (b). Longitudinal solute distribution (c). Radial solute distribution (d).

The convective cell after pulling is stronger and also more concentrated at the sides than for the initial condition. The radial temperature gradient also increases after pulling the crucible.

The axial dopant concentration along the VB-10-10 sample at the center and 16 mm away from the center at both sides is shown in Figure 4.6c. The dopant concentration at the

center is very similar to that of the sides of this crystal which furthermore shows a uniform radial dopant distribution in all axial levels in Figure 4.6c. Figure 4.6d confirms that the radial dopant distribution is uniform. The compact lines below 33 mm show a higher quality of the single crystal in this region.

4.7. AVC-20-10-2-0.25

AVC-20-10-2-0.25 with a 20 mm/h puling velocity, 10 mm melt height, 2 mm vibrational amplitude, and 0.25 Hz vibrational frequency is grown to examine the effect of high amplitude and low frequency vibrations. Figure 4.7 shows the striations and single crystal length of this crystal. The initial s/l interface is expected to be flat. However, the forced convective flow due to the vibration melts the interface at the sides. The striations changes slightly in shape and the concavity of the s/l interface decreases slightly at the sides during growth. The asymmetric concavity might be due to the tilted vibrating baffle resulting in unsymmetrical forced convective flow. The single crystal length in this sample is close to that of AHP-10-10, while the pulling velocity is twice as high.

Figure 4.8a shows a higher concentration of dopant in the center of AVC-20-10-2-0.25 as compared to the sides at the initial s/l interface. This might be because of convective motion at sides. After the initial position, the dopant accumulation at the left side is more than at the center or the right side. Figure 4.8b shows the dopant concentration along the whole crystal. Even if the radial dopant distribution at lower levels are not symmetric, these compact lines represent a relatively uniform axial dopant distribution in most parts of the single part of the crystal and shows a comparatively low segregation in the solid.

Figure 4.9 shows the temperature distribution, interface shape, and flow pattern in the AVC-20-10-2-0.25 after 601s at the top, 602s at the middle-down, 603s at the bottom, and 604s at the middle-up positions of the baffle. At the top position, the forced convective cell is closer to the interface rather than the other ones. The top position generates a wider cell. The middle-down position has stronger flow at the center, with a weak clockwise cell induced by the main counterclockwise forced cell. This double-cell side-by-side configuration persists at the bottom position, but the weaker cell vanishes again by the

middle-up position. Despite having different flow cell shape and strength in different axial baffle positions, the interface shape at a cycle of vibration remains unchanged.

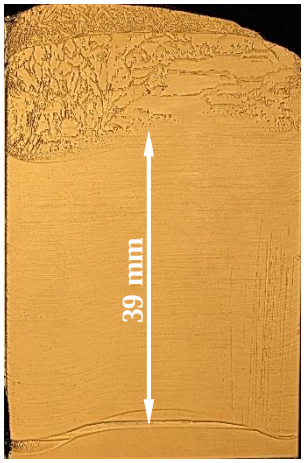

Figure 4.7. The striations and single crystal length of the AVC-20-10-2-0.25.

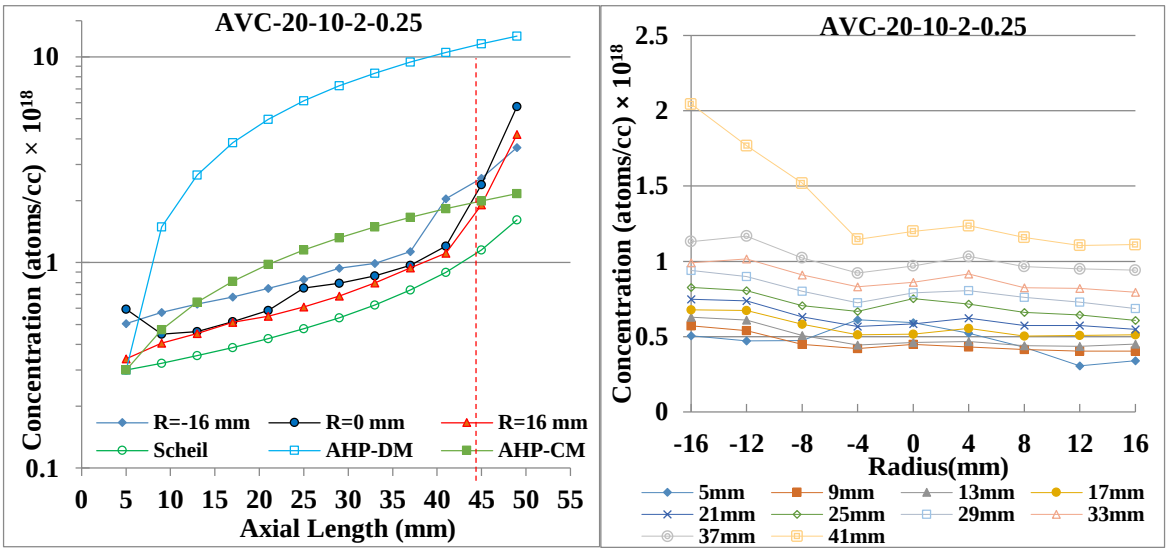

Figure 4.8. Longitudinal solute distribution (a) and Radial solute distribution (b) in AVC-20-10-2-0.25.

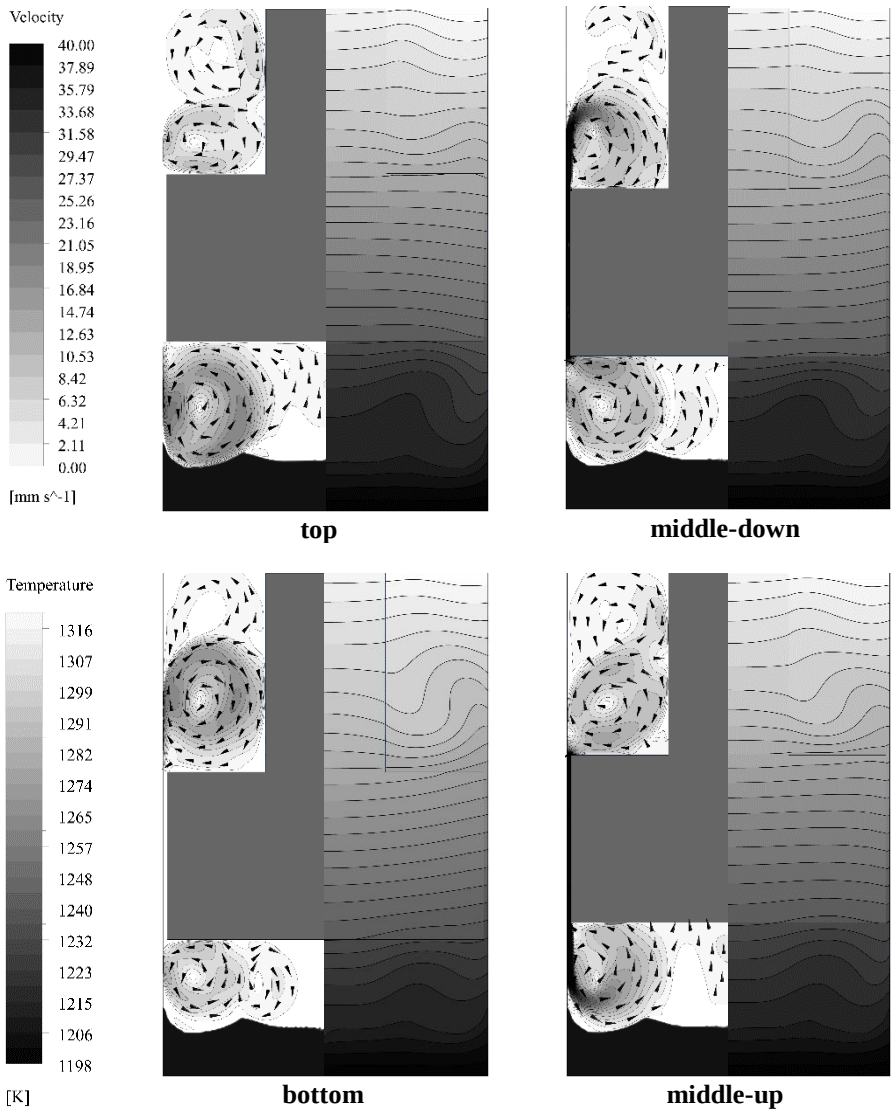

Figure 4.9. Temperature distribution (right), interface shape (left), and flow pattern (left) in the AVC-20-10-2-0.25 after 601s at the top, 602s at the middle-down, 603s at the bottom, and 604s at the middle-up positions.

4.8. AVC-20-15-0.25-25

Figure 4.10 shows the striations and single crystal length of AVC-20-15-0.25-25 with 20 mm/h puling velocity, 15 mm melt height, 0.25 mm vibrational amplitude, and 25 Hz vibrational frequency grown to examine the effect of low amplitude and high frequency of vibration on quality of grown crystal. In this crystal, asymmetric striations might be due to tilted vibrating baffle throughout the growth. More concavity at the left side is observable.

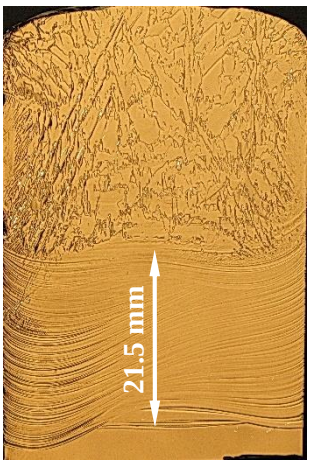

Figure 4.10.The striations and single crystal length of the AVC-20-15-0.25-25.

This also is expected to have a flat initial s/l interface. But, because of the induced vibrational flow, sides are melted after starting the vibration while pulling the crucible down. However, the striations below the poly/single boundary has become symmetric.

The axial dopant concentration along the AVC-20-15-0.25-25 at the center is more than the right side and less than the left side, as it is shown in Figure 4.11a. Figure 4.11b shows the dopant concentration along the entire crystal. This figure shows a low difference in dopant distribution in axial level. The dopant distribution in radial direction in accordance to the striation in Figure 4.10 is not uniform, though.

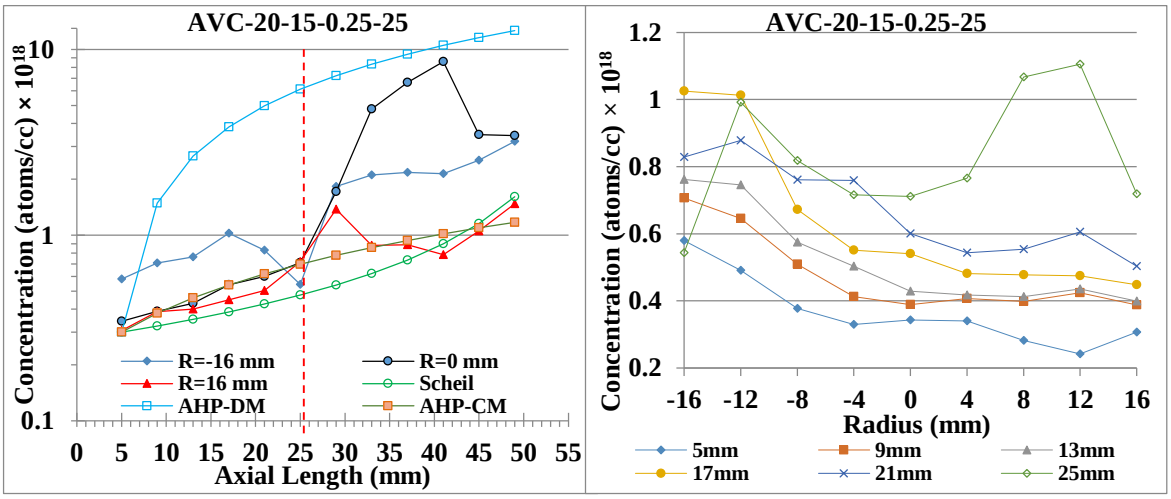

(a) **(b)**

Figure 4.11. Longitudinal solute distribution (a) and Radial solute distribution (b) in AVC-20-15-0.25-25.

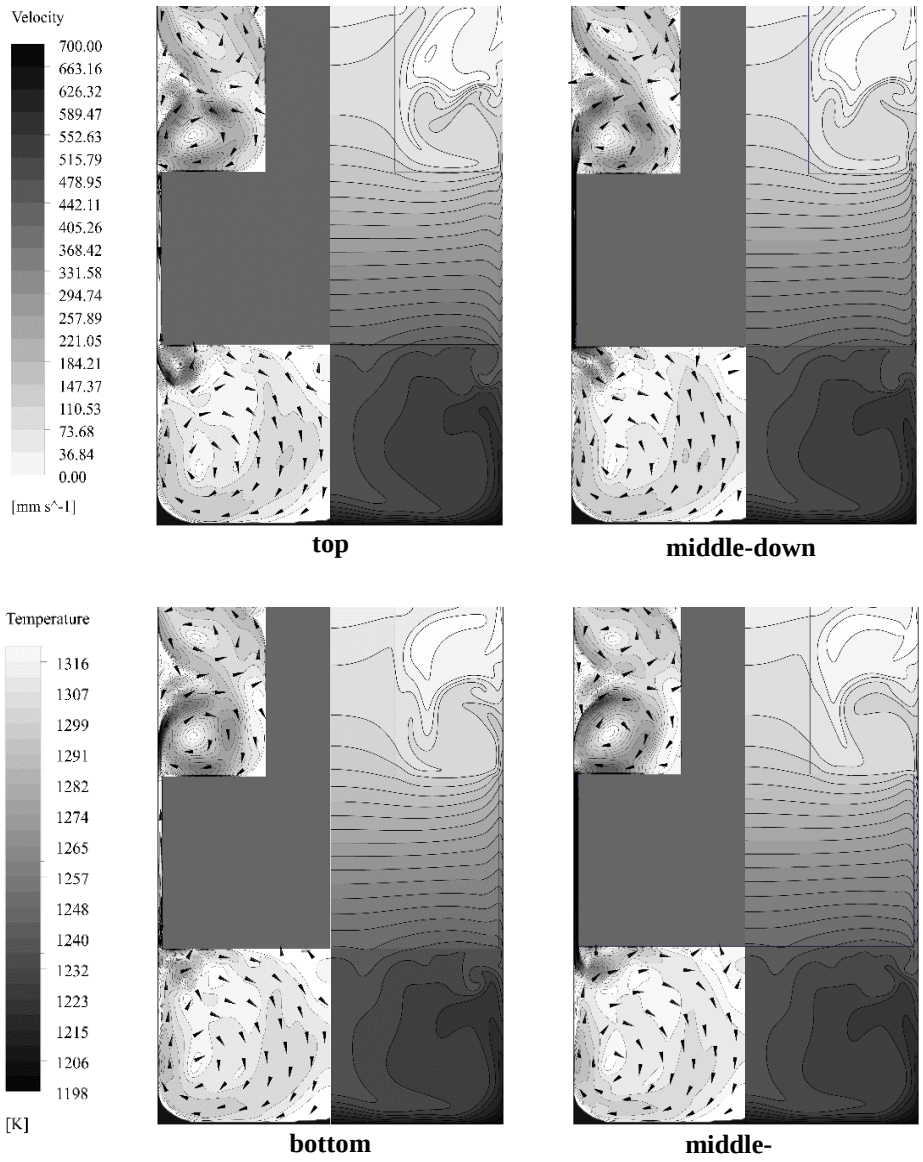

Figure 4.12. Temperature distribution (right), interface shape (left), and flow pattern (left) in the AVC-20-15-0.25-25 after 120.01s at the top, 120.02s at the middle-down, 120.03s at the bottom, and 120.04s at the middle-up positions.

As it is shown in Figure 4.12, in AVC-20-15-0.25-25, there are two developed strong convective cells, one on top of the other one in the melt region below the baffle. The smaller one is a strong counterclockwise forced cell and is attached to the sharp edge of the baffle base near the annular gap [17,100]. The larger induced one circulates within the melt region below the baffle.

4.9. AVC-20-10-2-0.25-g1 (S)

AVC-20-10-2-0.25-g1 is simulated to examine the effect of the increased annular gap between the baffle and the crucible on flow pattern and the s/l interface shape during the growth. The temperature distribution, the interface shape, and the flow pattern of this case after 601s at the top, 602s at the middle-down, 603s at the bottom, and 604s at the middle-up positions of the baffle are shown in Figure 4.13. Similar to AVC-20-10-2-0.25, at the top position, the forced convective cell is closer to the interface rather than the other positions. The top position generates a wider cell. This cell melts the sides of the interface in such a way that the interface looks flat in most parts. The interface shape at a cycle of vibration remains consistent. A second cell is not induced as is seen in Figure 4.13 for AVC-20-10-2-0.25.

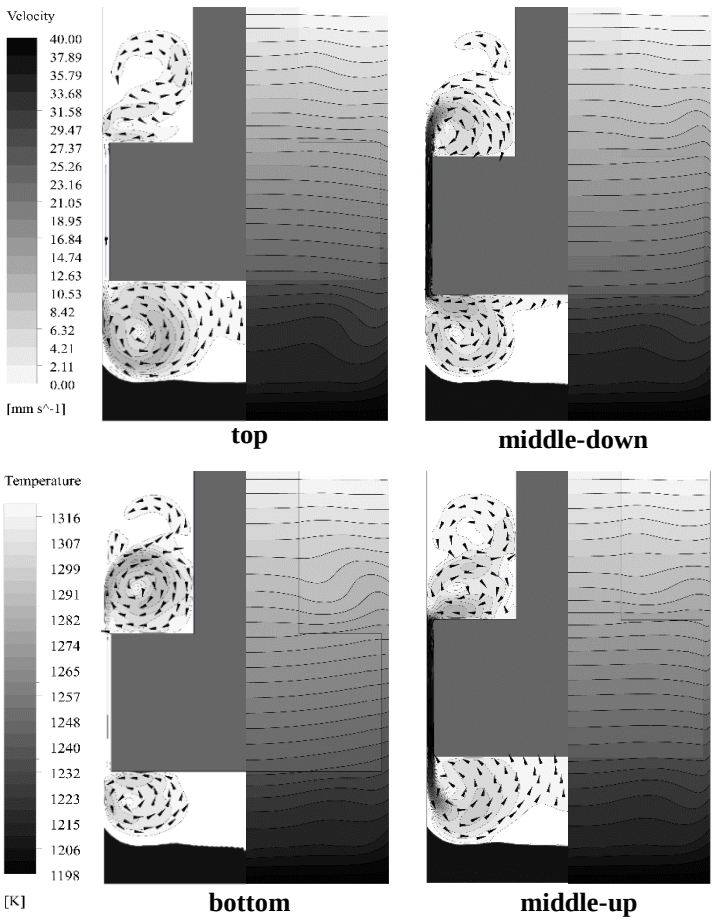

Figure 4.13. Temperature distribution (right), interface shape (left), and flow pattern (left) in the AVC-20-10-2-0.25-g1 after 601s at the top, 602s at the middle-down, 603s at the bottom, and 604s at the middle-up positions.

4.10. AVC-20-10-2-0.25-g2 (S)

AVC-20-10-2-0.25-g2 is also simulated to examine the effect of the increased annular gap between the baffle and the crucible on flow pattern and the s/l interface shape during the growth. The temperature distribution, the interface shape, and the flow pattern of this case after 601s at the top, 602s at the middle-down, 603s at the bottom, and 604s at the middle-up positions of the baffle are shown in Figure 4.14. Similar to AVC-20-10-2-0.25 and AVC-20-10-2-0.25-g1, at the top position, the forced convective cell is wider and more influential to the interface rather than the other positions. The interface shape at a cycle of vibration still remains consistent. In contrast to the two other mentioned cases, the convective motion in this sample generates a more concave s/l interface. An induced cell is not observed.

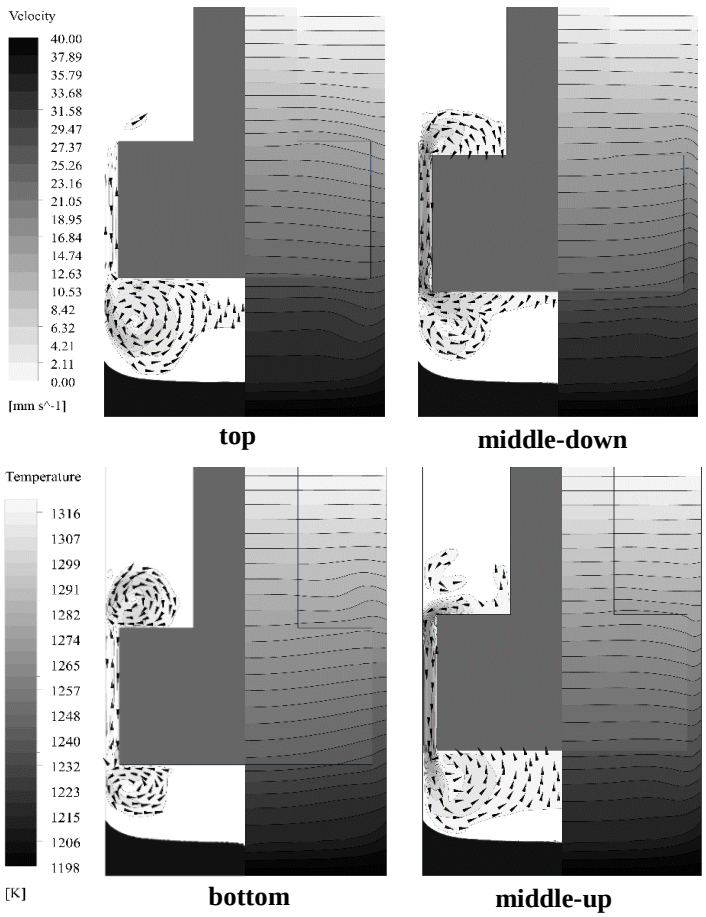

Figure 4.14. Temperature distribution (right), interface shape (left), and flow pattern (left) in the AVC-20-10-2-0.25-g2 after 601s at the top, 602s at the middle-down, 603s at the bottom, and 604s at the middle-up positions.

4.11. AVC-20-10-2-0.25-a10 (S)

AVC-20-10-2-0.25-a10 has a chamfer at the base of the baffle with 5 mm height and 10° angle. This chamfer changes the flow pattern in comparison to the similar case AVC-20-10-2-0.25. Figure 4.15 illustrates the temperature distribution, the interface shape, and the flow pattern of this case at different positions of the baffle. Resembling the AVC-20-10-2-0.25, at the top position, the forced convective cell is wider and more influential to the interface rather than the other positions. The interface shape at a cycle of vibration is not changed and its shape seems mostly flat. An induced cell is not observed.

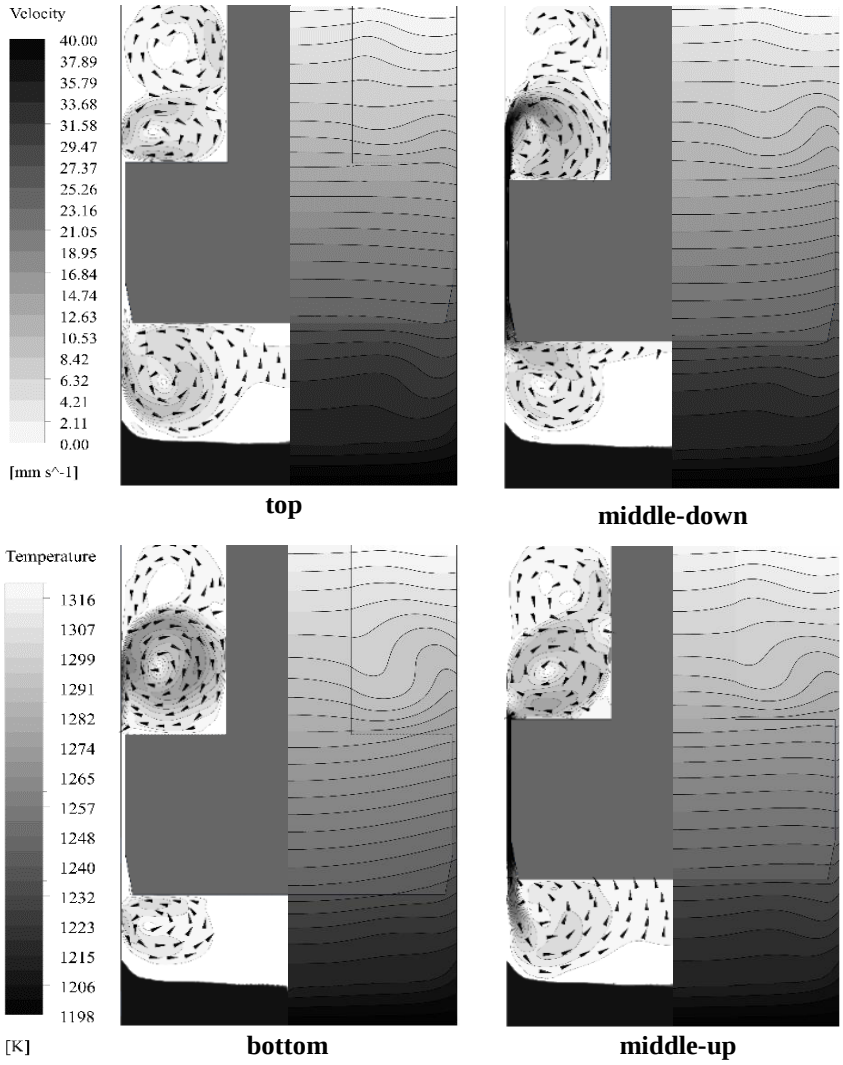

Figure 4.15. Temperature distribution (right), interface shape (left), and flow pattern (left) in the AVC-20-10-2-0.25-a10 after 601s at the top, 602s at the middle-down, 603s at the bottom, and 604s at the middle-up positions.

4.12. AVC-20-10-2-0.25-a20 (S)

AVC-20-10-2-0.25-a20 has a chamfer at the base of the baffle with 5 mm height and 20̊ angle. This shape of the baffle also changes the flow pattern in comparison to the similar case AVC-20-10-2-0.25 resulting in a concave interface. Figure 4.16 shows **t**he temperature distribution, the interface shape, and the flow pattern of this case after 601s at the top, 602s at the middle-down, 603s at the bottom, and 604s at the middle-up positions of the. In this sample the flow strength at the top position is higher than the other positions while it has a small effect on the interface in comparison to the flow in other positions of baffle. The bottom position is very quiescent. An induced cell is not observed.

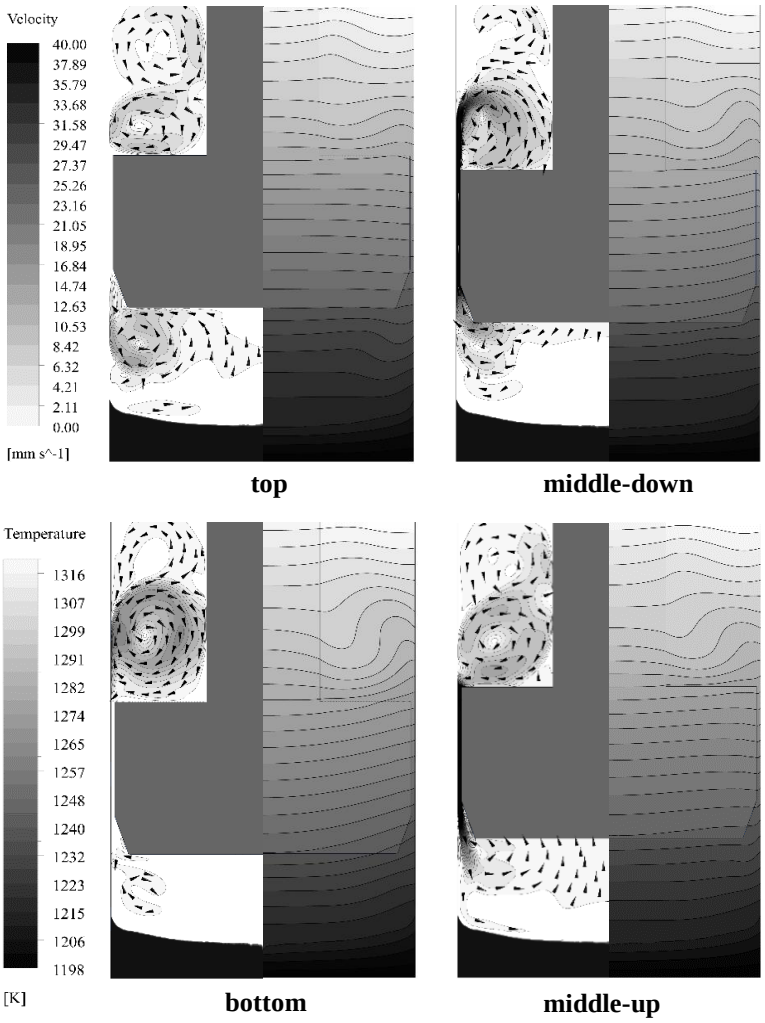

Figure 4.16. Temperature distribution (right), interface shape (left), and flow pattern (left) in the AVC-20-10-2-0.25-a20 after 601s at the top, 602s at the middle-down, 603s at the bottom, and 604s at the middle-up positions.

4.13. AVC-20-10-2-0.25-a30 (S)

The chamfer in AVC-20-10-2-0.25-a30 has 5 mm height and 30° angle resulting in weakened forced flow at the top position. However, in this case, the flow at the bottom and the middle-up positions is more effective on the interface, as shown in Figure 4.17. In this sample the interface is undesirably concave. An induced cell is not observed.

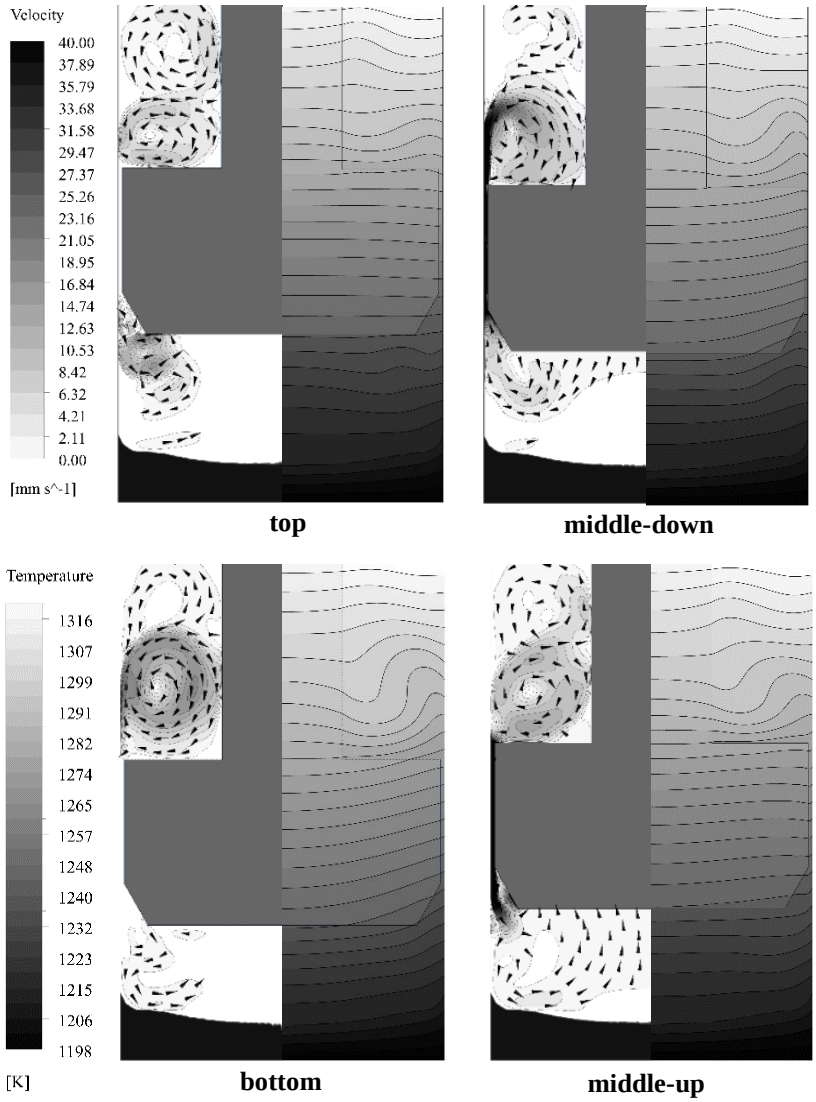

Figure 4.17. Temperature distribution (right), interface shape (left), and flow pattern (left) in the AVC-20-10-2-0.25-a30 after 601s at the top, 602s at the middle-down, 603s at the bottom, and 604s at the middle-up positions.

5. DISCUSSION

Figure 5.1 shows the experimentally grown crystals (left) with simulated results (right). The simulated results are presented after 600 seconds to illustrate the influence of the crucible/baffle pulling and baffle vibration on the interface shape.

The simulations for the VB and AHP crystals are stopped after 4200 seconds. For the AVC crystals, the simulations are continued only until 600 seconds for AVC-20-2-0.25 and 120 seconds for AVC-20-15-0.25-25 due to high computational time and memory cost. The simulations are believed to yield useful data with regard to real experiments (as will be shown later) since the melt flow already becomes stable within the simulated times.

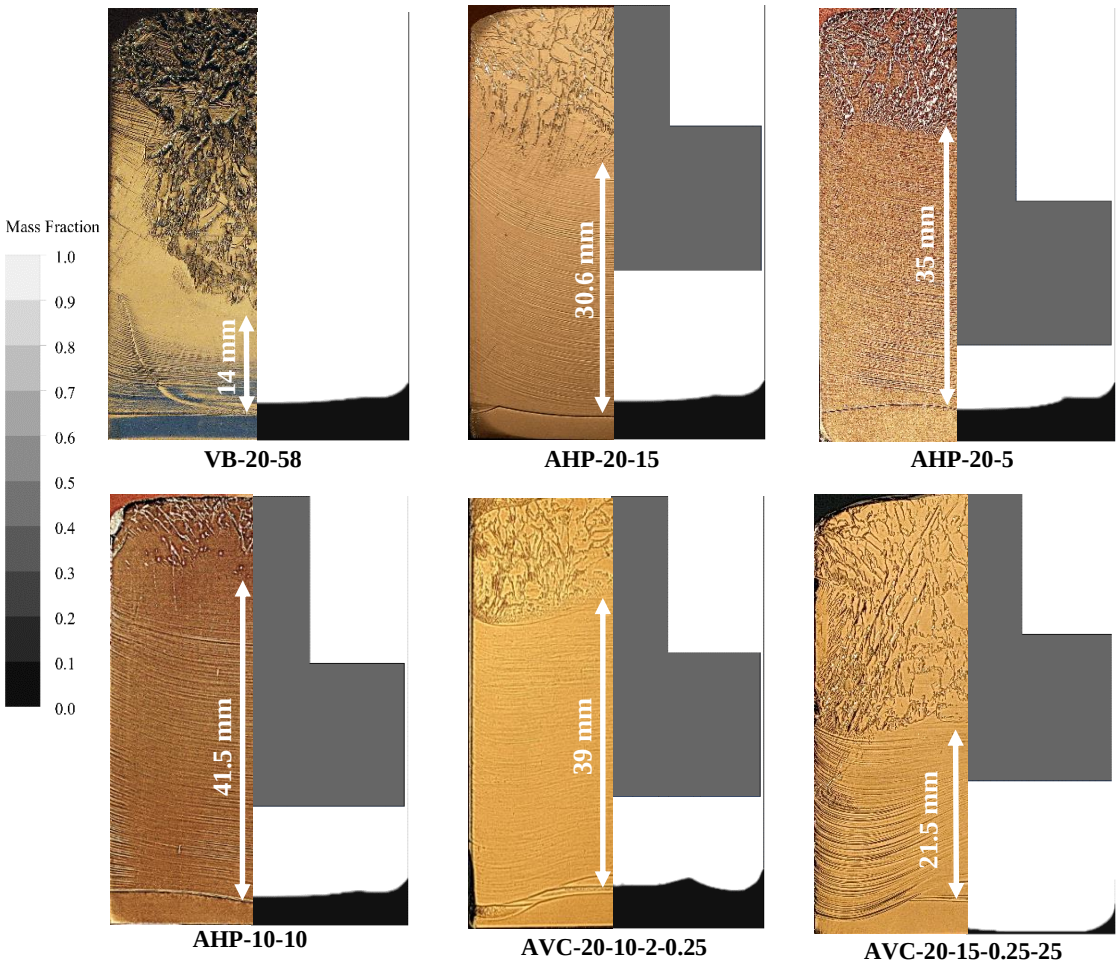

Figure 5.1. The interface shapes observed in the grown crystals (left) and obtained by the simulation (right).

5.1. Convective Flow

Significant improvement in the single crystal length in the grown crystals is believed to be a result of controlled melt flow near the s/l interface. The temperature distribution, flow velocity, and initial s/l interface shape at the initial (stationary) equilibrium for different melt heights are shown in Figure 5.2. A single convective cell consistently develops [186] above the s/l interface. Since the thermal conductivity of the solid Ge (17 W/m-K) is less than that of the liquid Ge (39 W/m-K), the direction of this cell is downward near the crucible wall, which gives a counterclockwise flow centered near the crucible wall [187]. With the largest melt height ($h = 58\ mm$), the flow is more localized toward the crucible wall. While in the other melt heights, the flow strength in the center is more significant. This indicates that as the melt volume between the baffle base and the interface decreases, the melt flowing down through the gap is dictated more efficiently toward the interface. An exception is the $h = 2mm$ case where the solid boundaries surrounding the fluid are believed to slow down the melt flow.

5.1.1. Gap Flow

During crucible pulling in the AHP method, the melt region below the baffle is fed from the region above the baffle. The upper melt flows down to the lower melt through an annular gap between the baffle and the crucible. This small (0.5 mm) gap is used to prevent back diffusion [181] of the dopant to the region above the baffle, and is the same for the AHP and AVC cases for a better comparison. The velocity of the downward flow in the annular gap is almost independent of the axial position. The maximum velocity magnitude of this flow is 0.07 mm/s in AHP-10-10 (V = 10mm/h), and 0.15 mm/s in the other AHP simulations (V = 20mm/h). This indicates that in the AHP cases, the velocity magnitude in the annular gap depends on the pulling velocity rather than the melt height and the annular flow in all AHP cases is so weak that it only slightly increases the strength of the convective cell below the baffle. This means that the convective cell below the baffle is mainly generated by the radial temperature gradient, since the system experiences a positive axial temperature gradient.

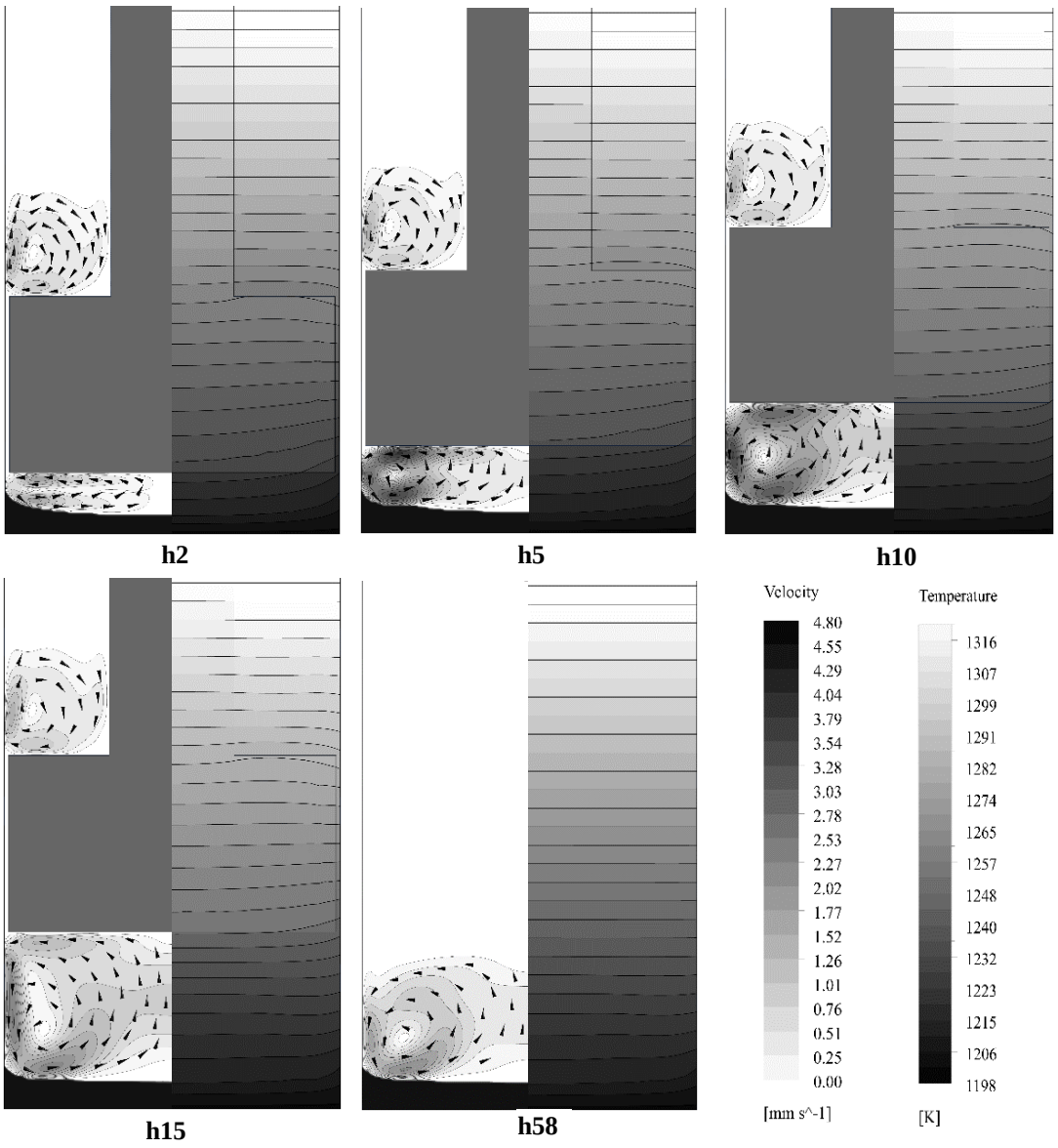

Figure 5.2. Initial stationary temperature distribution (right), interface shape (left) and flow pattern (left) in the VB, AHP, and AVC simulations obtained in the steady state solution. Note that h58 does not use a baffle.

5.1.2. Radial Temperature Gradient

Figure 5.3 shows the radial temperature profile on a horizontal line 6 mm above the seed base after 600 seconds (solid lines) and on a horizontal line 4 mm above the seed base after the stationary, steady state solution before the growth (dashed lines). These positions are nearest to the s/l interface from the liquid side at the respective times. The temperature profiles merge to the same value on the crucible wall because of the same boundary applied

in all cases; the value is greater for AHP-10-10 due to a lower pulling velocity. The temperatures in the center show that the decrease in the melt height results in more axial heat flux to the interface at that location via the high thermal conductivity baffle (k = 65 W/m-K at 1000℃) [181]. However, the temperatures are closer at the side.

The radial temperature gradient in the crystals after 600 seconds at different axial positions from the base of the crystals is shown in Figure 5.4. For AHP-20-10 and VB-20-58, the radial temperature gradient for longer times is also presented in this figure. The reduced melt height gives rise to a higher radial temperature gradient. This result is in contradiction with our original purpose of using a conductive baffle to have a uniform heat supply over the entire interface [90]. Nevertheless, as can be seen in Figure 5.2, the temperature on the baffle is lower at the sides than the center. This becomes more apparent as the melt height decreases. Thus, the high thermal conductivity baffle without a heater is unable to generate a uniform heat flux over the interface. Furthermore, the radial temperature gradient increases with longer solidification time.

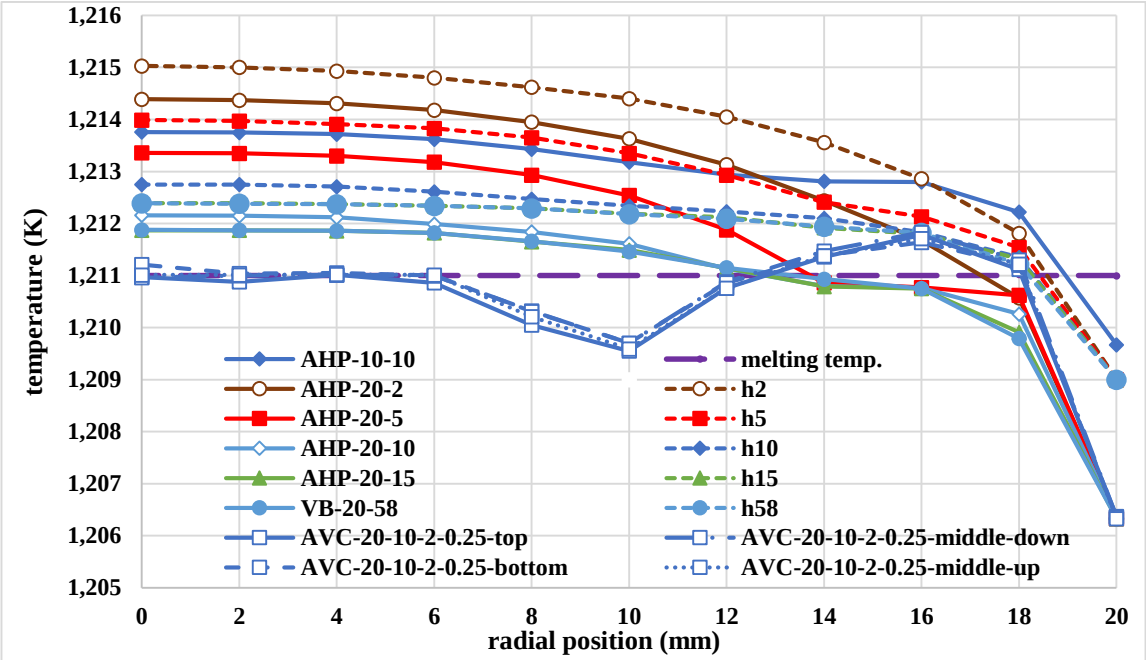

Figure 5.3. Radial temperature profile in the VB and AHP simulations after 600 seconds at 6 millimeters above the seed base (solid curves) and after the initial steady state solution at 4 millimeters above the seed base (dashed curves).

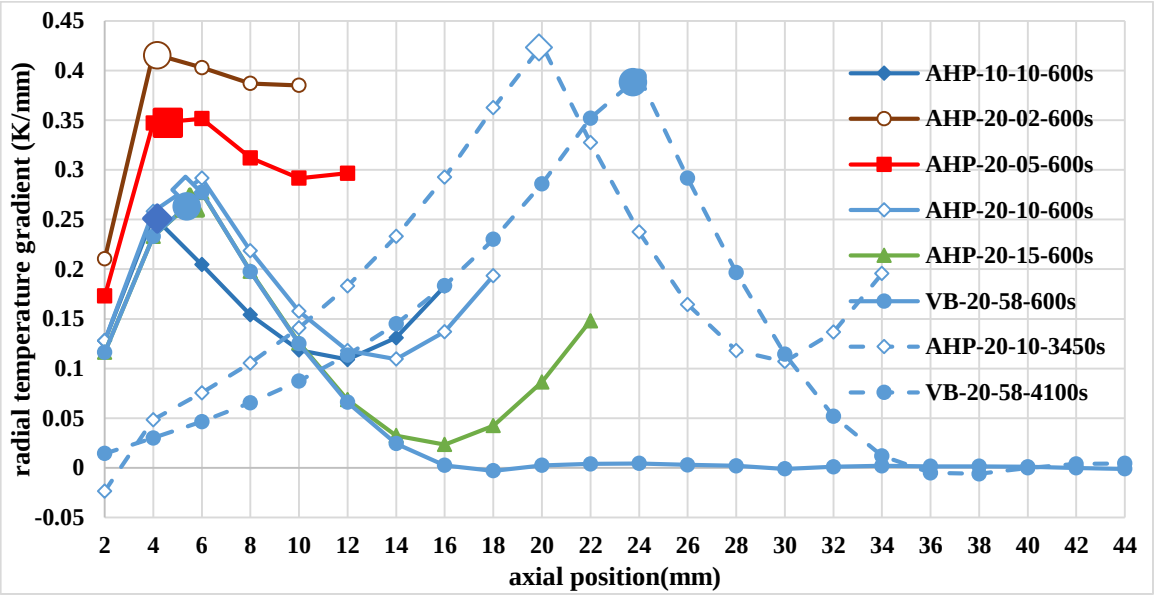

Figure 5.4. Radial temperature gradient in the VB and AHP simulations after 600 seconds at different axial positions from the seed base. Longer times for AHP-20-10 and VB-20-58 are also shown. Large symbols show the s/l interface position and last data point is about 1 millimeter below the baffle base.

In addition, at the given time of 600s in Figure 5.4, the radial temperature gradient does not vary noticeably in the axial direction in the melt with low melt height, while it decreases significantly for the larger melt heights. Again, the longer solidification times increases the radial temperature gradient in the axial direction.

In contrast, increasing the melt height, which means the baffle is farther away from the interface, reduces the radial temperature gradient. Thus, a stronger convective flow is observed in the crystals with a lower melt height. This stronger flow centered toward the crucible wall does not allow the interface on the wall to advance and enables a flatter interface. Possibly, a baffle with a side ring heater in contrast to a uniform base heater can promote a flat interface by reducing the radial temperature gradient.

Figure 5.5 shows the radial temperature profile in the AVC simulations of modified baffle shape after 600 seconds at 7 millimeters above the seed base.

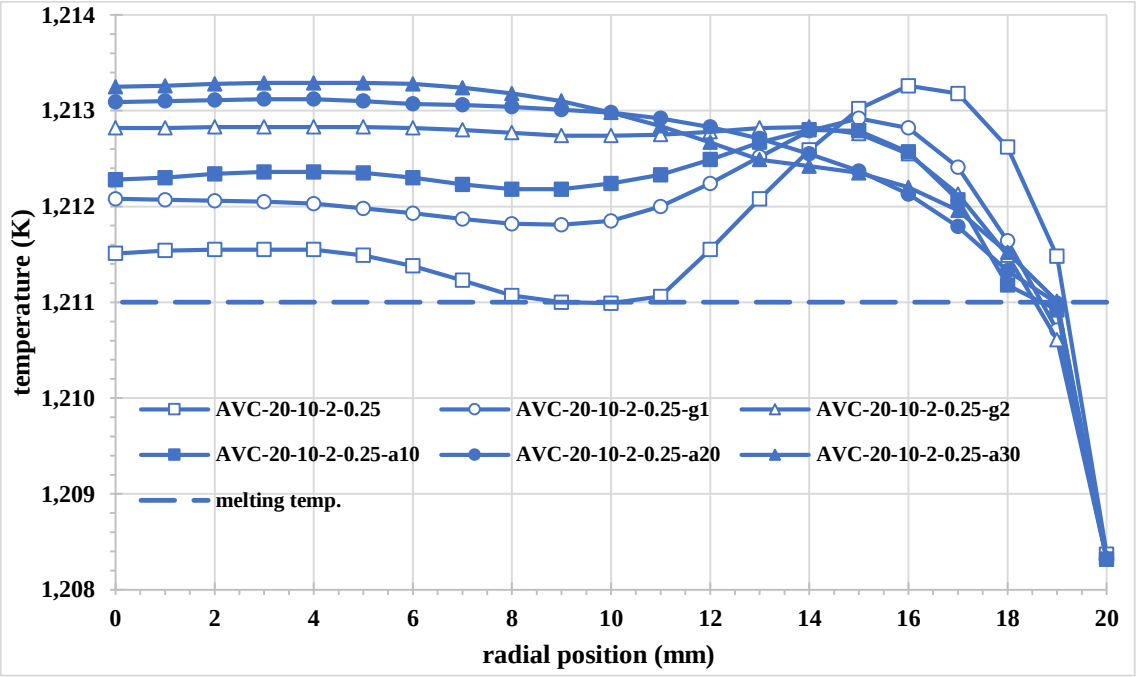

Figure 5.5. Radial temperature profile in the AVC simulations of baffle shape modification after 600 seconds at 7 millimeters above the seed base.

Since the lines in this figure resemble the temperature on a line near the interface, they are a fair representation of the interface shape, as well. AVC-20-10-2-0.25 shows the least temperature at the center and the most temperature at sides. Increasing the annular gap in AVC-20-10-2-0.25-g1 and AVC-20-10-2-0.25-g2 decreases the temperature at the center and lowers it at sides and results in a flatter interface. Use of the chamfer at the base of the baffle also increases the temperature at the center and decreases it at sides. In AVC-20-10-2-0.25-a10 is hotter at the center compared to AVC-20-10-2-0.25 and AVC-20-10-2-0.25-g1. However, it is colder at the center than AVC-20-10-2-0.25-g2. Increasing the angle of the chamfer leads the hot flow coming from the gap to the center and makes the interface more concave. Furthermore, AVC-20-10-2-0.25-g1 and AVC-20-10-2-0.25-a10 have a similar pattern. It is apparent that a wider gap can help to reduce the radial gradient while the chamfer increases it.

5.1.3. Flow Velocity (V)

Figure 5.6a shows the velocity magnitude of the flow at 1 millimeter above the s/l interface after the initial (stationary) equilibrium solution (dashed lines) and after 600

seconds of pulling (solid lines). In all the cases, after applying the pulling velocity, the strength of the convective cells increases. This is a result of increased radial temperature gradient with crucible pulling as seen in Figure 5.3. The flow velocity magnitude peaks in the region from 10 mm to 20 mm radial positions in all the cases. The magnitude is smallest in AHP-20-2. Interestingly, it is maximized with AHP-20-5, and then the magnitude decreases as the melt height increases. It is shown that the magnitude after 15 mm melt height stays roughly the same; AHP-20-15 and VB-20-58 have a similar trend and value for the velocity magnitudes. Furthermore, the radial position of the maximum velocity magnitude shifts toward the center as the melt height increases. In the radial range from 0 mm to 8 mm, the lower the melt height, the greater the velocity magnitude. Thus, a better mixing is obtained with lower melt height, resulting in a flatter interface. A weaker flow towards the center with increased melt height is also mentioned above and seen in Figure 5.2 for the stationary conditions. The time varying velocity magnitude profiles in Figure 5.6b indicate the stability of the flow after about 2400 seconds, and that the flow is nearly stable already after 300 seconds.

The variation in the maximum velocity magnitude of the flow during solidification for the VB and the AHP simulations is shown in Figure 5.7. Following an initial increase, the flow becomes stable after about 2400 seconds in the crystals with 20 mm/h pull velocity and after about 600 seconds in AHP-10-10. As deduced from Figure 5.6, Figure 5.7 also indicates that flow approaches stability after about 300 seconds. The trend of the curves in Figure 5.7 shows that the weakest flow belongs to the highest melt height (VB-20-58), providing further evidence that an immersed baffle increases the flow velocity for an efficient melt mixing. A comparison between AHP-20-10 and AHP-10-10 both in Figures 5.6 and 5.7 shows that the flow velocity is mostly dictated by the melt height rather than the pulling velocity.

For the simulated cases of modified baffles in the AVC configuration the maximum flow velocity when the baffle is at the top position and the gap flow velocity in the radially middle of the annular gap at the axial position of 10 mm above the baffle base during the baffle's middle-up stroke are given in Table 5.1. The data indicate that increasing the gap size decreases both the gap flow velocity and the flow velocity below the baffle at the top

position. In contrast, an increased chamfer yields an initial drop and then an increase in both the maximum flow velocity and the gap flow velocity.

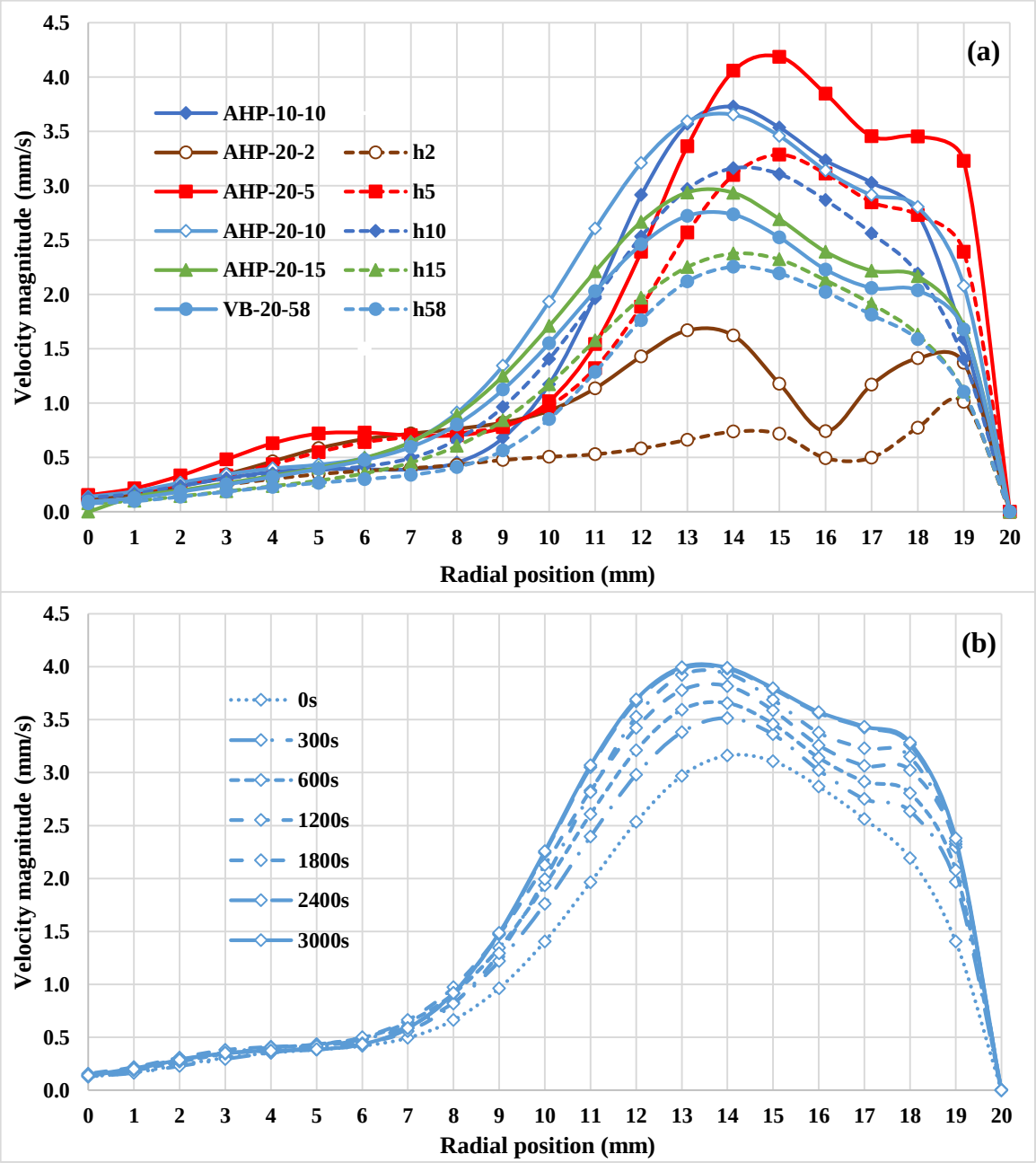

Figure 5.6. Velocity magnitude in the VB and AHP simulations for initial stationary solution (dashed curves) and after 600 seconds (solid curves) 1 millimeter above the interface at the center (a). Velocity magnitude in AHP-20-10 simulation from initial stationary condition (0 seconds) to 3000 seconds at 1 millimeter above the interface at the center. The lines at 2400s and 3000s overlap (b).

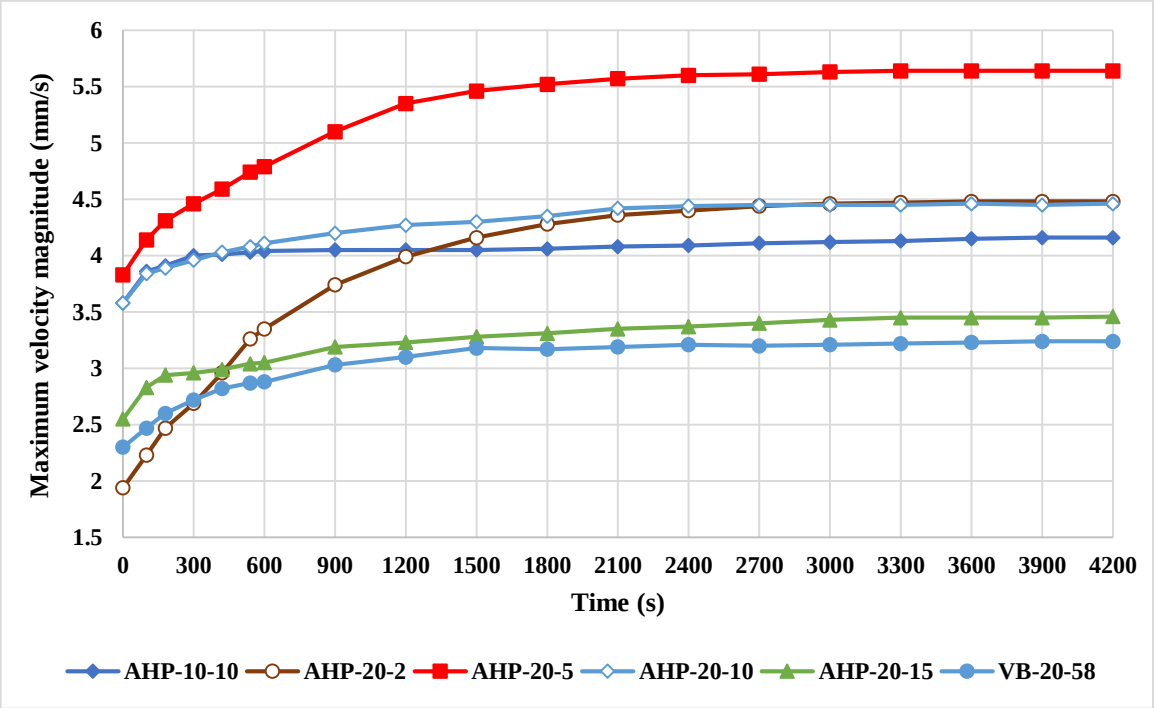

Figure 5.7. Maximum fluid velocity magnitude in all the VB and AHP simulations.

Table 5.1. The maximum flow velocity when the baffle is at the top position, and the flow velocity in the annular gap when the baffle is at the middle-up position.

Case	Maximum Velocity (mm/s)	Gap Velocity (mm/s)
AVC-20-10-2-0.25	23.99	80.95
AVC-20-10-2-0.25-g1	16.35	40.26
AVC-20-10-2-0.25-g2	11.52	17.86
AVC-20-10-2-0.25-a10	14.22	59.68
AVC-20-10-2-0.25-a20	16.26	81.08
AVC-20-10-2-0.25-a30	20.23	81.02

Increasing the gap from 0.5 mm to 1 mm decreases the maximum velocity significantly (32%), while this change in velocity is relatively smaller for a further increase from 1 mm to 2 mm (29%). The gap flow velocity decreases for 50% by increasing the gap from 0.5 mm to 1 mm and similarly it has 55% decrease when the gap increases from 1 mm to 2 mm. Comparing the AVC-20-10-2-0.25 case with chamfered baffle base shows that the maximum flow velocity below the baffle is lowest for the lowest angle of chamfer (a10) while the related figures in Results section shows that the baffle with lower chamfer angle affects the s/l interface more. While, the lower angle decreases the flow velocity significantly, flow accelerates when the chamfer angle increases. From the gap flow velocity,

it can be seen that the lower chamfer angle has an important effect on lowering the flow in the gap. In AVC-20-10-2-0.25-a10, the gap flow velocity is 26% less than the case without chamfer while the other two cases with 20 and 30 degree chamfer do not change the gap flow velocity. It shows that the flow in the gap deaccelerates when hits the strong convective flow below the baffle in middle-up position shown in Figure 4.15.

5.1.4. Growth Rate

The interface position in the center of the crystals at different times is shown in Figure 5.8. The inset in this figure shows the beginning of the solidification. The interface is sluggish at the beginning as reported experimentally [188], and begins advancing after about 100 seconds. The growth rate approaches the pulling rate after about 2400 seconds as seen in Figure 5.8b, which shows the deviation between the pulling velocity and the simulated interface growth velocity. The deviation here indicates a recession in the interface growth rate. Thus, the reduced interface growth velocity with low melt height can be justified on the basis of the axial heat flux to the interface through the thermally conductive baffle. The percent deviation is similar in all cases in later times.

AHP-10-10, AHP-20-10, and AVC-20-10-2-0.25 have equal initial seed and melt heights, but after applying the pulling velocity they grow with different initial rates because of differently evolved convective cells. In AVC-20-10-2-0.25, the forced convective cell has the highest effect at the 16 mm radial position, and even arrests interface growth in this region for a while. After 180 seconds the interface starts growing in this region, as shown in Figure 5.2. At the center, the growth rate in AVC-20-10-2-0.25 is greater than all the other cases indicated by the lowest deviation in Figure 5.8b. As a result of the forced convective cell at the sides, the interface in AVC-20-10-2-0.25 generates a deep side concavity at the beginning and since the growth rate at the side increases in time, the concavity near the crucible wall vanishes in time. Then, the interface takes a more planar form in the later stages of the growth, as seen in Figure 5.1. Most of the seed in the AVC-20-15-0.25-25 melts in approximately 15 seconds, due to very strong convective cell. All available algorithms and discretization methods in Fluent are tested to conduct the most accurate simulation in this crystal. In addition, several under relaxation factors and residuals are tried to test their

influence on solidification. The variation in different simulation approaches is insignificant, and none resulted in solidification within the simulated time of 120 seconds in this crystal.

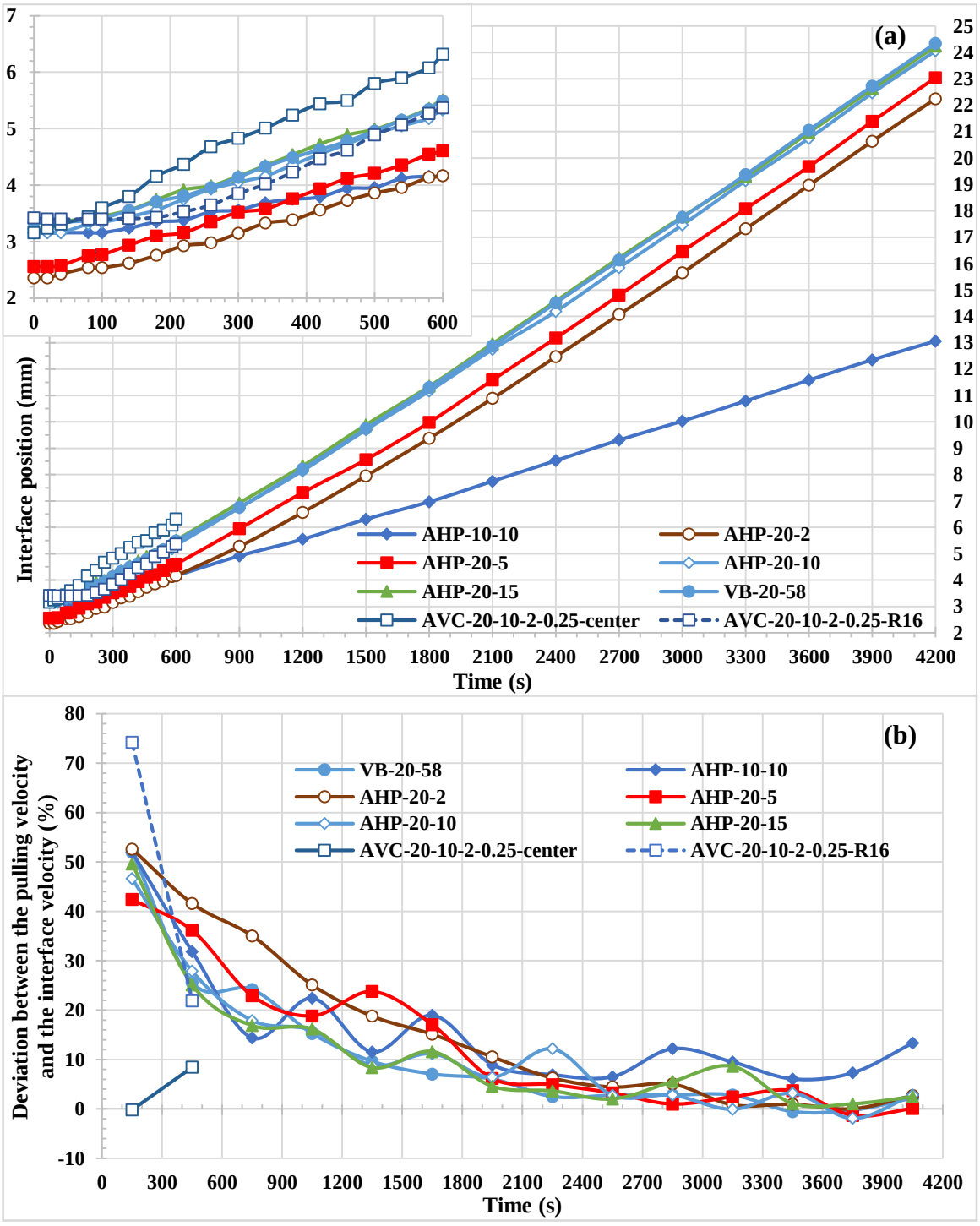

Figure 5.8. The interface position during the solidification process (a). Deviation between the pulling velocity and the interface velocity (b).

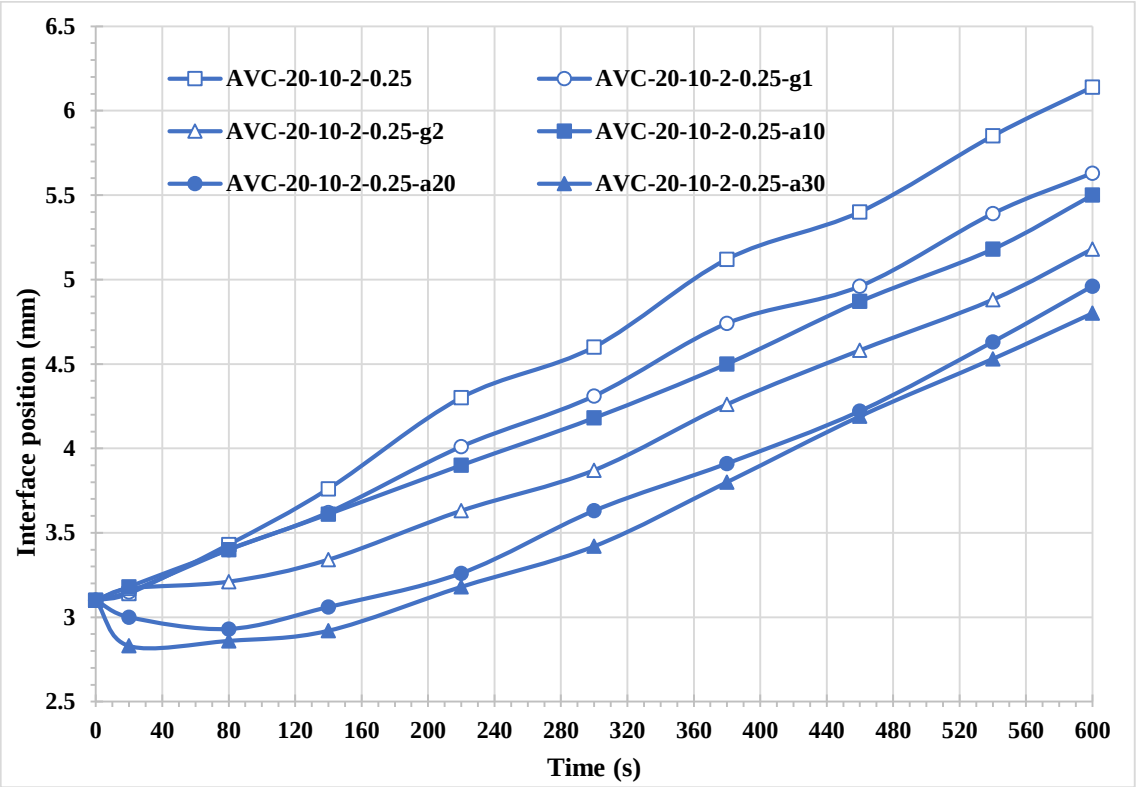

Figure 5.9. The interface position during the solidification process. Measured at the center line relative to the seed base.

Figure 5.9 shows the interface position of the AVC cases with modified baffle shape from the beginning of the solidification to 600s. The slope of these lines represent the growth rate of the s/l interface. In AVC-20-10-2-0.25 which has a strong flow at sides rather than the center, the growth rate is the most. Increasing the gap size conducts the flow coming from the gap to the center of the interface and lowers the growth rate. Likewise, increasing the angle of the chamfered baffle increases the effect of flow at the center. This actually melts the interface back at the beginning of the pulling of crucible in AVC-20-10-2-0.25-a20 and AVC-20-10-2-0.25-a30.

5.1.5. Melt Height (h)

Figure 5.10a demonstrates the melt height versus time during the crucible pulling. The melt height in the AVC crystals is calculated at the middle position of the baffle's vibration cycle. The melt height increases during the growth in all the simulations, but tends to stabilize after about 2400 seconds. The variation in the melt height is a direct consequence

of the deviation between the s/l interface velocity and the pulling velocity. As the relative velocity of the baffle to the crucible is constant, a change in the melt height indicates a different interface growth velocity.

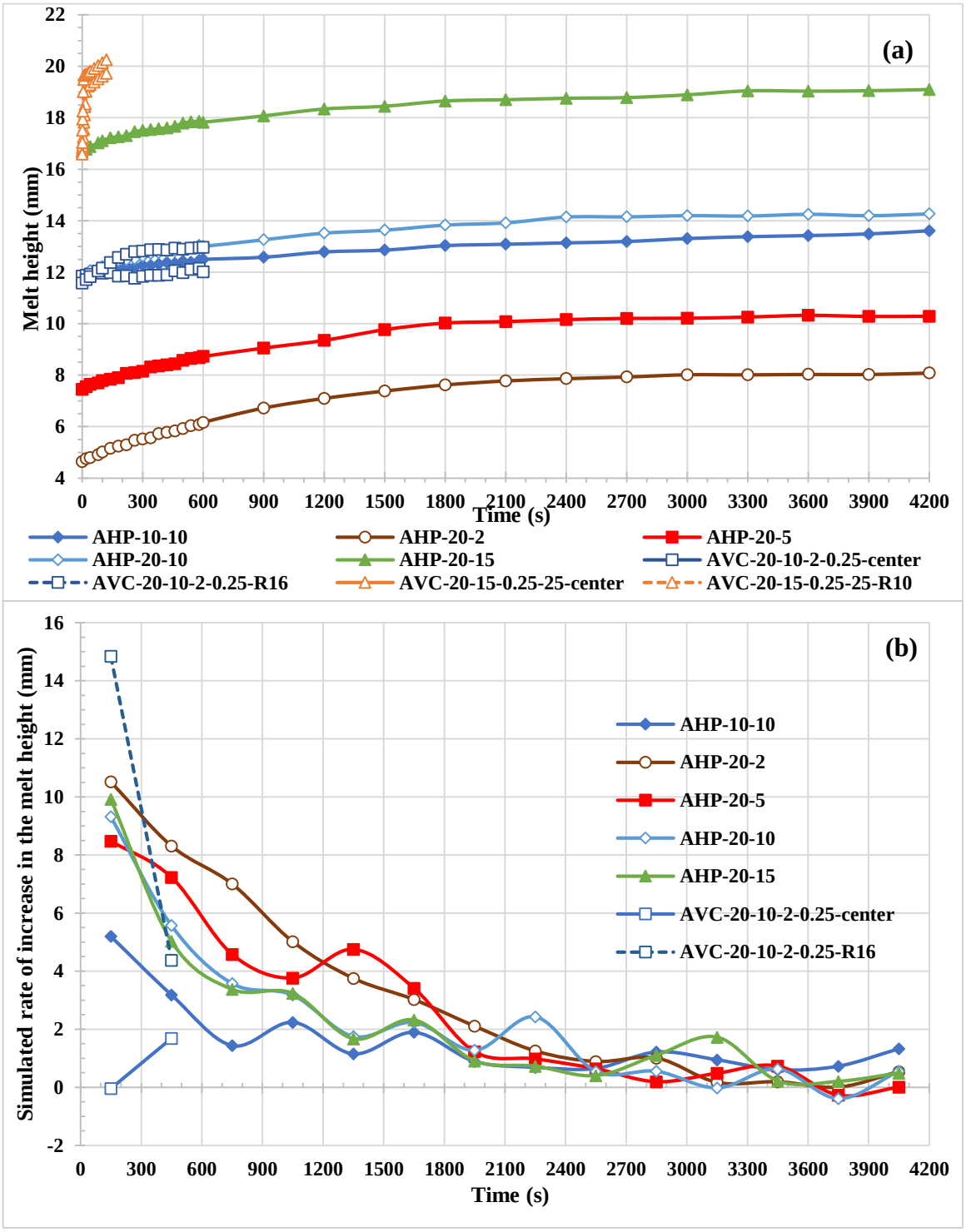

Figure 5.10. The melt height during the solidification process (a). Simulated rate of increase in the melt height (b).

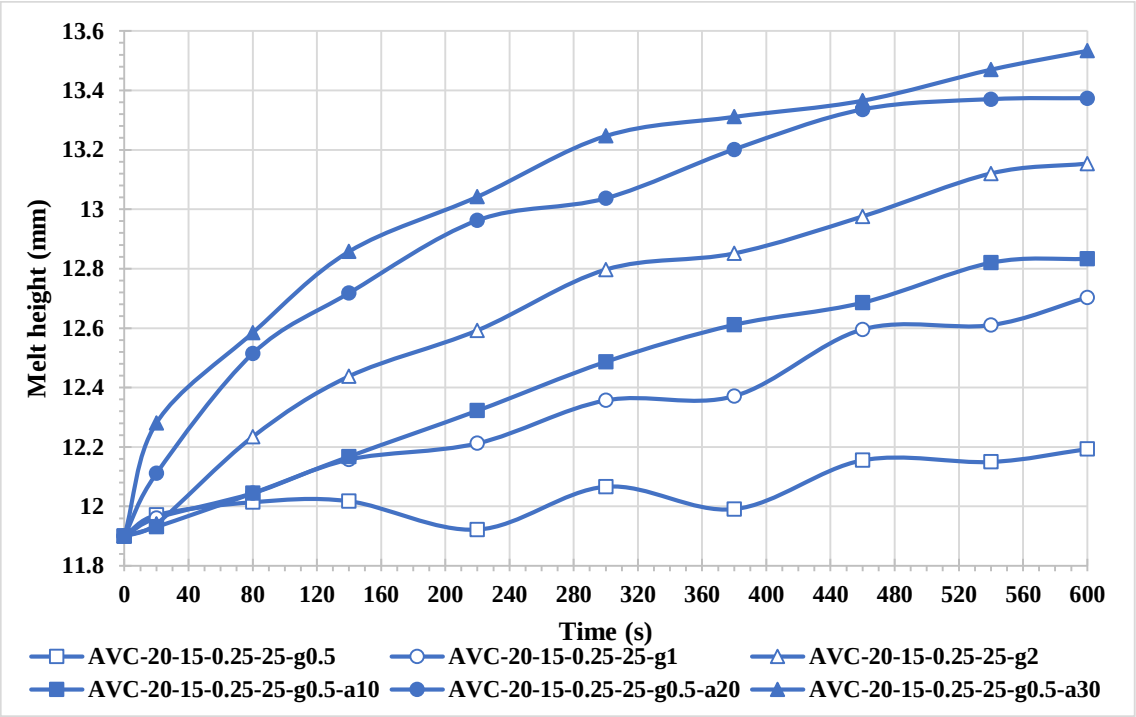

Figure 5.11. The melt height during the solidification process of AVC simulated cases with modified baffle shape.

Figure 5.10b shows that for a constant pulling velocity, the eventual change in the melt height (h_r) is smaller for larger initial melt heights. For a consistent melt height of 10 mm, AVC-20-10-2-0.25-center shows the least change in the melt height, AHP-10-10 follows it, and AHP-20-10 shows the greatest change. This reflect itself in the form of striations. Faint striations can be observed in AVC-20-10-2-0.25 and sharp ones in the other crystals [181] in Figure 5.1.

Figure 5.11 which shows the melt height (measured from the center of the interface to the center of the baffle at the middle-up position) from the beginning to the 600s of growth in AVC cases with modified baffle shape, justifies the results discussed about Figure 5.9.

5.1.6. Vibrational Amplitude (A) and Frequency (f)

Increasing the pulling velocity to raise the growth rate also increases the radial temperature gradient and the concavity of the s/l interface which, in turn, increases the solute segregation [181]. However, uniform convective mixing can decrease the solute segregation

and lead to a more uniform concentration in the solid[90]. The AVC method is used to better stir the melt near the s/l interface. A properly selected amplitude and frequency of the vibration can provide controlled melt flow and redistribute the solute homogeneously.

In contrast to the AHP method, in the AVC method there is a melt mixing between the regions below and above the baffle [98,100]. There is a melt flow up and down through the annular gap with the vibration of the baffle. This flow, in contrast to that for the AHP method, generates a forced vortex attached to the baffle base which then can induce a vortex in the melt below the baffle. The simulations show that the maximum velocity magnitude of the downward flow in the annular gap in the AVC-20-10-2-0.25 in the upward motion of the baffle is 81.22 mm/s. This value is 786.7 mm/s for the AVC-20-15-0.25-25. Recalling that this value is maximum 0.15 mm/s in the AHP cases, the downward annular flow in the AVC cases will clearly have a significant effect on the melt flow below the baffle. This high velocity annular flow is a result of a high baffle to crucible relative velocity, which is 2 mm/s (7200 mm/h) in the AVC-20-10-2-0.25 and 25 mm/s (9×10^4 mm/h) in the AVC-20-15-0.25-25. This relative velocity in the AHP cases is maximum 20 mm/h. In addition, it is clear that in the AVC cases, the velocity magnitude in the annular gap depends on the vibrational parameters rather than the pulling velocity and the melt height.

The vibrational vortices under the baffle are characterized by the vibrational Reynolds number [20], defined as:

$$Re_v = 2\pi f r A/v \tag{5.1}$$

where f is the vibrational frequency in Hertz, A is the vibrational amplitude, r is the radius of the baffle, and v is the kinetic viscosity of the melt. A higher vibrational Reynolds number corresponds to a stronger convective cell in the space between the baffle and the s/l interface. Thus, a high amplitude, A, and a high frequency, f, are preferred. However, according to the vibration intensity [102] ($I = A \times f^2$), the effect of the frequency is more than that of the amplitude. The value of this parameter (I) for the cases used in this study is given in Table 4.1, which indicates that the flow intensity in the AVC-20-15-0.25-25 is much greater than that in the AVC-20-10-2-0.25.

In the AVC method, a variation in the vibrational amplitude and frequency generates different types of forced convection cells. Even for the same set of vibrational parameters, the flow cell shape and strength vary with baffle position in the oscillation cycle which is comprised of the top, middle-down, bottom, and middle-up. For example, the strongest cell in the AVC-20-10-2-0.25 is generated after 601s at the top of the cycle with a maximum velocity of 24 mm/s. Although the size and the velocity magnitude of this cell during the vibration changes, its counterclockwise direction persists. Figure 5.12 shows the velocity magnitude in the AVC-20-10-2-0.25 at a line 8.3 mm above the seed base after 601s at the top, 602s at the middle-down, 603s at the bottom, and 604s at the middle-up position. Since the velocity is measured at a fixed axial position, the two peaks of the top position are related to the velocity of the sides of the cell and implies that at the top position, the forced convective cell is closer to the interface than the other ones. This can be seen in Figure 4.9, as well.

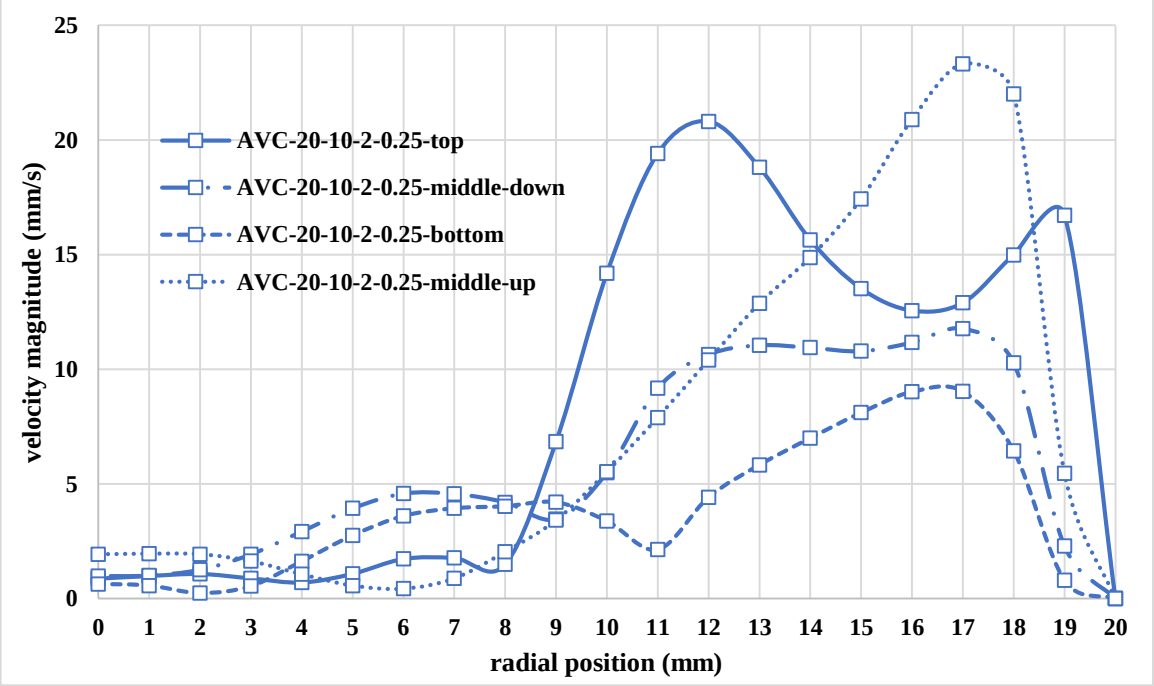

Figure 5.12. Velocity magnitude in the AVC-20-10-2-0.25 at 8.3 millimeter above the seed base after 597s at the top, 598s at the middle-down, 599s at the bottom, and 600s at the middle-up positions.

Vibration with a high amplitude and a low frequency mixes the melt moderately, avoids high vibrational intensity, and provides a flatter interface with more homogeneous solute redistribution [181]. In fact, two side-by-side convective cells in opposite direction at the middle-down and the bottom positions contribute to a more homogeneous solute distribution according to the experimental results.

Very high frequency vibrational motion brings the hot liquid via the annular gap close to the interface, increasing the concavity and solute segregation [181]. Figure 4.12 demonstrates that the flow induced above the interface in different cycle stages does not change and has a constant form and trend. The velocity magnitude for this induced flow is also almost invariant with the baffle position in the oscillation cycle, unlike in the previous AVC crystal that is shown in Figure 5.12.

Simulations demonstrate that the vibration with low amplitude and high frequency generates a uniform constant induced convective cell which covers the entire melt domain under the baffle. Experimental results show though that in this case, the length of the single crystal is about a half that of the other AVC sample with high amplitude and low frequency. On the contrary, the AVC with high amplitude and low frequency generates a moderate convective cell near the crucible wall accompanied by a second cell at two cycle positions. This creates a good melt mixing in the region below the baffle.

By controlling the forced convective flow with an appropriate amplitude and frequency, a single crystal length close to that in AHP-10-10 can be achieved in AVC-20-10-2-0.25 even while doubling the pulling rate, Figure 5.1. That is an appropriate choice of the vibrational parameters can improve crystal quality by suppressing or modifying the buoyancy and forced flow. Comparison of Figures 4.9 and 4.12 shows that with higher frequency, the forced flow vortices become smaller and move away from the interface toward the baffle base. Further experimental and simulation efforts could test the effect of varies frequency and amplitude couples on the induced flow above the interface. Since the smaller forced flow vortices are expected to be distant from the interface, their adverse effect on the interface morphology is expected to vanish. Still, the dimensionally small forced flow vortices can induce a flow above the interface that may mix the melt more uniformly.

5.2. Axial and Radial Solute Distribution

By reducing the melt height with the immersed baffle in the AHP and AVC methods, the convective cells created by the buoyancy and the flow through the annular gap between the crucible and the baffle are squeezed vertically and elongated parallel to the interface. This provides more effective mixing in the melt which delays selective solute accumulation at the center of the crystal. Therefore, as shown in the longitudinal solute distribution plots in the results section, the solute concentration at the center lies between the complete mixing and diffusional mixing for all the crystals except for the VB-20-58. Furthermore, in the AHP growth, at the low melt height (AHP-20-5), due to reduced effective bulk melt volume below the baffle, the crystal solidifies with a higher solute content; compare the radial solute distribution in AHP-20-5 and AHP-20-15. The solute incorporation in the solid is normally greater with increased solidification velocity. Therefore, AHP-20-15 is expected to have a greater solute content than AHP-10-10, but because of a lower melt height in the latter, its concentration is approximately equal to the former. A similar consequence is seen in the radial segregation plots of these samples in Figure 5.13. This outcome is not observed for the other crystals (VB or AVC), probably because of a more rigorous melt flow in them. Also, the average radial solute segregation plots along the crystals given in Figure 5.13 show that the radial solute segregation is less in the crystals grown with a lower melt height, and the value of the segregation remains the same along the crystal. This shows that reducing the melt height provides both radial and axial homogeneity in the grown crystals.

The flow behavior in the melt above the s/l interface is very influential in the solute redistribution, as discussed above, and in the single crystal length of a grown crystal. The melt can experience mixing due to a buoyancy-driven convection from temperature and solute gradients in the melt. A stabilizing, positive axial temperature gradient is applied during the growth of the crystals. In addition, since the density of the solute (Sb) is higher than the solvent (Ge) in the Sb-doped Ge crystals, the solute does not float, so the system is solutally stable. Thus, the convection in the melt should arise from the radial temperature gradients. Although the graphite baffle inside the melt did not contain a heater, because of its high thermal conductivity, an axial heat flux is produced close to the interface however, lower side temperature leads to a greater radial temperature gradient as explained in Results. Figure 5.1 show that insertion of the baffle significantly enhances the achieved single crystal

length in the grown crystals. Therefore, the breakdown of the interface occurs earlier in the VB20-58 crystal compared to the other crystals grown in this study. When the melt height is reduced to 15 mm (AHP-20-15), the single crystal length increases to 30.6 mm. A further reduction of the melt height to 5 mm (AHP-20-5) increases the single crystal length to 35 mm. A similar trend is seen for the AVC crystals, although obscured by the vibration effect. Hence, although the radial temperature gradient increases with a reduced melt height, it causes better mixing and more uniform solute distribution in the solid.

The uniformity of the solute redistribution in both the radial and axial directions is an important object in the single crystal growth of semiconductors. During solidification, the solute Sb in the solvent Ge is rejected to the interface due to the segregation coefficient (K) which is less than one (k = 0.003) [90]. The rejected solute at the interface can either be distributed in the melt homogeneously by completely mixing (CM) the melt (Scheil model) or collected in front of the s/l interface and leads to a boundary layer formation (diffusional mixing, DM [120]). In the presence of convective flow the solute will be partially mixed in the liquid. The solute distribution along the solidified crystals is collected by the four-point-probe technique and presented in the previous section. The radially averaged solute segregation for the grown crystals along the length is calculated as $(C_{max} - C_{min})/C_{av}$ and plotted in Figure 5.13, where C_{max}, C_{min}, and C_{av} are respectively the maximum, minimum, and average solute concentration in a radial plane.

The buoyancy driven thermal convection in the melt redistributes the rejected solute from the solidifying interface into the bulk fluid. However, this convection does not effectively mix the melt to redistribute the solute homogeneously. As shown by the longitudinal solute distributions in Results, while the axial solute redistribution for the VB-20-58 crystal at the center is close to that of diffusional mixing, the solute concentrations at the sides are between the Scheil and VB-DM curves. This shows diffusional mixing at the center and partial mixing at the sides due to creation of a convective cell at each side that do not disturb the center appreciably.

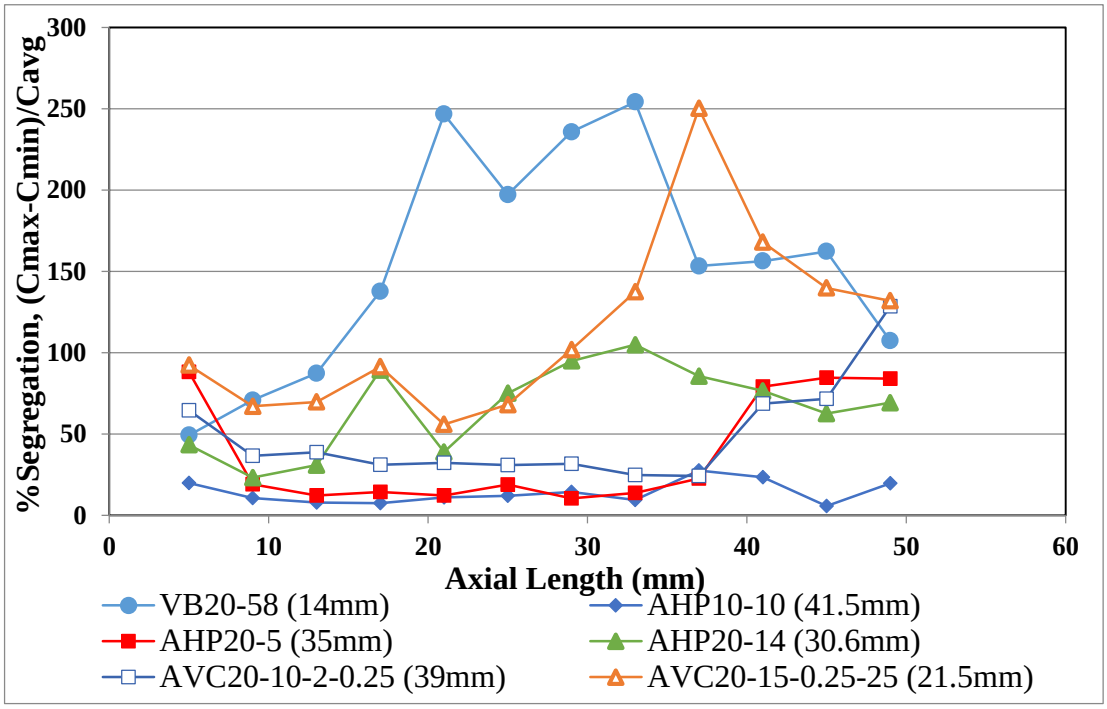

Figure 5.13. Averaged radial solute segregation along the crystals. The values in the parentheses are the single crystal lengths.

It is also shown in Figure 4.1d that the solute concentration in VB-20-58 is progressively higher at the center as solidification continues. Due to a weak convection at the center, solute accumulates in the vicinity of the interface and the melt solidifies with a higher solute content. Figure 5.13 also shows that the lowest segregation is observed in AHP-10-10 and AHP-20-5. These two crystals very nicely illustrate the importance of growth parameters and a positive role of the baffle in single crystal quality. AHP-20-5 is pulled with a velocity twice that of AHP-10-10. Thus, production efficiency is increased while the crystal quality is the same.

5.3. Interface Shape and Stability

The striation has been mentioned before as a marker of the interface. Actually, it is a type of crystal defect which is often observed in melt-grown crystals because of oscillations in the temperature and/or in the composition field at the interface. Thus, the sudden temperature and concentration variations, the melt convection, or the melt-back can yield these intrinsic crystal defects. Several approaches have been adopted to suppress the striations by sustaining a constant segregation coefficient, interface velocity, and solute

boundary layer during the solidification.[189] Crystal growth in the microgravity, magnetic fields, and reduced melt height solidifications have aimed at decreasing the convection, yet mixing the melt can homogenize the solute field and thermal field. Indeed, a controlled mixing can push the segregation coefficient toward unity that can suppress the striations [189]. Presence of the faint striations in the AVC-20-10-2-0.25 sample indicates that mixing in this sample by the axially vibrating baffle results in a uniform solute distribution in front of the interface and hence prevents sudden changes in the interface velocity. In contrast, when the mixing is severe as in the other two AVC crystals, a melt-back and regrowth take place repeatedly yielding sudden changes in the interface velocity. Moreover, the striations in the AHP samples are more visible than those in the AVC20-10-2-0.25 but less than those in the high frequency AVC samples. This indicates that the convection in a reduced melt height is still significant to cause the oscillations, but a properly adjusted axial vibration can provide a better solute uniformity to yield a constant interface growth rate.

Figure 5.14 shows the simulated interface shapes at different times from the start of the pulling. The vertical scales are equal in all cases, and only the radial profile of the interface is shown. The vertical line at the left side is the crucible wall. The crucible is initially positioned within the axial temperature gradient to obtain the interface 5 mm above the seed base. However, because of the varying strength of the convective cells in the crystals even before pulling (Figure 5.2), different seed heights in the center result. The simulated interface profiles are reasonably close to the experimental ones in the initial growth period as seen in Figure 5.1 and explained in the results section. However, the simulated results do not match the experimental ones in later times. The real interface shape is shown by the striations in real crystal photos in Figure 5.1. The current simulations provide a general idea about flow pattern during solidification of studied crystals. Furthermore, in the AVC-20-15-0.25-25 simulation, an intense flow created by the high vibration frequency melts back the seed leaving a very thin seed layer. This issue is not observed in the corresponding experiment because the cooling system chills the bottom of the seed, and this cooling is neglected in the simulations. The intense vibrational flow also creates deep concavity at the sides of the AVC-20-10-2-0.25.

Comparison of the single crystal lengths in Figure 5.1 shows that a decrease in the effective melt height results in an increase in the single crystal length in the grown crystals.

The single crystal length of VB-20-58 is the lowest owing to its greatest melt height. AHP-20-15 and AHP-20-5 show the same trend for a constant pulling velocity. The AVC crystals have a reduced melt height and a greater single crystal length than the VB crystal, though the comparison is complicated by varying vibration parameters. The enhanced stability (single crystal length) is of course a result of uniform solute distribution and prevention of the melt undercooling during solidification with a baffle.

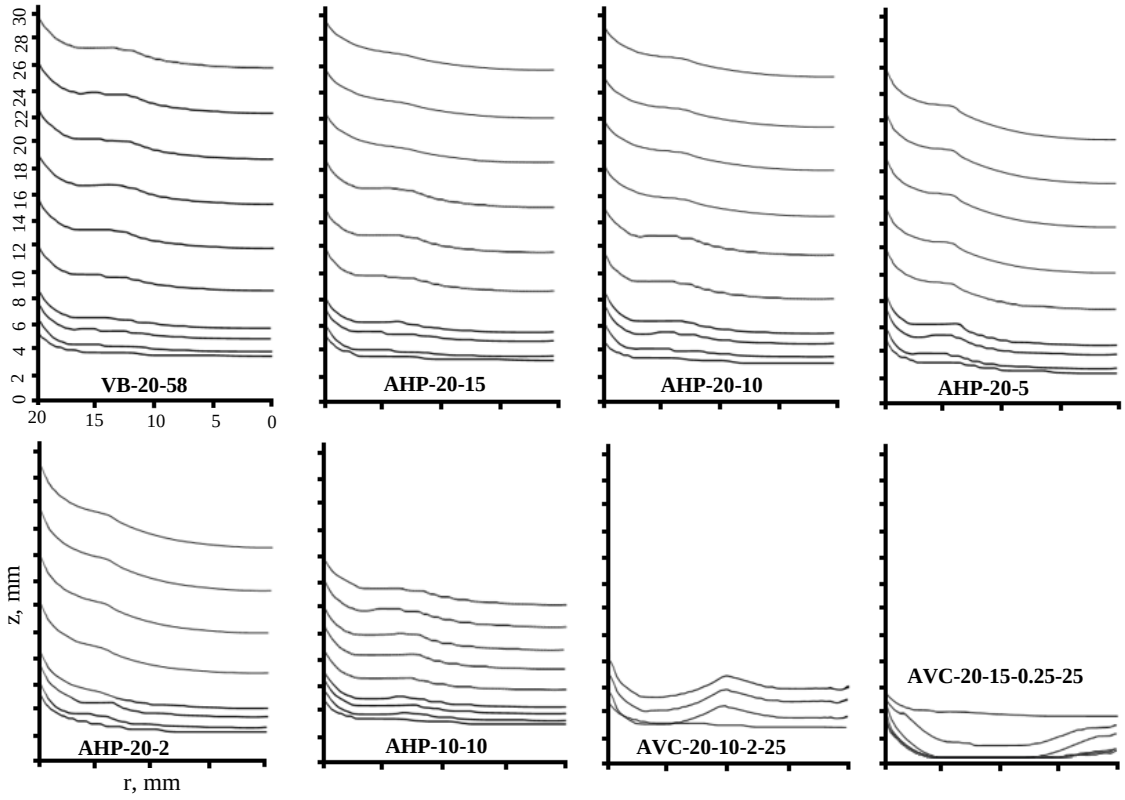

Figure 5.14. The interface shape at different times during the solidification process in all the simulations. The lines shown in each sample (bottom-up) represent the interface position respectively at 0, 180, 420, 600, 1200, 1800, 2400, 3000, 3600, and 4200 seconds. In the AVC-20-15-0.25-25, the shown lines (top-down) represent the interface position respectively at 0, 5, 10, 20, 30, and 120 seconds. In this sample interfaces at 30 and 120 are overlapped, thus there are four visible lines.

6. CONCLUSIONS

Numerical simulations have been performed to characterize the flow in the melt of crystals grown by the VB, AHP, and AVC methods. The implications of the flow on the temperature distribution, the interface shape, the solute distribution, and the single crystal quality have been analyzed. By the AHP method, the effect of the melt height on the convective flow above the s/l interface has been investigated. Experimental results show that decreasing the melt height generally increases the single crystal length. Simulations further reveal that a lower melt height increases the radial temperature gradient in the melt which generates a better mixing near the interface. It is also determined that the real interface growth velocity deviate more from the pull velocity with lower melt heights.

While a radial temperature gradient in the VB method leads to high solute segregation, an immersed baffle with high thermal conductivity in the melt can decrease the melt height effectively and reduce the solute segregation. In addition, a gentle mixing of the melt by an axial vibration of the baffle homogenizes the solute concentration and provides more flat interface at the center of the crystal. Therefore, an improved single crystal length has been obtained by a reduced melt height (AHP) and appropriately adjusted axial vibration in the melt (AVC). Furthermore, the AVC makes it possible to increase the growth rate and achieve almost the same single crystal quality that is normally obtained with the lower pulling velocities in the other growth methods.

Applying an axial vibration to the baffle in the AVC method gives two more parameters to adjust the flow characteristics. Specifically, the melt can be more thoroughly mixed near the s/l interface to achieve a uniform solute distribution by appropriately adjusting the amplitude and frequency of the vibration. In contrast to the AHP method, the AVC method has a high velocity melt flow through the annular gap between the baffle and the crucible generating a forced flow. The flow cell shape and strength vary with baffle position throughout the vibration cycle for a given set of vibrational parameters. Increasing the amplitude and frequency of vibration increases the strength of the forced flow. Vibration with a high amplitude and a low frequency generates a more moderate flow, and is observed

in this study to result in a more homogeneous solute redistribution. Although vibrational motion with a high frequency generates a uniform constant convective flow and covers the entire melt domain under the baffle, the hot liquid from the annular gap is driven close to the interface, and increases the concavity and solute segregation. In addition to vibration amplitude and frequency, shape modifications to the baffle do modify melt flow pattern. This also provides means to control melt flow to produce high quality crystals.

7. FUTURE WORK

This research can be continued to have a better prediction on the s/l interface shape and dopant segregation in addition to the convective flow and its effect in different configurations of the AHP and AVC methods with various melt heights and amplitudes and frequencies of vibration. Several different baffle shapes can be examined and analyzed to grow crystals with larger diameters while increasing the crystal quality.

In AHP cases making a cavity below the baffle can decrease the axial heat flux from the high conductivity baffle through the center of the s/l interface and effectively help to have a more planar and accordingly a more uniform dopant distribution in radial direction.

Making axial holes in the baffle with different sizes in high amplitude and low frequency AVC case to let the hot melt passes from the top region of the baffle through the s/l interface to mix the melt uniformly can be an effective way to increase the quality of the crystals with much larger diameters.

REFERENCES

1. Depuydt, B., M. De Jonghe, W. De Baets, I. Romandic, A. Theuwis, C. Quaeyhaegens, C. Deguet, T. Akatsu, and F. Letertre, *Germanium Materials*, in *Germanium-based technologies: from materials to devices*, Elsevier, Amsterdam, 2007.

2. Yurasov, D., A. Antonov, M. Drozdov, V. Schmagin, K. Spirin, and A. Novikov, "Antimony segregation in Ge and formation of n-type selectively doped Ge films in molecular beam epitaxy", *Journal of Applied Physics*, Vol. 118, pp. 145701, 2015.

3. Olesinski, R. and G. Abbaschian, "The Ge− Sb (Germanium-Antimony) system", *Journal of Phase Equilibria*, Vol. 7, pp. 219, 1986.

4. Greenberg, J., *Experimental Data on P-T-X Phase Diagrams and Non)stoichiometry* in *Thermodynamic Basic of Crystal Growth*, Springer-Verlag, Berlin Heidelberg, 2002.

5. Emsley, J., *Nature's Building Blocks: An Az of the Elements*, Oxford University Press, 2001.

6. Depuydt, B., A. Theuwis, and I. Romandic, "Germanium: from the first application of Czochralski crystal growth to large diameter dislocation-free wafers", *Materials Science in Semiconductor Processing*, Vol. 9, pp. 437, 2006.

7. *Workshop on Germanium for CMOS*, in *SiGe and Ge: Materials, Processing, and Devices*, The Electrochemical Society (ECS), USA, 2006.

8. Jorgenson, J. D., *Germanium recycling in the United States in 2000*, US Department of the Interior, US Geological Survey, 2006.

9. Chen, J., D. Yang, X. Ma, Z. Zeng, D. Tian, L. Li, D. Que, and L. Gong, "Influence of germanium doping on the mechanical strength of Czochralski silicon wafers", *Journal of Applied Physics*, Vol. 103, pp. 123521, 2008.

10. Czochralski, J., "Ein neues verfahren zur messung der kristallisationsgeschwindigheit der metalle", *Z. phys. Chemie.*, Vol. 92, pp. 219, 1918.

11. Pfann, W. G. and H. C. Theuerer, "*Semiconductor translating device*", Google Patents, 1955.

12. Terashima, K. and T. Fukuda, "A new magnetic-field applied pulling apparatus for LEC GaAs single crystal growth", *Journal of Crystal Growth*, Vol. 63, pp. 423, 1983.

13. Bridgman, P., "Crystal growth apparatus", *Proc. Am. Acad. Arts Sci*, 1925.

14. Chang, C. E. and W. R. Wilcox, "Control of interface shape in the vertical Bridgman-Stockbarger technique", *Journal of Crystal Growth*, Vol. 21, pp. 135, 1974.

15. Sen, S. and W. R. Wilcox, "Influence of crucible on interface shape, position and sensitivity in the vertical Bridgman-Stockbarger technique", *Journal of Crystal Growth*, Vol. 28, pp. 36, 1975.

16. Meyer, S. and A. G. Ostrogorsky, "Interface shape in the vertical Bridgman configuration with and without the submerged heater", *Journal of Crystal Growth*, Vol. 166, pp. 700, 1996.

17. Zharikov, E., L. Prihod'ko, and N. Storozhev, "Fluid flow formation resulting from forced vibration of a growing crystal", *Journal of Crystal Growth*, Vol. 99, pp. 910, 1990.

18. Fedyushkin, A., N. Bourago, V. Polezhaev, and E. Zharikov, "The influence of vibration on hydrodynamics and heat-mass transfer during crystal growth", *Journal of Crystal Growth*, Vol. 275, pp. e1557, 2005.

19. Avetissov, I., A. Sadovskiy, S. Belov, A. Khomyakov, K. Rekunov, V. Kostikov, and E. Sukhanova, "Thermodynamic features of axial vibrational control technique for crystal growth from the melt", *CrystEngComm*, Vol. 15, pp. 2213, 2013.

20. Zharikov, E. V., *Advanced Technologies of Crystal Growth from Melt Using Vibrational Influence*, in *Crystal Growth Technology: Semiconductors and Dielectrics*, Wiley-VCH Verlag Weinheim 2010.

21. Deal, A., E. Balikci, and R. Abbaschian, "Enhanced morphological stability in Sb-doped Ge", *Metallurgical and Materials Transactions A*, Vol. 38, pp. 100, 2007.

22. Rogers, P. and J. Williamson, "*Devitrified glass with fibrous crystals in parallel relationship*", Google Patents, 1974.

23. Gianoulakis, S. E. and R. Sparrow, "*Crystal growth and annealing method and apparatus*", Google Patents, 2001.

24. Tamura, M., M. Ohkura, M. Miyao, N. Natsuaki, N. Yoshihiro, T. Tokuyama, and H. Ishihara, "*Method of producing single crystal film utilizing a two-step heat treatment*", Google Patents, 1986.

25. Wang, F. E., A. M. Syeles, W. L. Clark, and W. J. Buehler, "Growth of TiNi Single Crystals by a Modified``Strain-Anneal"Technique*", Journal of Applied Physics*, Vol. 35, pp. 3620, 1964.

26. Zhang, H. and J. F. Banfield, "Understanding polymorphic phase transformation behavior during growth of nanocrystalline aggregates: insights from TiO2*", The Journal of Physical Chemistry B*, Vol. 104, pp. 3481, 2000.

27. Heuer, A., V. Lanteri, and A. Dominguez-Rodriguez, "High-temperature precipitation hardening of Y 2 O 3 partially-stabilized ZrO 2 (Y-PSZ) single crystals*", Acta metallurgica*, Vol. 37, pp. 559, 1989.

28. Dhanaraj, G., K. Byrappa, V. V. Prasad, and M. Dudley, *Crystal Growth Techniques and Characterization: An Overview*, in *Springer Handbook of Crystal Growth*, Springer, 2010.

29. Aidong, J., C. Fen, L. Qi, C. Zusheng, and Z. Yong, "Flux growth of large single crystals of low temperature phase barium metaborate*", Journal of Crystal Growth*, Vol. 79, pp. 963, 1986.

30. Adachi, H., T. Watanabe, M. Yoshimura, Y. Mori, and T. Sasaki, "Growth of protein crystal at interface between two liquids using slow cooling method*", Japanese Journal of Applied Physics*, Vol. 41, pp. L726, 2002.

31. Mlavsky, A. and M. Weinstein, "Crystal Growth of GaAs from Ga by a Traveling Solvent Method*", Journal of Applied Physics*, Vol. 34, pp. 2885, 1963.

32. Revcolevschi, A., U. Ammerahl, and G. Dhalenne, "Crystal growth of pure and substituted low-dimensionality cuprates CuGeO 3, La 2 CuO 4, SrCuO 2, Sr 2 CuO 3 and Sr 14 Cu 24 O 41 by the floating zone and travelling solvent zone methods", *Journal of Crystal Growth*, Vol. 198, pp. 593, 1999.

33. Majchrowski, A., M. Borowiec, and E. Michalski, "Top seeded solution growth of KHo (WO 4) 2 single crystals", *Journal of Crystal Growth*, Vol. 264, pp. 201, 2004.

34. Polgár, K., A. Peter, L. Kovács, G. Corradi, and Z. Szaller, "Growth of stoichiometric LiNbO 3 single crystals by top seeded solution growth method", *Journal of Crystal Growth*, Vol. 177, pp. 211, 1997.

35. Hosaka, M. and S. Taki, "Hydrothermal growth of quartz crystals in NaCl solution", *Journal of Crystal Growth*, Vol. 52, pp. 837, 1981.

36. Sekiguchi, T., S. Miyashita, K. Obara, T. Shishido, and N. Sakagami, "Hydrothermal growth of ZnO single crystals and their optical characterization", *Journal of Crystal Growth*, Vol. 214, pp. 72, 2000.

37. Ehrentraut, D., H. Sato, Y. Kagamitani, H. Sato, A. Yoshikawa, and T. Fukuda, "Solvothermal growth of ZnO", *Progress in crystal growth and characterization of materials*, Vol. 52, pp. 280, 2006.

38. Ahsanulhaq, Q., A. Umar, and Y. Hahn, "Growth of aligned ZnO nanorods and nanopencils on ZnO/Si in aqueous solution: growth mechanism and structural and optical properties", *Nanotechnology*, Vol. 18, pp. 115603, 2007.

39. James, J. and R. Kell, "*Crystal growth from aqueous solutions*", Pergamon Press, London. pp. 557, 1975.

40. Dario, A., H. O. Sicim, and E. Balikci, "Germanium–silicon single crystal growth by the axial heat processing (AHP) technique", *Journal of Crystal Growth*, Vol. 318, pp. 1057, 2011.

41. Hobgood, H., B. Swanson, and R. Thomas, "Czochralski growth of CdTe and CdMnTe from liquid encapsulated melts", *Journal of Crystal Growth*, Vol. 85, pp. 510, 1987.

42. Bonner, W. and L. Van Uitert, "Growth of single crystals of Pb 3 MgNb 2 O 9 by the Kyropoulos technique", *Materials Research Bulletin*, Vol. 2, pp. 131, 1967.

43. Mochizuki, S., F. Fujishiro, and S. Minami, "Photoluminescence and reversible photo-induced spectral change of SrTiO3", *Journal of Physics: Condensed Matter*, Vol. 17, pp. 923, 2005.

44. Takagi, M., K. Takasaki, and K. Koyama, "*Vapor phase growth method*", Google Patents, 1985.

45. Hanna, M., Z. Lu, and A. Majerfeld, "Very high carbon incorporation in metalorganic vapor phase epitaxy of heavily doped p-type GaAs", *Applied physics letters*, Vol. 58, pp. 164, 1991.

46. Noborisaka, J., J. Motohisa, S. Hara, and T. Fukui, "Fabrication and characterization of freestanding GaAs/AlGaAs core-shell nanowires and AlGaAs nanotubes by using selective-area metalorganic vapor phase epitaxy", *Applied physics letters*, Vol. 87, 2005.

47. Ponchet, A., A. Rocher, A. Ougazzaden, and A. Mircea, "Self-induced laterally modulated GaInP/InAsP structure grown by metal-organic vapor-phase epitaxy", *Journal of Applied Physics*, Vol. 75, pp. 7881, 1994.

48. Hu, J., X. Xu, J. Stotz, S. Watkins, A. Curzon, M. Thewalt, N. Matine, and C. Bolognesi, "Type II photoluminescence and conduction band offsets of GaAsSb/InGaAs and GaAsSb/InP heterostructures grown by metalorganic vapor phase epitaxy", *Applied physics letters*, Vol. 73, pp. 2799, 1998.

49. Li, X., M.-W. Lin, A. A. Puretzky, J. C. Idrobo, C. Ma, M. Chi, M. Yoon, C. M. Rouleau, I. I. Kravchenko, and D. B. Geohegan, "Controlled vapor phase growth of single crystalline, two-dimensional GaSe crystals with high photoresponse", *Scientific reports*, Vol. 4, 2014.

50. T. Nishinaga and S. Naritsuka, *Epitaxial Growth of III-V Compounds*, in *Crystal Growth Technology*, William Andrew Inc., Norwich, New York, 2003.

51. Verneuil, A., "Production artificielle du rubis par fusion", *Paris Acad. Sci., Comptes Rendus*, Vol. 135, pp. 791, 1902.

52. Wikipedia, "Verneuil process ", 2016, https://en.wikipedia.org/wiki/Verneuil_process, June 2016

53. Hoshikawa, K., "Czochralski silicon crystal growth in the vertical magnetic field", *Japanese Journal of Applied Physics*, Vol. 21, pp. L545, 1982.

54. Kakimoto, K., M. Eguchi, H. Watanabe, and T. Hibiya, "Natural and forced convection of molten silicon during Czochralski single crystal growth", *Journal of Crystal Growth*, Vol. 94, pp. 412, 1989.

55. Sadamitsu, S., S. Umeno, Y. Koike, M. Hourai, S. Sumita, and T. Shigematsu, "Dependence of the grown-in defect distribution on growth rates in Czochralski silicon", *Japanese Journal of Applied Physics*, Vol. 32, pp. 3675, 1993.

56. Matsui, A., I. Yonenaga, and K. Sumino, "Czochralski growth of bulk crystals of Ge 1-x Si x alloys", *Journal of Crystal Growth*, Vol. 183, pp. 109, 1998.

57. Yonenaga, I., "Czochralski growth of GeSi bulk alloy crystals", *Journal of Crystal Growth*, Vol. 198, pp. 404, 1999.

58. Hattendorf, J., W.-D. Zeitz, N. Abrosimov, and W. Schröder, "The interstitial boron and the boron–germanium complex in silicon–germanium crystals", *Physica B: Condensed Matter*, Vol. 308, pp. 535, 2001.

59. Li, F., S. Pan, X. Hou, and Z. Zhou, "Growth of Bi 2 ZnOB 2 O 6 crystal by the Czochralski method", *Journal of Crystal Growth*, Vol. 312, pp. 2383, 2010.

60. Banerjee, J. and K. Muralidhar, "Role of internal radiation during Czochralski growth of YAG and Nd: YAG crystals", *International journal of thermal sciences*, Vol. 45, pp. 151, 2006.

61. Nawash, J. M. and K. G. Lynn, "Czochralski crystal growth of Zn 2 Te 3 O 8", *Journal of Crystal Growth*, Vol. 310, pp. 4217, 2008.

62. Spiro, K., "*Process of coating iron and iron alloys with chromium*", Google Patents, 1926.

63. Meroli, S., "Czochralski vs Float Zone: growing mono-crystalline silicon", 2012, http://meroli.web.cern.ch/meroli/Lecture_silicon_floatzone_czochralski.html, June 2016

64. Delbeco, C., W. Hayes, and P. Yuster, "Absorption Spectra of F 2−, Cl 2−, Br 2−, and I 2− in the Alkali Halides", *Physical Review*, Vol. 121, pp. 1043, 1961.

65. Patterson, D. A., "Controlled atmosphere kyropoulos growth of alkali halide single crystals", *Review of Scientific Instruments*, Vol. 33, pp. 831, 1962.

66. RMD, R. M. D., Inc., "Kyropoulos ", 2016, http://rmdinc.com/kyropoulos/, June 2016.

67. Pfann, W. G., "Principles of zone-melting", *Trans. AiME*, Vol. 194, pp. 747, 1952.

68. Motohira, N., K. Kuwahara, T. Hasegawa, K. Kishio, and K. Kitazawa, "Single Crystal Growth of Bi sub 2 Sr sub 2 Ca sub n--1 Cu sub n O sub y Superconductors by the Floating Zone Method", *Nippon Seramikkusu Kyokai Gakujutsu Ronbunshi(J. Ceram. Soc. Jpn.)*, Vol. 97, pp. 1009, 1989.

69. Kimura, S. and I. Shindo, "Single crystal growth of YIG by the floating zone method", *Journal of Crystal Growth*, Vol. 41, pp. 192, 1977.

70. Takekawa, S., H. Nozaki, A. Umezono, K. Kosuda, and M. Kobayashi, "Single crystal growth of the superconductor Bi 2.0 (Bi 0.2 Sr 1.8 Ca 1.0) Cu 2.0 O 8", *Journal of Crystal Growth*, Vol. 92, pp. 687, 1988.

71. Takeya, H., T. Hirano, and K. Kadowaki, "Single crystal growth of quaternary superconductor YNi 2 B 2 C by a floating zone method", *Physica C: Superconductivity*, Vol. 256, pp. 220, 1996.

72. Lal, K. and G. Bhagavannarayana, "A high-resolution diffuse X-ray scattering study of defects in dislocation-free silicon crystals grown by the float-zone method and comparison with Czochralski-grown crystals", *Journal of Applied Crystallography*, Vol. 22, pp. 209, 1989.

73. Campbell, T., M. Schweizer, P. Dold, A. Cröll, and K. Benz, "Float zone growth and characterization of Ge 1− x Si x (x⩽ 10at%) single crystals", *Journal of Crystal Growth*, Vol. 226, pp. 231, 2001.

74. Shonai, T., M. Higuchi, K. Kodaira, T. Ogawa, S. Wada, and H. Machida, "Float zone growth and laser performance of Nd: GdVO 4 single crystals", *Journal of Crystal Growth*, Vol. 241, pp. 159, 2002.

75. PVEducation, "Float Zone Silicon", http://www.pveducation.org/pvcdrom/manufacturing/float-zone-silicon, June 2016.

76. Bridgman, P., "Various Physical Properties of Rubidium and Caesium and the Resistance of Potassium under Pressure", *Proceedings of the American Academy of Arts and Sciences*, JSTOR, 1925.

77. Stockbarger, D. C., "The production of large single crystals of lithium fluoride", *Review of Scientific Instruments*, Vol. 7, pp. 133, 1936.

78. Koai, K., K. Sonnenberg, and H. Wenzl, "Influence of crucible support and radial heating on the interface shape during vertical Bridgman GaAs growth", *Journal of Crystal Growth*, Vol. 137, pp. 59, 1994.

79. Helmers, L., J. Schilz, G. Bähr, and W. Kaysser, "Macrosegregation during Bridgman growth of Ge 1− x Si x mixed crystals", *Journal of Crystal Growth*, Vol. 154, pp. 60, 1995.

80. Chen, H., R. Li, C. Ge, X. Ge, and W. Xu, "Growth of bismuth tellurite crystals by vertical Bridgman method", *Journal of Crystal Growth*, Vol. 281, pp. 303, 2005.

81. Xiao, H., H. Chen, F. Xu, C. Jiang, and P. Yang, "Bridgman growth of CdWO 4 single crystals", *Journal of Crystal Growth*, Vol. 310, pp. 521, 2008.

82. Everson, W., C. Ard, J. Sepich, B. Dean, G. Neugebauer, and H. Schaake, "Etch pit characterization of CdTe and CdZnTe substrates for use in mercury cadmium telluride epitaxy", *Journal of electronic materials*, Vol. 24, pp. 505, 1995.

83. Golyshev, V. and M. Gonik, "*Russian Patent Application 4,810,464, Feb. 15, 1990*", Publication.

84. Ostrogorsky, A., "*Method for directional solidification of single crystals*", Google Patents, 1991.

85. Ostrogorsky, A., "Single-crystal growth by the submerged heater method", *Measurement Science and Technology*, Vol. 1, pp. 463, 1990.

86. Yeckel, A. and J. J. Derby, "Feasibility study of cadmium zinc telluride growth using a submerged heater in a vertical Bridgman system", *Journal of electronic materials*, Vol. 33, pp. 488, 2004.

87. Balikci, E., A. Deal, and R. Abbaschian, "Detached crystal growth from melt by the axial heat processing technique", *Journal of Crystal Growth*, Vol. 271, pp. 37, 2004.

88. Meyer, S. and A. Ostrogorsky, "Forced convection in vertical Bridgman configuration with the submerged heater", *Journal of Crystal Growth*, Vol. 171, pp. 566, 1997.

89. Ostrogorsky, A. G., H. Sell, S. Scharl, and G. Müller, "Convection and segregation during growth of Ge and InSb crystals by the submerged heater method", *Journal of Crystal Growth*, Vol. 128, pp. 201, 1993.

90. Balikci, E., A. Deal, and R. Abbaschian, "Antimony-doped germanium single crystals grown from the melt by the axial heat processing (AHP) technique", *Journal of Crystal Growth*, Vol. 262, pp. 581, 2004.

91. Balikci, E., A. Deal, R. Abbaschian, S. V. Bykova, V. D. Golyshev, M. A. Gonik, V. B. Tsvetovsky, M. P. Marchenko, and I. V. Frjazinov, "A study on the morphological stability of faceted interfaces in antimony-doped germanium single crystals grown by the axial heat processing method", *Crystal growth & design*, Vol. 4, pp. 377, 2004.

92. Bykova, S. V., V. D. Golyshev, M. A. Gonik, V. B. Tsvetovsky, E. Balikci, A. Deal, R. Abbaschian, M. P. Marchenko, I. V. Frjazinov, and V. N. Vlasov, "The experimental–numerical investigation of instability of faceted Ge doped by Sb growth on the base of AHP method", *Journal of Crystal Growth*, Vol. 275, pp. e229, 2005.

93. Marın, C. and A. Ostrogorsky, "Growth of Ga-doped Ge 0.98 Si 0.02 by vertical Bridgman with a baffle", *Journal of Crystal Growth*, Vol. 211, pp. 378, 2000.

94. Golyshev, V., M. Gonik, and V. Tsvetovsky, "Problems of Bi 4 Ge 3 O 12 and Li 2 B 4 O 7 single crystal growth by crusibleless variant of AHP method", *Journal of Crystal Growth*, Vol. 198, pp. 501, 1999.

95. Golyshev, V., M. Gonik, and V. Tsvetovskii, "In situ measurement of interface supercooling during growth of Bi4Ge3O12 single crystals from melt", *Instruments and experimental techniques*, Vol. 41, pp. 735, 1998.

96. Dutta, P. S. and A. G. Ostrogorsky, "Nearly diffusion controlled segregation of tellurium in GaSb", *Journal of Crystal Growth*, Vol. 191, pp. 904, 1998.

97. Dario, A., H. O. Sicim, and E. Balikci, "A comparative study on the growth of germanium–silicon single crystals grown by the vertical Bridgman and axial heat processing techniques", *Journal of Crystal Growth*, Vol. 351, pp. 1, 2012.

98. Dario, A., H. O. Sicim, and E. Balikci, "A new approach for dopant distribution and morphological stability in crystals grown by the axial heat processing (AHP) technique", *Journal of Crystal Growth*, Vol. 337, pp. 65, 2011.

99. Avetisov, I. K., A. Y. Mel'kov, A. Y. Zinov'ev, and E. Zharikov, "Growth of nonstoichiometric PbTe crystals by the vertical Bridgman method using the axial-vibration control technique", *Crystallography Reports*, Vol. 50, pp. S124, 2005.

100. Avetissov, I. C., E. Sukhanova, A. Khomyakov, A. Y. Zinovjev, V. Kostikov, and E. Zharikov, "Simulation and crystal growth of CdTe by axial vibration control technique in Bridgman configuration", *Journal of Crystal Growth*, Vol. 318, pp. 528, 2011.

101. Sadovskiy, A., E. Sukhanova, S. Belov, V. Kostikov, M. Zykova, M. Artyushenko, E. Zharikov, and I. Avetissov, "Axial vibration control of melt structure of sodium nitrate in crystal growth process", *Journal of Crystal Growth*, Vol. 417, pp. 16, 2015.

102. Avetissov, I. C., A. Sadovskiy, E. Sukhanova, G. Y. Orlova, I. Belogorokhov, and E. Zharikov, "Perfection of NaNO 3 single crystals grown by axial vibrational control

technique in Czochralski configuration", *Journal of Crystal Growth*, Vol. 360, pp. 167, 2012.

103. Avetissov, I. C., E. Sukhanova, A. Sadovskii, V. Kostikov, and E. Zharikov, "Experimental and numerical modeling of Czochralski crystal growth under axial vibrational control of the melt", *Journal of Crystal Growth*, Vol. 312, pp. 1429, 2010.

104. Avetissov, I., A. Sadovskiy, S. Belov, C. K. Khan, E. Mozhevitina, E. Sukhanova, and E. Zharikov, "Czochralski growth of NaNO 3–LiNO 3 solid solution single crystals using axial vibrational control technique", *Journal of crystal growth*, Vol. 401, pp. 899, 2014.

105. Shen, X., A. Anilkumar, R. Grugel, and T. Wang, "Utilizing vibration to promote microstructural homogeneity during floating-zone crystal growth processing", *Journal of Crystal Growth*, Vol. 165, pp. 438, 1996.

106. Lyubimova, T., R. Scuridin, A. Cröll, and P. Dold, "Influence of high frequency vibrations on fluid flow and heat transfer in a floating zone", *Crystal Research and Technology*, Vol. 38, pp. 635, 2003.

107. Lan, C., "Effects of axial vibration on vertical zone-melting processing", *International journal of heat and mass transfer*, Vol. 43, pp. 1987, 2000.

108. Avetissov, I. C., A. Sadovskii, E. Sukhanova, E. Zharikov, A. Belogorokhov, and B. Levonovich, "Czochralski crystal growth assisted by axial vibrational control technique", *Journal of Crystal Growth*, Vol. 312, pp. 1104, 2010.

109. Avetissov, I. C., A. Sadovskii, E. Sukhanova, and E. Zharikov, "Single crystal growth by axial vibrational control technique in Czochralski configuration", *Journal of Crystal Growth*, Vol. 318, pp. 979, 2011.

110. Stefanescu, D. M., *Thermodynamics of solidification*, in *Science and Engineering of Casting Solidification*, Kluwer Academic, New York, 2002.

111. D. A. Porter, K. E. E., *Thermodynamics and Phase Diagrams*, in *Phase Transformations in Metals and Alloys*, Chapman & Hall, London, 1992.

112. Stefanescu, D. M., *Atomic Scale Phenomena: Nucleation and Growth*, in *Science and Engineering of Casting Solidification*, Kluwer Academic, New York, 2002.

113. Jackson, K., "Liquid metals and solidification", *ASM, Cleveland*, pp. 174, 1958.

114. Turnbull, D., "Thermodynamics in physical metallurgy", *American Society of Metals, Cleveland*, pp. 282, 1950.

115. D. A. Porter, K. E. E., *Solidification*, in *Phase Transformations in Metals and Alloys*, Chapman & Hall, London, 1992.

116. Hillig, W. and D. Turnbull, "Theory of crystal growth in undercooled pure liquids", *The Journal of Chemical Physics*, Vol. 24, pp. 914, 1956.

117. Stefanescu, D. M., *Macro-Mass Transport*, in *Science and Engineering of Casting Solidification*, Kluwer Academic, New York, 2002.

118. Burton, J., R. Prim, and W. Slichter, "The distribution of solute in crystals grown from the melt. Part I. Theoretical", *The Journal of Chemical Physics*, Vol. 21, pp. 1987, 1953.

119. Stefanescu, D. M., *Micro-Scale Phenomena and Interface Dynamics*, in *Science and Engineering of Casting Solidification*, Kluwer Academic, New York, 2002.

120. Tiller, W., K. Jackson, J. Rutter, and B. Chalmers, "The redistribution of solute atoms during the solidification of metals", *Acta metallurgica*, Vol. 1, pp. 428, 1953.

121. Davis, S. and T. Schulze, "Effects of flow on morphological stability during directional solidification", *Metallurgical and Materials Transactions A*, Vol. 27, pp. 583, 1996.

122. Coriell, S. and G. McFadden, "Buoyancy effects on morphological instability during directional solidification", *Journal of Crystal Growth*, Vol. 94, pp. 513, 1989.

123. Koichi Kakimoto, B. G., *Fluid Dynamics: Modeling and Analysis*, in *Handbook of Crystal Growth: Bulk Crystal Growth*, Elsevier, 2015.

124. Hurle, D., "*Crystal Pulling from the Melt Springer*", Berlin, 1993.

125. Jones, A., "An experimental model of the flow in Czochralski growth", *Journal of Crystal Growth*, Vol. 61, pp. 235, 1983.

126. Liang, M. and C. Lan, "Three-dimensional thermocapillary and buoyancy convections and interface shape in horizontal Bridgman crystal growth", *Journal of Crystal Growth*, Vol. 180, pp. 587, 1997.

127. Kim, K., "Suppression of thermal convection by transverse magnetic field", *Journal of the Electrochemical Society*, Vol. 129, pp. 427, 1982.

128. Cröll, A. and K. Benz, "Static magnetic fields in semiconductor floating-zone growth", *Progress in crystal growth and characterization of materials*, Vol. 38, pp. 7, 1999.

129. Dold, P. and K. Benz, "Rotating magnetic fields: fluid flow and crystal growth applications", *Progress in crystal growth and characterization of materials*, Vol. 38, pp. 39, 1999.

130. Mitric, A., T. Duffar, C. Diaz-Guerra, V. Corregidor, L. Alves, C. Garnier, and G. Vian, "Growth of Ga (1− x) InxSb alloys by Vertical Bridgman technique under alternating magnetic field", *Journal of Crystal Growth*, Vol. 287, pp. 224, 2006.

131. Watanabe, M., M. Eguchi, and T. Hibiya, "Silicon crystal growth by the electromagnetic Czochralski (EMCZ) method", *Japanese Journal of Applied Physics*, Vol. 38, pp. L10, 1999.

132. Watanabe, M., M. Eguchi, W. Wang, T. Hibiya, and S. Kuragaki, "Controlling oxygen concentration and distribution in 200mm diameter Si crystals using the electromagnetic Czochralski (EMCZ) method", *Journal of Crystal Growth*, Vol. 237, pp. 1657, 2002.

133. Capper, P., J. Brice, C. Jones, W. Coates, J. Gosney, C. Ard, and I. Kenworthy, "Interfaces and flow regimes in ACRT grown Cd x Hg 1− x Te crystals", *Journal of Crystal Growth*, Vol. 89, pp. 171, 1988.

134. Coates, W., P. Capper, C. Jones, J. Gosney, C. Ard, I. Kenworthy, and A. Clark, "Effect of ACRT rotation parameters on Bridgman grown Cd x Hg 1− x Te crystals", *Journal of Crystal Growth*, Vol. 94, pp. 959, 1989.

135. Lan, C., "Effects of centrifugal acceleration on the flows and segregation in vertical Bridgman crystal growth with steady ampoule rotation", *Journal of Crystal Growth*, Vol. 229, pp. 595, 2001.

136. Friedrich, J., J. Baumgartl, H.-J. Leister, and G. Müller, "Experimental and theoretical analysis of convection and segregation in vertical Bridgman growth under high gravity on a centrifuge", *Journal of Crystal Growth*, Vol. 167, pp. 45, 1996.

137. Wilcox, W., L. Regel, and W. Arnold, "Convection and segregation during vertical Bridgman growth with centrifugation", *Journal of Crystal Growth*, Vol. 187, pp. 543, 1998.

138. Witt, A., H. Gatos, M. Lichtensteiger, M. Lavine, and C. Herman, "Crystal Growth and Steady-State Segregation under Zero Gravity: InSb", *Journal of the Electrochemical Society*, Vol. 122, pp. 276, 1975.

139. Herrmann, F. and G. Müller, "Growth of 20 mm diameter GaAs crystals by the floating-zone technique with controlled As-vapour pressure under microgravity", *Journal of Crystal Growth*, Vol. 156, pp. 350, 1995.

140. Anilkumar, A., R. Grugel, X. Shen, C. Lee, and T. Wang, "Control of thermocapillary convection in a liquid bridge by vibration", *Journal of Applied Physics*, Vol. 73, pp. 4165, 1993.

141. Lyubimov, D., T. Lyubimova, S. Meradji, and B. Roux, "Vibrational control of crystal growth from liquid phase", *Journal of Crystal Growth*, Vol. 180, pp. 648, 1997.

142. Yuan, W., M. Banan, L. Regel, and W. Wilcox, "The effect of vertical vibration of the ampoule on the directional solidification of InSb・GaSb alloy", *Journal of Crystal Growth*, Vol. 151, pp. 235, 1995.

143. Yu, W., Z. Chen, W. Hsu, B. Roux, T. Lyubimova, and C. Lan, "Effects of angular vibration on the flow, segregation, and interface morphology in vertical Bridgman crystal growth", *International journal of heat and mass transfer*, Vol. 50, pp. 58, 2007.

144. G. Z. Gershuni and D. V. Lyubimov, *Thermal vibrational convection*, Wiley-VCH, 1998.

145. Brown, R. A., "Theory of transport processes in single crystal growth from the melt", *AIChE Journal*, Vol. 34, pp. 881, 1988.

146. Müller, G. and A. Ostrogorsky, "Convection in melt growth", *Handbook of Crystal Growth*, Vol. 2, pp. 709, 1994.

147. Yeckel, A. and J. J. Derby, "Computational simulations of the growth of crystals from liquids", *Crystal Growth Technology*, pp. 115, 2003.

148. Yeckel, A. and J. J. Derby, *Computer modelling of bulk crystal growth*, in *Bulk Crystal Growth of Electronic, Optical, and Optoelectronic Materials*, 2005.

149. Polezhaev, V., "*Modeling of technologically important hydrodynamics and heat/mass transfer processes during crystal growth*", in *Crystal Growth Technology*. pp. 155, 2003.

150. Kakimoto, K., *Heat and mass transfer under magnetic fields*, in *Crystal Growth Technology*, 2003.

151. Lan, C., "Recent progress of crystal growth modeling and growth control", *Chemical engineering science*, Vol. 59, pp. 1437, 2004.

152. Derby, J. and A. Yeckel, *Heat transfer analysis and design for bulk crystal growth: perspectives on the Bridgman method*, in *Handbook of Crystal Growth*, 2015.

153. Rhim, W.-K. and T. Ishikawa, "Thermophysical Properties of Molten Germanium Measured by a High-Temperature Electrostatic Levitator1", *International Journal of Thermophysics*, Vol. 21, pp. 429, 2000.

154. Lan, C. and J. Chian, "Three-dimensional simulation of Marangoni flow and interfaces in floating-zone silicon crystal growth", *Journal of Crystal Growth*, Vol. 230, pp. 172, 2001.

155. Yildiz, M. and S. Dost, "A continuum model for the Liquid Phase Diffusion growth of bulk SiGe single crystals", *International Journal of Engineering Science*, Vol. 43, pp. 1059, 2005.

156. Hu, H. and S. A. Argyropoulos, "Mathematical modelling of solidification and melting: a review", *Modelling and Simulation in Materials Science and Engineering*, Vol. 4, pp. 371, 1996.

157. Gartling, D., "*Finite element analysis of convective heat transfer problems with change of phase*", Sandia Labs., 1978.

158. Voller, V., M. Cross, and N. Markatos, "An enthalpy method for convection/diffusion phase change", *International journal for numerical methods in engineering*, Vol. 24, pp. 271, 1987.

159. Voller, V. R. and C. Prakash, "A fixed grid numerical modelling methodology for convection-diffusion mushy region phase-change problems", *International journal of heat and mass transfer*, Vol. 30, pp. 1709, 1987.

160. Brent, A., V. Voller, and K. t. J. Reid, "Enthalpy-porosity technique for modeling convection-diffusion phase change: application to the melting of a pure metal", *Numerical Heat Transfer, Part A Applications*, Vol. 13, pp. 297, 1988.

161. Group, S., "*CGSim Flow Module Theory Manual, v. 8.12*".

162. Friedrich, J., "CrysVun Flyer: Modeling of Crystal Growth", *Frauhofer Institute of Integrated Systems and Device Technology*, 2007.

163. Fainberg, J., D. Vizman, J. Friedrich, and G. Mueller, "A new hybrid method for the global modeling of convection in CZ crystal growth configurations", *Journal of Crystal Growth*, Vol. 303, pp. 124, 2007.

164. Fainberg, J., H.-J. Leister, and G. Müller, "Numerical simulation of the LEC-growth of GaAs crystals with account of high-pressure gas convection", *Journal of Crystal Growth*, Vol. 180, pp. 517, 1997.

165. Treibig, J., S. Berler, and U. Rüde, "ORCAN: A platform for complex parallel simulation software", *ARCS Workshops*, 2006.

166. Dupret, F., P. Nicodeme, Y. Ryckmans, P. Wouters, and M. Crochet, "Global modelling of heat transfer in crystal growth furnaces", *International journal of heat and mass transfer*, Vol. 33, pp. 1849, 1990.

167. Nowak, A. J., R. A. Białecki, A. Fic, and G. Wecel, "Analysis of fluid flow and energy transport in Czochralski's process", *Computers & fluids*, Vol. 32, pp. 85, 2003.

168. Kirpo, M., "Global simulation of the Czochralski silicon crystal growth in ANSYS FLUENT", *Journal of Crystal Growth*, Vol. 371, pp. 60, 2013.

169. Dai, B., B. Devulapalli, P. Gunjalb, and M. Kulkarni, "Calibration of the enthalpy-porosity based method for CZ silicon growth", *ECS Transactions*, Vol. 18, pp. 989, 2009.

170. Lan, C., "Three-dimensional simulation of floating-zone crystal growth of oxide crystals", *Journal of Crystal Growth*, Vol. 247, pp. 597, 2003.

171. Lyubimova, T. and Y. N. Parshakova, "Numerical investigation of heat and mass transfer during vertical Bridgman crystal growth under rotational vibrations", *Journal of Crystal Growth*, Vol. 385, pp. 82, 2014.

172. Martínez-Tomás, C. and V. Munoz, "CdTe crystal growth process by the Bridgman method: numerical simulation", *Journal of Crystal Growth*, Vol. 222, pp. 435, 2001.

173. Avetissov, I., V. Kostikov, V. Meshkov, E. Sukhanova, M. Grishechkin, S. Belov, and A. Sadovskiy, "Modeling of axial vibrational control technique for CdTe VGF crystal growth under controlled cadmium partial pressure", *Journal of Crystal Growth*, Vol. 385, pp. 88, 2014.

174. FLUENT, A., "*15-Theory Guide, ANSYS*", ANSYS Corporation, Inc., Canonsburg, PA, 2013.

175. Chorin, A. J., "Numerical solution of the Navier-Stokes equations", *Mathematics of computation*, Vol. 22, pp. 745, 1968.

176. "Properties and Characteristics of Graphite for the semi-conductor industry.", http://www.entegris.com/resources/assets/6205-7329-0513.pdf June 2016.

177. Dario, A., "*segregation and Interface Stability in Germanium-Silicon Single Crystal Alloys*", in *Mechanical Engineering*, Bogazici University, Turkey. pp. 105, 2010.

178. "*Multi Height Probe and Multi Height Microposition Probe*", Maintenance and Use of the Jandel Engineering Ltd.

179. Valdes, L. B., "Resistivity measurements on germanium for transistors", *Proceedings of the IRE*, Vol. 42, pp. 420, 1954.

180. Sze, S. and J. Irvin, "Resistivity, mobility and impurity levels in GaAs, Ge, and Si at 300 K", *Solid-State Electronics*, Vol. 11, pp. 599, 1968.

181. Sheikhi, A., P. Yousefi L, and E. Balikci, "Growing Single Crystals with a Low Melt Height and an Axial Vibration", *Crystal growth & design*, Vol. 16, pp. 2429, 2016.

182. Stelian, C. and T. Duffar, "Modeling of thermosolutal convection during Bridgman solidification of semiconductor alloys in relation with experiments", *Journal of Crystal Growth*, Vol. 266, pp. 190, 2004.

183. "*Solidification and Melting*", in *ANSYS Fluent Theory Guide*, ANSYS, Inc., Canonsburg, PA, 2013.

184. "*Basic Fluid Flow*", in *ANSYS Fluent Theory Guide*, ANSYS, Inc., Canonsburg, PA, 2013.

185. Patankar, S., *Numerical heat transfer and fluid flow*, CRC press, 1980.

186. Adornato, P. M. and R. A. Brown, "Convection and segregation in directional solidification of dilute and non-dilute binary alloys: effects of ampoule and furnace design", *Journal of crystal growth*, Vol. 80, pp. 155, 1987.

187. Mazumder, P. and R. Trivedi, "Integrated simulation of thermo-solutal convection and pattern formation in directional solidification", *Applied Mathematical Modelling*, Vol. 28, pp. 109, 2004.

188. Montakhab, M., M. Bacak, and E. Balikci, "Low Melt Height Solidification of Superalloys", *Metallurgical and Materials Transactions A*, Vol. 47, pp. 3031, 2016.

189. Scheel, H. J. and T. Fukuda, *Theoretical and Experimental Solutions of the Striation Problem*, Wiley Online Library New York, 2003.